# Applications of Galactic Microlensing

by

Daniel Kubas

A thesis submitted in partial fulfillment of the requirements for the degree of
Doctor Rerum Naturalium
in Astrophysics
at the Mathematisch-Naturwissenschaftliche Fakultät
der Universität Potsdam.

March 31, 2005

TO MY GRANDPARENTS
ILSE, GOTTFRIED, OTTILIE AND LEO
MY PARENTS, VERONIKA AND GÜNTER
MY SISTER ANTONIA
AND MR. SPOCK, GOLDENBOY AND CARLOS GARDEL

# Abstract

Subject of this work is the study of applications of the *Galactic Microlensing effect*, where the light of a distant star (source) is bend according to Einstein's theory of gravity by the gravitational field of intervening compact mass objects (*lenses*), creating multiple (however not resolvable) images of the source. Relative motion of source, observer and lens leads to a variation of deflection/magnification and thus to a time dependant observable brightness change (*lightcurve*), a so-called *microlensing event*, lasting weeks to months.

The focus lies on the modeling of binary-lens events, which provide a unique tool to fully characterize the lens-source system and to detect extra-solar planets around the lens star. Making use of the ability of genetic algorithms to efficiently explore large and intricate parameter spaces in the quest for the global best solution, a modeling software (Tango) for binary lenses is developed, presented and applied to data sets from the PLANET microlensing campaign. For the event OGLE-2002-BLG-069 the 2nd ever lens mass measurement has been achieved, leading to a scenario, where a G5III Bulge giant at $(9.4 \pm 1.4)$ kpc is lensed by an M-dwarf binary with total mass of $M_{\rm L} = (0.51 \pm 0.15) M_{\odot}$ at distance $(2.9 \pm 0.4)$ kpc Furthermore a method is presented to use the absence of planetary lightcurve signatures to constrain the abundance of extra-solar planets.



# Abstract

Thema der Arbeit ist das Studium von Anwendungen des *Galaktischen Mikrolinseneffektes* bei dem das Licht eines entfernten Sternes (Quelle) nach Einstein's Theorie der Gravitation im Schwerefeld eines sich hinreichend nahe der Sichlinie zur Quelle befindlichen massereichen kompakten Objektes (Linse) abgelenkt wird und Mehrfachbilder der Quelle erzeugt werden (welche jedoch nicht aufgelöst werden können). Die Relativbewegung von Quelle, Beobachter und Linse führt zur einer Änderung der Ablenk-und Verstärkungswirkung und somit zu einer beobachtbaren Helligkeitsänderung der Quelle (*Lichtkurve*), einem sogenannten *Mikrolinsenereignis*, welches Wochen bis Monate andauert.

Der Schwerpunkt liegt in der Modelierung von Doppellinsen-Ereignissen, welche die einzigartige Möglichkeit bieten das Linsen-Quelle System vollständig zu charakterisieren und extra-solare Planeten um den Linsenstern zu detektieren. Unter Verwendung der Eigenschaft genetischer Algorithmen hoch-dimensionale und komplizierte Parameterräume effizient nach dem besten globalen Model zu durchsuchen, wird eine Modelier-Software (Tango) entwickelt, präsentiert und auf Daten der PLANET Mikrolinsen Beobachtungskampagne angewandt. Dabei konnte für das Ereignis OGLE-2002-BLG-069 zum zweitenmal überhaupt die Linsenmasse bestimmt werden, in einem Szenario bei dem ein G5III Bulge Riese, $(9.4 \pm 1.4)$ kpc entfernt, von einem M-Zwerg Binärsystem mit einer Gesamtmasse von $M_{\rm L} = (0.51 \pm 0.15)\ M_{\odot}$ in einer Entfernung von $(2.9 \pm 0.4)$ kpc gelinst wird. Darüberhinaus wird ein Verfahren vorgestellt mit dem man die Abwesenheit planetarer Lichtkurvensignaturen nutzen kann, um Aussagen über die Häufigkeit extrasolarer Planeten zu treffen.

# Contents

# Introduction

> There are infinite many worlds, alike and unalike ours.
>
> *Epikur, 341-270 B.C.*

Subject of this work is the study of applications of the *Galactic Microlensing effect*, where the light of a distant star (source) is bend according to Einstein's theory of gravity by the gravitational field of intervening compact mass objects (*lenses*), creating multiple (however not resolvable) images of the source. Relative motion of source, observer and lens leads to a variation of deflection/magnification and thus to a time dependant observable brightness change (lightcurve), a so-called *microlensing event*, lasting weeks to months.

The analysis of these lightcurves allows us to study interesting physical aspects of the source and the lens. For example the possibility to observe distant sources with angular resolutions far beyond the reach of even our best telescopes, enabling detailed comparisons of stellar atmosphere models with observations. Microlensing also offers a new way of detecting extrasolar planets, which in principle is even sensitive to Earth-like planets. Although microlensing is still a rather young field, with the first microlensing events being reported in 1993 (Alcock et al. 1993; Aubourg et al. 1993; Udalski et al. 1993), it already has proven to be a fascinating and valuable tool for Galactic Astrophysics, with breakthrough discoveries such as the latest one for example, the detection of the most distant extrasolar planet known to this day, a Jovian planet of mass $\sim 1.5^{+0.1}_{-1.2}$ $M_J$ with a $3^{+0.1}_{-1.7}$ AU orbit around the lens of OGLE-03-235/MOA-03-53 about 17 000 lightyears away from us (Bond et al. 2004).

This thesis is structured in two parts. Part I introduces the essentials of gravitational lens theory needed for this work and also the analysis tools developed in the course of the Phd-time. Part II then is about applying these tools to selected events from the PLANET[1] microlensing campaign.
Chapters 5 to 8 are preluded by an abstract. If you do not have too much time, you should at least read the summary given in Chapter 9.

[1] planet.iap.fr

# Part I

# Theory and Simulations

In theory there is no difference between theory and practice. In practice there is.

*unknown*

# Chapter 1

# A brief review of Gravitational Lensing theory

*This and the following chapter introduce briefly the essential theory and terms needed in gravitational microlensing as applied in this work. While some technical details have been put into the appendix in order not to break the reading flow, the interested reader can find exhaustive information in the literature recommended on page 142.*

In our current understanding the propagation of light obeys Einstein's General Relativity theory. However, if one considers only weak gravitational fields (i.e. $|\phi|/c^2 \ll 1$), which is more than a fair approximation for most of the objects acting as lenses, one can simplify the problem and linearize Einstein's field equations to derive the following line element (Misner et al. 1973)

$$ds^2 = -\left(1 + \frac{2\phi}{c^2}\right) c^2 dt^2 + \left(1 - \frac{2\phi}{c^2}\right) (dx^2 + dy^2 + dz^2) \ . \tag{1.1}$$

It describes a space-time in which the speed of light is reduced in the vicinity of massive objects and the Newtonian gravitational potential $\phi$ formally acts on the light as medium with diffraction index $n = 1 - \frac{2\phi}{c^2}$. The most simple lens, a point with mass $M$ at distance $r$ has the following potential

$$\phi = -\frac{GM}{r} = -\frac{GM}{\sqrt{u^2 + z^2}} \ . \tag{1.2}$$

For small deflection angles $\vec{\hat{\alpha}}$, integration along the unperturbed light ray $z$ (passing the lens at the same minimum distance $u$ as the perturbed light ray, see Fig. 1.1) yields

$$\vec{\hat{\alpha}} = \frac{4GM}{c^2 u^2} \vec{u} = \frac{2R_s}{u} \frac{\vec{u}}{u} \ . \tag{1.3}$$

Since the part of the light path in which most of the deflection takes place is very small

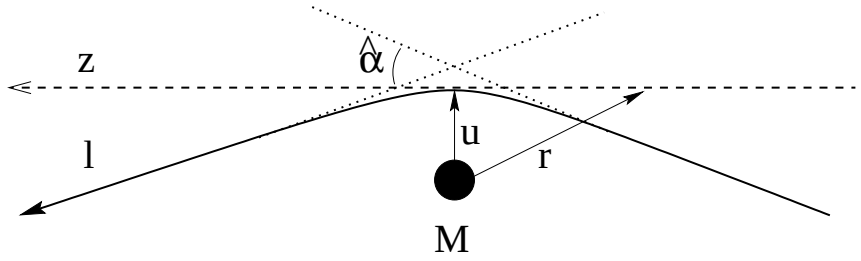


Figure 1.1: To first order the deflection of light in the vicinity of the mass M is calculated along the unperturbed ray z (dashed), passing the lens at the same distance u as the perturbed ray l (solid). Since most of the deflection takes place very close to the lens, the perturbed light path can be approximated by two unperturbed ones (dotted), which directions differ by $\hat{\alpha}$.

compared to the full path of the light ray one can define a *lens plane*, containing the projected lens mass and characterized by the surface mass density $\Sigma$

$$\Sigma(\vec{u}) = \int \rho(\vec{u}, z) dz \ . \tag{1.4}$$

The deflection at $\vec{u}$ is then the superposition of the deflections from all mass elements in the lens plane.

## 1.1 The lens equation

Fig.1.2 illustrates the geometry of the standard gravitational lens system, comprising a light source, a lens and an observer. One can directly read off the relation[1]

$$\vec{\theta} D_{\rm S} = \vec{\beta} D_{\rm S} + \vec{\hat{\alpha}} D_{\rm LS} \ , \tag{1.5}$$

which using $\vec{\alpha} = \frac{D_{\rm LS}}{D_{\rm S}} \vec{\hat{\alpha}}$ translates into

$$\vec{\beta} = \vec{\theta} - \vec{\alpha}(\vec{\theta}). \tag{1.6}$$

This equation (1.6) is known as *lens equation* and defines a two-dimensional mapping from the lens plane onto the source plane. So trivial its derivation and so harmless in its form it gives birth to a rich diversity of phenomena. In general it is nonlinear in $\vec{\theta}$ and not only changes the apparent position of the source on the sky but can also create multiple images of it.

## 1.2 The Einstein ring

For spherically symmetric lenses the lens equation with (1.3) can be rewritten as

$$\beta(\theta) = \theta - \frac{D_{\rm LS}}{D_{\rm L} D_{\rm S}} \frac{4GM(\theta)}{c^2 \theta} \ . \tag{1.7}$$

[1]Using the Euclidian relation: angular distance = angle × distance, which holds to sufficient precision on the scales of our Galaxy.

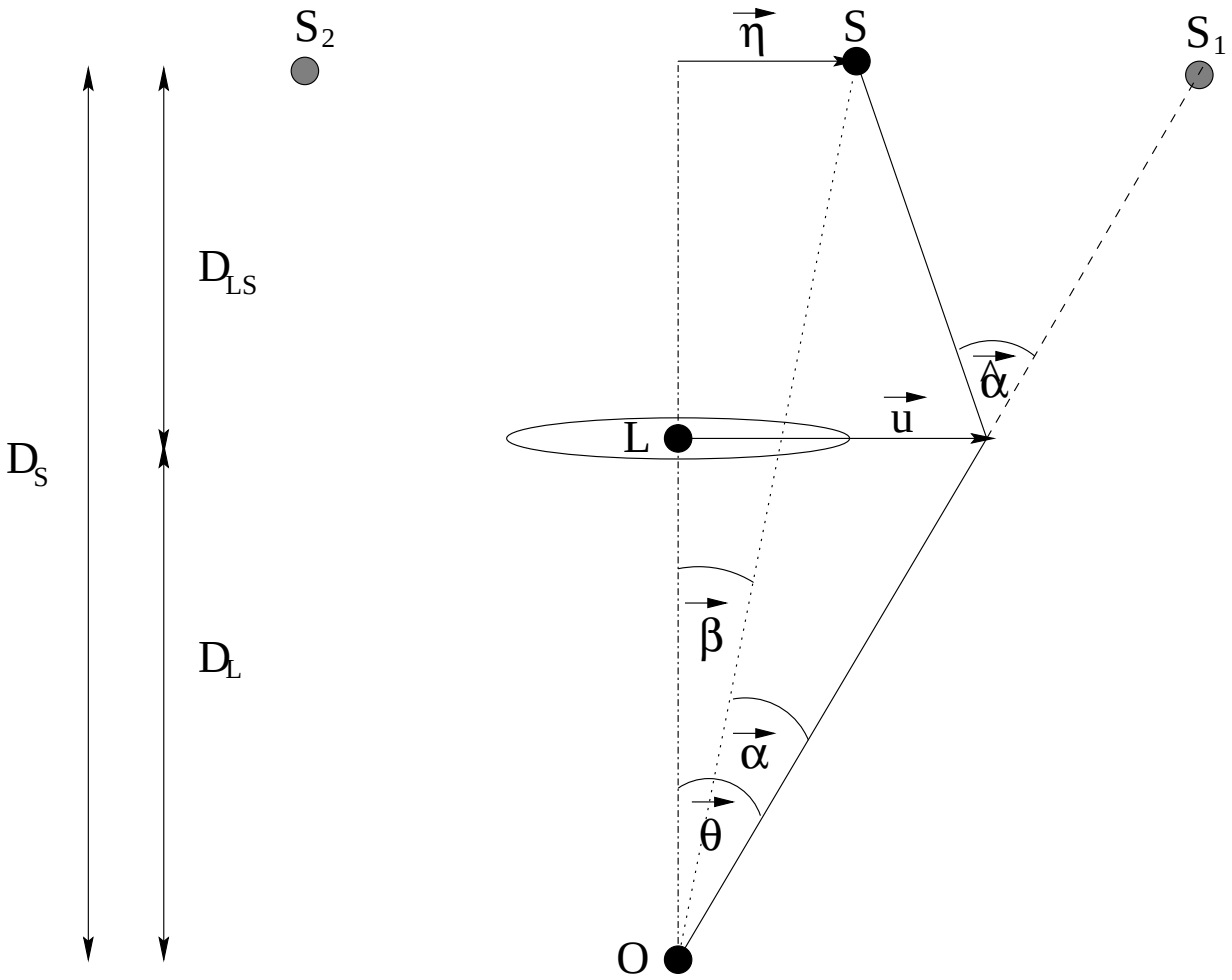


Figure 1.2: Basic geometry of a lens system. Light from the source S, located at distance $D_{\rm S}$, passing the lens with impact parameter $\vec{u}$ is bent by the angle $\vec{\hat{\alpha}}$ and reaches the observer at O. The true source position S with respect to the optical axis is marked by $\vec{\beta}$ and the position of image $S_1$ is $\vec{\theta}$. The lens is located at distance $D_{\rm L}$ and the distance between source and lens is $D_{\rm LS}$. The light path for image $S_2$ is analog to $S_1$ but not shown for reasons of clarity.

If source, lens and observer are exactly aligned on the optical axis (i.e. $\beta = 0$) the source would be imaged as ring with the angular radius (in the lens plane)

$$\theta_E = \sqrt{\frac{4GM(\theta_E)}{c^2}\frac{D_{\rm LS}}{D_{\rm L}D_{\rm S}}}\,. \tag{1.8}$$

This so called *Einstein ring* (Chwolson 1924; Einstein 1936) is the central characteristic quantity in lensing, all length and time scales are normalized to it.

## 1.3 The point mass lens (or Schwarzschild lens)

Using the Einstein radius (1.8), the lens equation for a point mass $M = M(\theta)$ has the form of a quadratic equation

$$\beta = \theta - \frac{\theta_E^2}{\theta} \,, \tag{1.9}$$

with the two solutions, i.e. image positions

$$\theta_\pm = \frac{1}{2}\left(\beta \pm \sqrt{\beta^2 + 4\theta_E^2}\right) \,. \tag{1.10}$$

The images have different parity, one residing within and the other outside the Einstein ring. Their separation is of order 2 $\theta_E$.

## 1.4 Amplification

Gravitational lensing preserves the number of photons, it only redistributes them. The observers either receives more photons (amplification) or less photons (de-amplification) compared to the case when the lens would be absent. Since also the surface brightness of the source is not changed under lensing the only remaining possibility to achieve an amplification (respectively de-amplification) is to change the solid angle under which the source is observed, so we define

$$\text{magnification} = \frac{\text{image solid angle}}{\text{source solid angle}} = \frac{\text{image area}}{\text{source area}}$$

The terms magnification and amplification therefore are equivalent. Since in this study we put an emphasis on the photometric signature of lensing we will use the term amplification in the following.
The amplification factor $A$ is given by

$$A = \frac{1}{\det J} \,, \tag{1.11}$$

where J is the Jacobian of the lens mapping (1.6). It follows that the amplification of the two images, created by a point mass lens is then

$$A_\pm = \left[1 - \left(\frac{\theta_E}{\theta_\pm}\right)^4\right]^{-1} = \frac{u^2+2}{2u\sqrt{u^2+4}} \pm \frac{1}{2} \,, \tag{1.12}$$

where the impact parameter $u = \beta\theta_E^{-1}$ measures the projected separation of lens and source as fraction of the Einstein radius. Since in galactic lensing the images in general cannot

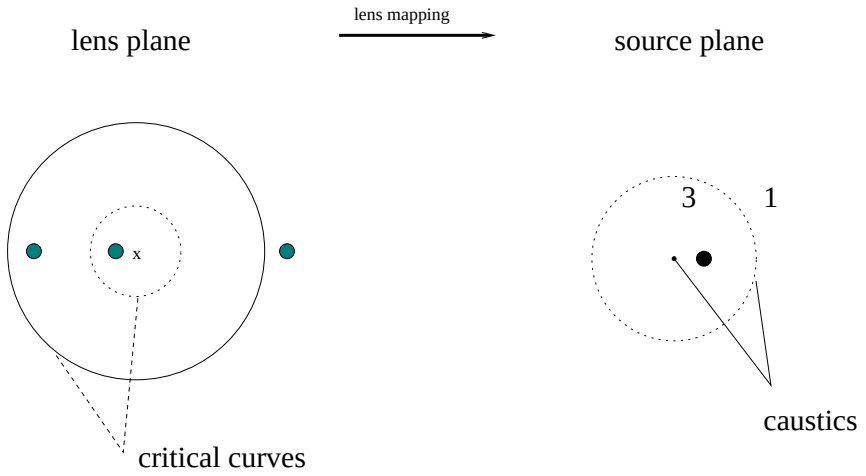


Figure 1.3: For a spherical nonsingular lens the critical curves are two circles. The inner one is mapped via the lens equation also onto a circle in the source plane. The outer one however degenerates into a point caustic. The filled small circles mark the source position (right), respectively the image positions (left). The position of the lens is marked with an x. Is the source outside the circular caustic there is only one image. Traversing the caustic to the inside creates two additional images.

be resolved (the image separations are on the order of milliarcsec), the total amplification is a more practicable quantity and reads

$$A = |A_+| + |A_-| = \frac{u^2+2}{u\sqrt{u^2+4}} \; . \tag{1.13}$$

We note that for $u \to 0$, $A \to \frac{1}{u}$, i.e. point sources would be infinitely amplified.

## 1.5 Caustics and critical curves

In reality sources are of course extended and the amplification remains finite, but apart from demonstrating the limits of our simplifying asumptions of geometric optics and point sources the points for which equation (1.11) diverges (i.e. where the Jacobian vanishes) mark regions of high amplification. In the lens plane the set of points which fulfill this criteria is called *critical curves*. The corresponding set of points (mapped via the lens equation 1.6) in the source plane are the *caustics*. Besides representing regions of high amplification caustics also separate places of different image number. The number of images is always odd and changes by 2 if a caustic is traversed. An exception from this rule is the Schwarzschild lens, where the third image is infinitely de-amplified because of the singularity of the lens. Figure 1.3 illustrates qualitatively caustics and critical curves for a circular non singular lens. In Chapter 2 we will have a closer look onto the caustics of binary lenses.

## 1.6 The microlensing effect

The mass scale of potential lenses serves as a natural hierarchy for lensing phenomena. Here we are interested in stars and planets acting as lenses in our Milky Way. A typical galactic lensing scenario comprises a source at about $D_{\rm S} = 8$ kpc and a lens at $D_{\rm L} = 6$ kpc resulting in an Einstein radius of

$$\theta_{\rm E} = 0.6 \text{ milliarcsec} \sqrt{\frac{M}{M_\odot} \frac{1}{D_{\rm L}/6 \text{ kpc}} - \frac{1}{D_{\rm S}/8 \text{ kpc}}} \tag{1.14}$$

Since we cannot resolve the multiple images in this case, the term *microlensing* was introduced in contrast to extragalactic *macrolensing* where image splittings of quasars lensed by galaxies (or galaxy clusters) are of the order of arcsecs, i.e. individual images can be observed. For a significant amplification to occur, the source and lens have to be aligned on the scale of the Einstein ring. The chances for this to happen are enhanced for sources that are distant and numerous, but even in the prime observing window for microlensing, the dense fields of the Galactic Bulge, the event rate is only about one in a million stars (see Appendix B.1 for details). Nevertheless, advances in detector and computer technology providing large field of views and fast data reduction have enabled survey teams such as OGLE (Udalski 2003) and MOA (Bond et al. 2004) to alert about $\sim 500-700$ microlensing events each year.

## 1.7 Lightcurves

The relative transversal motion $v_\perp$ of observer, lens and source leads to a change in the impact parameter $u$ and thus via equation (1.13) to a change in the observed flux $F$, i.e. a *microlensing event lightcurve* of the form

$$F(t) = F_{\rm S} A(t) + F_{\rm B} \ , \tag{1.15}$$

where $F_{\rm S}$ is the un-lensed source flux and $F_{\rm B}$ any other unresolved un-lensed flux, including the lens flux and background/crowding flux unavoidable in a typically very crowded field (see finder chart example on page 82). While ideally $F_{\rm B}$ is constant, in reality seeing and other noise can also lead to a time dependant variation. Assuming the relative motion to be a straight line in first approximation $u$ can be parameterized as

$$u(t) = \sqrt{u_o^2 + \left(\frac{t - t_{\rm o}}{t_{\rm E}}\right)^2} \ , \tag{1.16}$$

leading to (Refsdal 1964; Paczyński 1986)

$$A[u(t)] = \frac{u(t)^2 + 2}{u(t)\sqrt{u(t)^2 + 4}} \ , \tag{1.17}$$

This lightcurve model, also called Paczyński curve, is described by $t_o$ (the time when $u = u_o$), $t_E$ (the time in which the source has traversed one Einstein radius), $u_o$ (the minimum impact parameter) as well as $F_S$ and $F_B$. Figure 1.4 shows lightcurves for 4 different $u_o$ and Fig. 1.5 illustrates the influence of blending on an observed lightcurve.

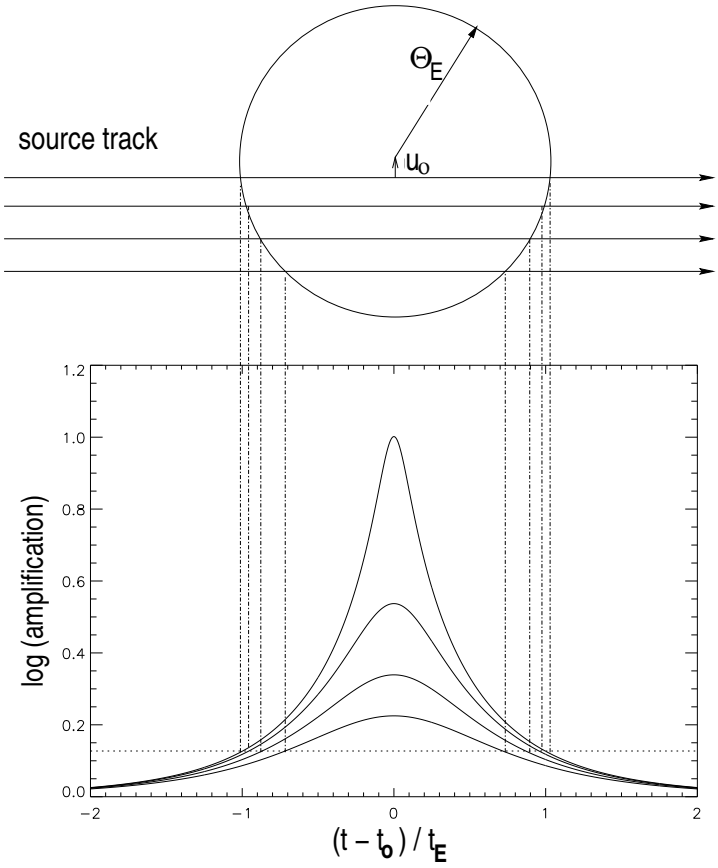


Figure 1.4: Lightcurves for a point source lensed by a point lens for different minimal impact parameter $u_o = 0.1, 0.3, 0.5, 0.7$ assuming rectilinear relative motion. On the Einstein ring $\Theta_E$ the total amplification is 1.34 (dotted line).

Out of these parameters only $t_E = \frac{R_E}{v_\perp} = \frac{\theta_E(M,D_L,D_S)D_L}{v_\perp}$ contains physical information about the lens, albeit in a degenerate combination of $v_\perp$, $M$, $D_L$ and $D_S$. While the distance to the source can be estimated from multiband/spectroscopic measurements[2], the lens usually is too faint to be detected directly. Interpretation of a microlens event in general therefore requires assumptions on the lens distance and motion. For a typical scenario with $D_S = 8$ kpc, $D_L = 6$ kpc and $v_\perp = 200$km/s the time scale of an event is on the order of

$$t_E \sim 30 \text{ Tage } \sqrt{\frac{M}{M_\odot}} \,. \tag{1.18}$$

[2]Knowing the spectral type from stellar models (van Belle 1999) one can derive the linear radius of the source and its absolute luminosity to infer its distance.

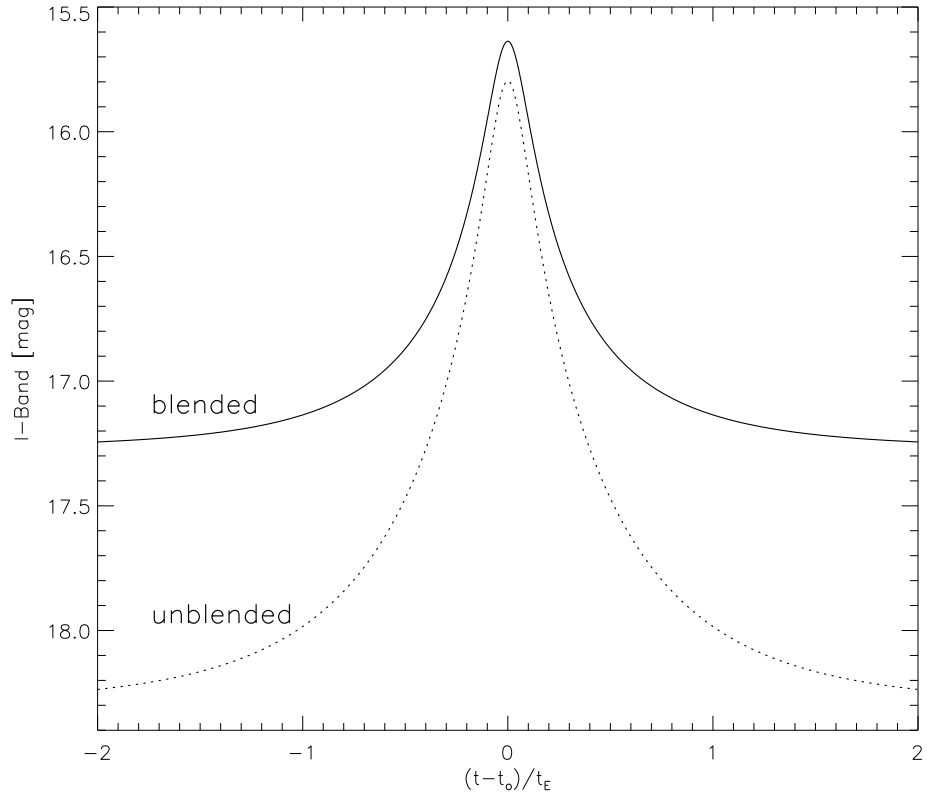


Figure 1.5: The effect of (constant) blending onto the observed lightcurve. The solid line curve shows the flux (in magnitudes) for a source with intrinsic brightness of $F_{\rm S} = 18.30$ mag undergoing a single lens event with $u_o = 0.1$ but with an additional blend fraction of $h = F_{\rm B}/(F_{\rm S} + F_{\rm B}) = 0.61$. The dotted line marks the lighcurve with the same $u_o$ and $F_{\rm S}$ as it would be observed in the absence of blending. When the data covers only a small fraction of the amplification gradient, for instance only the peak region, the blending will be only poorly constrained, which can lead to severe misestimates of the true lens event parameters. A high amplification event could then be easily masked as a low amplification event in crowded fields typical for galactic microlensing (see Fig. 6.1 for instance).

# Chapter 2

# The binary lens

> A double lens is vastly more complicated than a single one.
>
> *Paczynski, 1996*

The most simple planetary system consists of two bodies, a planet and a star. Since also stars very often come in pairs, it seems more than worthwhile to study the effects of binary lenses. Following equation (1.4) the deflection angle of a distribution of point masses in the lens plane is equal to the sum of the deflection angles of each point lens of mass $m_i$ at $\vec{x_i}$. With normalized coordinates $\vec{x} = \frac{\vec{\theta}}{\theta_{\rm E}}$, $\vec{y} = \frac{\vec{\beta}}{\theta_{\rm E}}$ this can be written as

$$\vec{\alpha}(\vec{x}) = \frac{4G}{c^2} \sum_i^n m_i \, \frac{\vec{x} - \vec{x_i}}{|\vec{x} - \vec{x_i}|^2} \; . \tag{2.1}$$

so the lens equation for n point masses takes on the form

$$\vec{y} = \vec{x} - \sum_i^n m_i \, \frac{\vec{x} - \vec{x_i}}{|\vec{x} - \vec{x_i}|^2} \; , \tag{2.2}$$

with the convention $\sum_i^n m_i = 1$. In the case of a binary lens ($n = 2$) it is useful to introduce the mass ratio $q = \frac{m_2}{m_1}$ and the separation of the lens components $d$ (measured in fractions of the Einstein radius). For unequal masses $m_1$ is defined to be the primary mass, i.e. $0 < q \leq 1$. For $q \ll 1$ let $m_1 = M_*$ be the star mass and $m_2 = m_{\rm pl}$ the planet mass. Putting $m_1$ into the origin $(0, 0)$ and $m_2$ to $(0, d)$ the binary lens equation reads

$$\vec{y} = \vec{x} - m_1 \frac{\vec{x}}{|\vec{x}|^2} - q m_1 \frac{\vec{x} - \vec{d}}{|\vec{x} - \vec{d}|^2} \quad . \tag{2.3}$$

It is an algebraic equation of 5th order in $|\vec{x}|$, and which in dependence of $q$ and $d$ either has 3 or 5 solutions. Contrary to the single point lens it has a rich caustic structure giving rise to an enormous lightcurve diversity. Although there is no closed analytic form for

its solution one can at least explicitely calculate the caustics and get a first feeling for the expected lens properties. Schneider & Weiss (1986) could show that there are exactly 3 different topologies for arbitrary mass ratios $q$. Figures 2.1 and 2.2 show caustics and critical curves for $q = 1$ (i.e., $m_1 = m_2$) and $q = 0.1$ for different separations $d$. The caustics are no longer degenerated into a point as in the single lens case but show the following geometries. For small separations 3 caustics are formed, 2 three-cusped[1] secondary caustics as well as a central four-cusped caustic. The transition to wide separations is marked by a single six-cusped caustic, which for sufficient large $d$ breaks up into two four-cusped caustics. Details on how to derive these binary lens caustics/critical lines are given in Appendix B.2.
The amplification of the binary lens (assuming a point source) can then be computed by solving the binary lens equation (2.3) at each source position and calculated according to Eq. (1.11) via $A = 1/\det J$, with $J = \frac{\partial \vec{y}}{\partial \vec{x}}$ being the Jacobian of the lens mapping[2].

## 2.1 Planets as lenses

While as seen in Fig. 2.2 for mass ratios $q < 1$ the caustics shrink, change their relative positions, get compressed or stretched and only the $x_2 = 0$ axis remains as symmetry axis, their topology is still equivalent to the case $q = 1$. When the mass ratio is in the planetary regime ($q \leq 10^{-2}$) the triangular-shaped secondary caustics are also called *planetary caustics* and the caustic close to the main lens is referred to as *central caustic*. The idea how to use microlensing to detect planets around the lens star is then rather simple. If the source hits the influence region of the planetary (or central) caustic this should lead to deviations from the normal Paczyński-form of a single lens, which can be revealed by photometric observations (Mao & Paczyński 1991). An example of a planetary lightcurve perturbation is shown in Fig. 2.3. The following sections serve to quantify this planetary signal and discuss its observability.

[1]The ends of closed caustic curves are not named corners but cusps. This stems from catastrophe theory, a mathematical discipline dealing with singularities of differentiable mappings, to which also the lens mapping belongs (Arnold 1984).

[2]It turns out that this calculus best is done using the complex notation of Witt (1990) in which the binary lens equation (2.3) reads: $c = z + \frac{m_1}{z_1 - \overline{z}} - q\frac{m_2}{z_2 - \overline{z}}$, with $c = y_1 + iy_2, z = x_1 + ix_2$ .

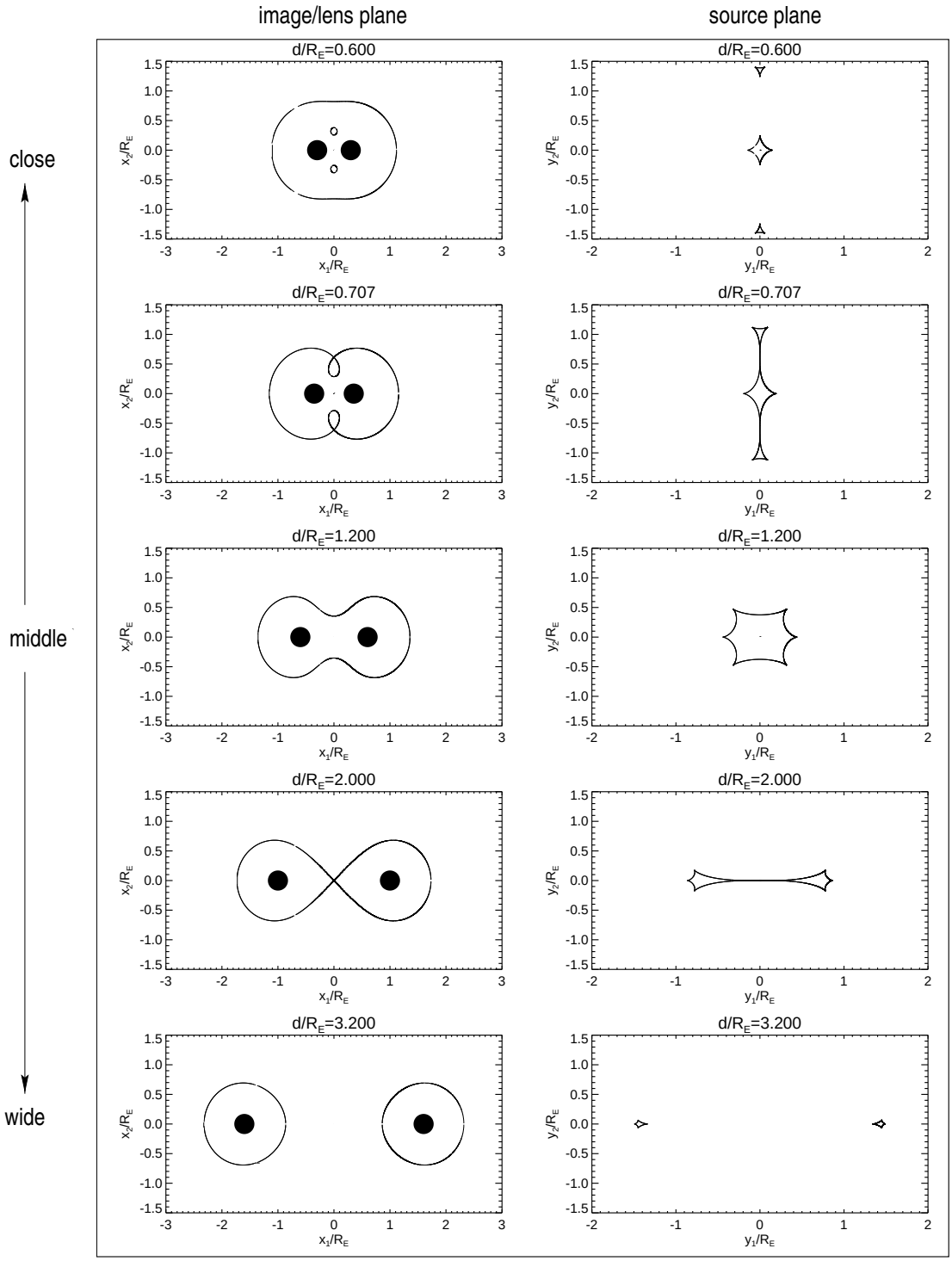


Figure 2.1: Critical curves (left column, lens/image plane) and caustics (right column, source plane) of a binary lens with mass ratio $q = 1$ for different separations $d$ (increasing from top to bottom). The black filled circles mark the lens positions with the center of mass serving as origin.

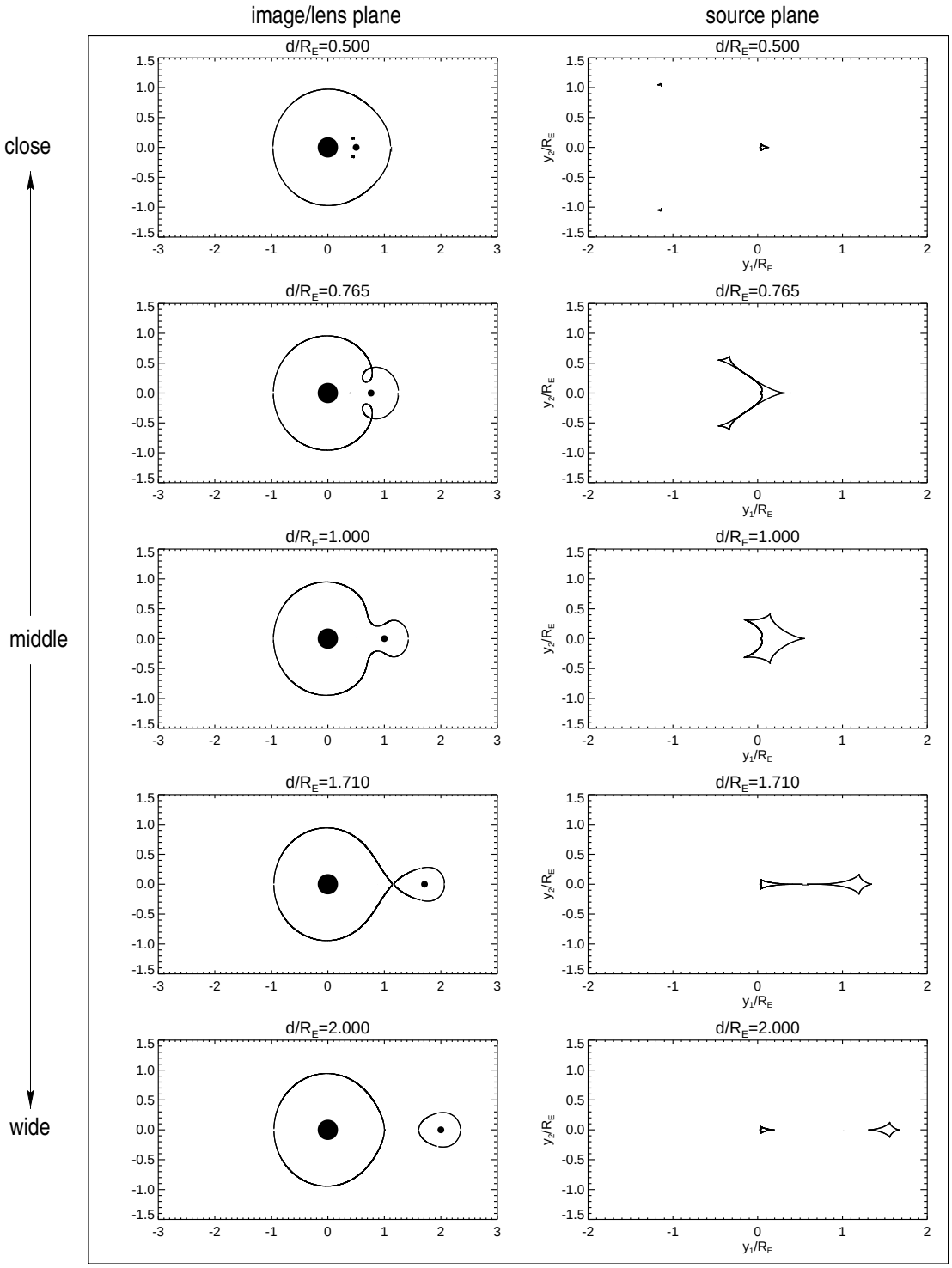


Figure 2.2: Critical curves (left column) and caustics (right column) of a binary lens with q=0.1. The primary mass (big filled circle) lies in the origin.

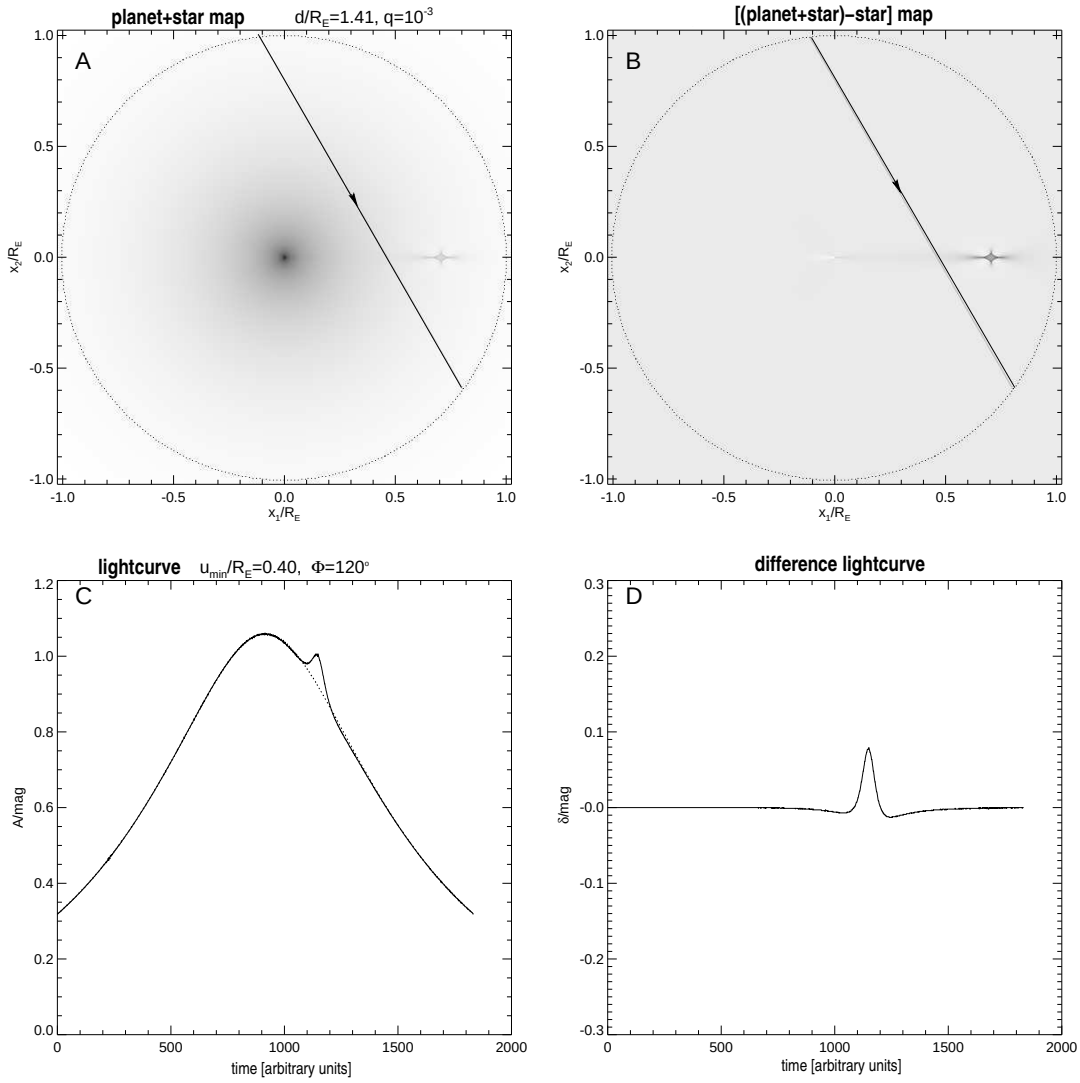


Figure 2.3: **A**: Amplification map (generated with the ray-shooting technique introduced in Sec. 2.2.1) of a star+planet configuration with mass ratio $q = 10^{-3}$ and separation $d = 1.41$. The circle marks the Einstein ring and the line the source motion. **B**: Here the amplification effect of the lens star has been subtracted for better contrast of the planetary lens effect. **C**: Resulting lightcurve of the track marked in map A. The dotted line marks the single lens lightcurve as it would be observed in the absence of the planet. **D**: Lightcurve of the difference map B showing only the photometric signal of the planet.

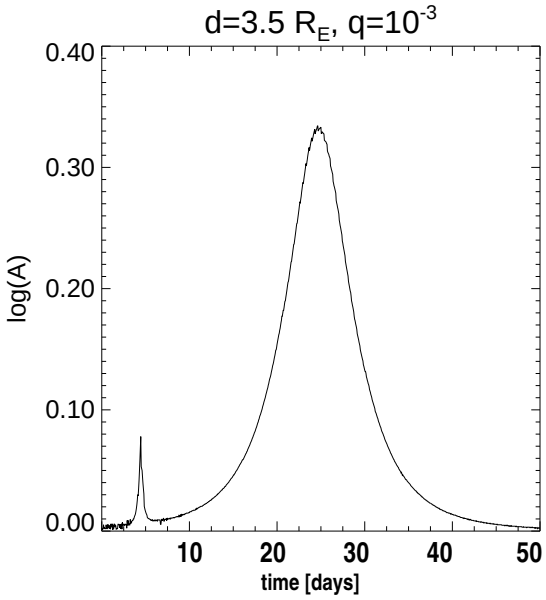


Figure 2.4: A planet with $q = 0.001$ and 3.5 Einstein radii away from its parent star could leave a single lens like signature (first peak) which is too short (ranging from days down to hours for Jupiters, repectively Earths) to be picked up by current survey teams in contrast to the main lens event due to the lens star, lasting weeks to months.

### 2.1.1 The lensing zone

If the secondary caustics are outside the Einstein ring of the primary lens the chances of detecting planets with current observational campaigns (see Sec. 4) are significantly reduced. Firstly the amplification of the primary is $A < 1.34$, i.e. the signal-to-noise gets poorer. Secondly for increasing lens separation the event behaves essentially as being two independent lenses (see Fig. 2.4) and so the 'single' lens event of the planet can get too short (days to hours for Jupiters, respectively Earths) to achieve a convincing data coverage. If lens separations are too small the lens acts more and more as a single one. For planet-star separations where the planetary caustics are inside the Einstein ring of the main lens, the planet can affect the microlens event therefore most effectively. This condition is fulfilled for planet-star distances d in the so called *lensing zone* (see also Fig. 2.5)

$$0.6R_{\mathrm{E}} \lesssim d \lesssim 1.6R_{\mathrm{E}} \; . \tag{2.4}$$

A derivation of this relation is given in Appendix B.3. By scaling the (linear) Einstein radius properly

$$R_{\mathrm{E}} = 8.0 \text{ AU} \sqrt{\frac{M}{M_{\odot}} \, \frac{D_{\mathrm{S}}}{8 \text{ kpc}} \, x(1-x)} \quad , x \equiv \frac{D_{\mathrm{L}}}{D_{\mathrm{S}}} \; . \tag{2.5}$$

using a typical lens scenario (with $D_{\mathrm{L}} = 4$ kpc, respectively 6 kpc and $D_{\mathrm{S}} = 8$ kpc) this translates to roughly to 1 AU - 4 AU, which by chance happens to overlap with the habitable

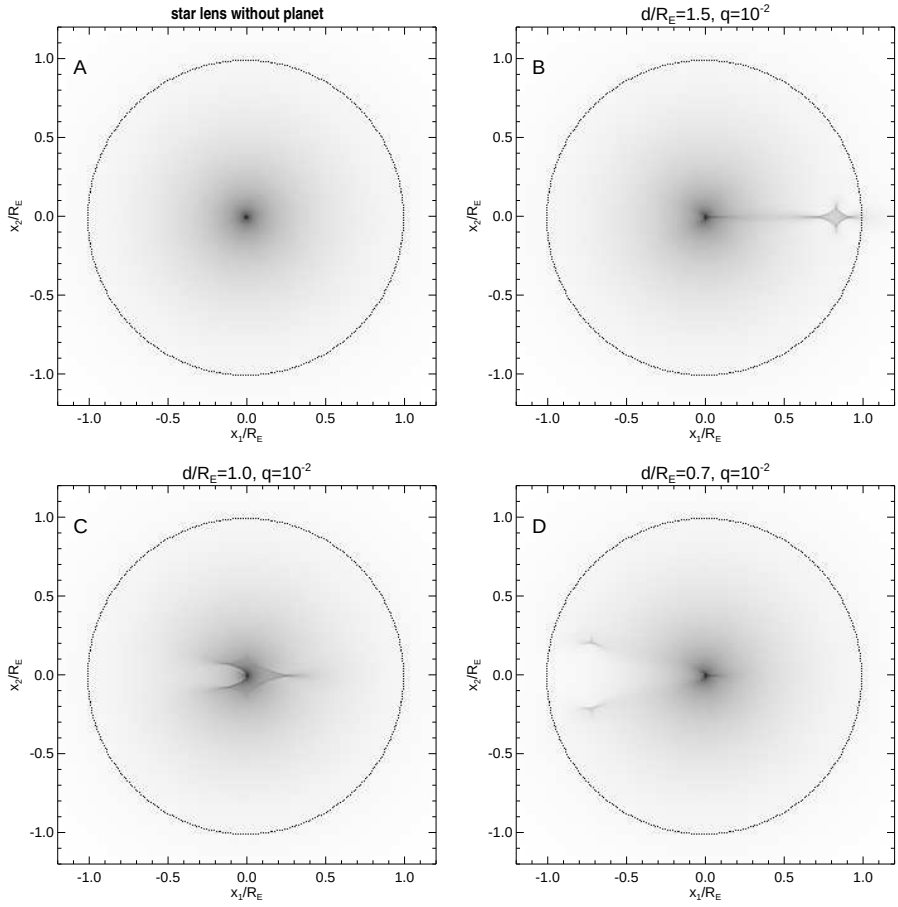


Figure 2.5: Amplification map **A** shows the spherically symmetric pattern of a single point mass lens. Maps **B-D** display a lens with a planetary companion of mass ratio $q = 10^{-2}$ at three different positions in the lensing zone, namely at $d/R_{\rm E} = 1.5, 1.0, 0.7$. In all cases the secondary/planetary caustics are within the Einstein ring (dotted circle) of the lens star. Again dark regions mark high amplification areas and bright regions low amplifications.

zones of sun-like stars [3]. There exists however a way to probe planet-star distances beyond this zone. The central caustic, keeping its position close to the lens star, is sensitive to companions outside the lensing zone. The caveat herein however is the fact that any companion affects the central caustic and even for rather dense data coverage ambiguous solutions between planetary and a star companion can occur. Such a case is presented in Sec. 6. However, the absence of lightcurve anomalies in those high amplification events probing the central caustic, can be more safely used to exclude/constrain the presence of planetary companions as demonstrated in Chapter 8.

[3]The habitable zone is defined as orbital region, in which liquid water can exist on a planet's surface (Hart 1979).

### 2.1.2 Planetary detection probabilities

While as seen above, planets can in principle be detected via microlensing, the more practical question is how likely this planetary signature is to occur in order to motivate/justify observing campaigns. Intense numerical simulations performed by Kubas & Wambsganß (2001) assuming that each lens has a planet in the lensing zone and that the lightcurve is completely sampled yielded the following upper limits. Defining a detection criteria by demanding that the deviation from the single-lens behavior $\delta(t) \equiv \frac{A(t)-A_{\rm single}(t)}{A_{\rm single}(t)}$ exceeds a given threshold for at least 3 consecutive measurements, a Jupiter in the lensing zone would for example in $\sim 12$ % of the cases leave a signature of amplitude $\gtrsim 0.05$ mag and lasting $\gtrsim 5$ % of the Einstein time scale $t_{\rm E}$ of the event (translating to $\gtrsim 3$ days for a typical $t_{\rm E}$ of $\sim 20$ days). Microlensing teams such as PLANET (see Sec. 4) achieving $1-2$ % photometry and hourly sampling should therefore be easily capable to pick up these signals.

Table 2.1: For source sizes $R_{\rm S}/R_{\odot}$=0.8, 7.5, 23.3 and mass ratios $q = 10^{-3}, 10^{-4}, 10^{-5}$ the (over the lensing zone) integrated detection probability $\hat{P}$ for the planetary signature is given for each combination of the criteria $|\delta| \geq 5\%, 3\%, 1\%$ and $t_{\rm p}/t_{\rm E} \geq 5\%, 3\%, 1\%$. For instance the probability $\hat{P}_5^3$, i.e. $|\delta| \geq 5\%$ and $t_{\rm p}/t_{\rm E} \geq 3\%$ is 0.18 for $R_{\rm S} = 0.8 R_{\odot}$ and $q = 10^{-3}$.

| | | | $\hat{P}_5^{t_{\rm p}}, \|\delta\| \geq 5\%$ | | | $\hat{P}_3^{t_{\rm p}}, \|\delta\| \geq 3\%$ | | | $\hat{P}_1^{t_{\rm p}}, \|\delta\| \geq 1\%$ | | |
|---|---|---|---|---|---|---|---|---|---|---|---|
| | q | $t_{\rm p}/t_{\rm E} \geq$ | 5% | 3% | 1% | 5 % | 3 % | 1% | 5% | 3% | 1% |
| | $10^{-3}$ | | 0.13 | 0.18 | 0.23 | 0.22 | 0.27 | 0.32 | 0.46 | 0.50 | 0.53 |
| $R_{\rm S} = 0.8 R_{\odot}$ | $10^{-4}$ | | 0.01 | 0.02 | 0.06 | 0.02 | 0.03 | 0.08 | 0.06 | 0.11 | 0.16 |
| | $10^{-5}$ | | 0.00 | 0.00 | 0.01 | 0.00 | 0.00 | 0.01 | 0.00 | 0.01 | 0.03 |
| | $10^{-3}$ | | 0.12 | 0.18 | 0.23 | 0.21 | 0.28 | 0.32 | 0.46 | 0.50 | 0.52 |
| $R_{\rm S} = 7.5 R_{\odot}$ | $10^{-4}$ | | 0.01 | 0.02 | 0.05 | 0.02 | 0.03 | 0.08 | 0.06 | 0.11 | 0.15 |
| | $10^{-5}$ | | 0.00 | 0.00 | 0.00 | 0.00 | 0.00 | 0.01 | 0.00 | 0.01 | 0.03 |
| | $10^{-3}$ | | 0.12 | 0.15 | 0.16 | 0.20 | 0.24 | 0.27 | 0.46 | 0.48 | 0.50 |
| $R_{\rm S} = 23.3 R_{\odot}$ | $10^{-4}$ | | 0.00 | 0.00 | 0.01 | 0.01 | 0.02 | 0.02 | 0.06 | 0.08 | 0.10 |
| | $10^{-5}$ | | 0.00 | 0.00 | 0.00 | 0.00 | 0.00 | 0.00 | 0.00 | 0.00 | 0.00 |

In Table 2.1 detection probabilities for a variety of different thresholds in $|\delta|$ and anomaly durations $t_{\rm p}$ for three different mass ratios $(\log\ q) = -3, -4, -5$ (corresponding roughly to Jupiter, Neptune and Earth masses) and three different source sizes $R_{\rm S}/R_{\odot} = 0.8,\ 7.5,\ 23.3$ are given. Using a grid of amplification maps spanning the separations $d$= 0.10, 0.18, 0.32, 0.56, 0.71, 0.89, 1.00, 1.12, 1.41, 1.78, 3.16, 5.62, 10.00 for each mass ratio and source size these probabilities were then derived by scanning each map uniformly in impact angle and impact parameter and counting succesfull detections for a given criterion.

## 2.2 Extended Sources

In the majority of cases, lenses and sources in Galactic microlensing are treated as point like, based on the fact that the physical sizes of lenses $R_{\rm L}$ and sources $R_{\rm S}$ are negligible compared to the characteristic Einstein radius. While for compact lenses such as stars and planets one finds that $R_{\rm L}/R_{\rm E} \ll 1$ holds in virtually all cases (with $D_{\rm S} = 8$ kpc, $D_{\rm L} = 6$ kpc a Sun-like lens would imply $R_{\rm L}/R_{\rm E} = 0.001$ and a Jovian lens $R_{\rm L}/R_{\rm E} = 0.005$), things can be very different for the source size. Table 2.2 lists angular radii for different star types serving as a reference length scale and also the Einstein radii for various masses (assuming again $D_{\rm S} = 8$ kpc, $D_{\rm L} = 6$ kpc).

| Source sizes | | | Einstein radii of Lenses | |
|---|---|---|---|---|
| $R_{\rm S}/R_\odot$ | $R_{\rm S}/\mu$as | spectral type | Lens mass/$M_\odot$ | $R_{\rm E}/\mu$as |
| 0.8 | 0.6 | G2 V (ZAMS) | 1 | 583.1 |
| 2.3 | 1.8 | A1 V (") | $10^{-3}$ | 18.4 |
| 7.5 | 5.8 | B1 V (") | $10^{-4}$ | 5.8 |
| 23.3 | 18.1 | K2 III (Giant) | $10^{-5}$ | 1.8 |

Table 2.2: **Left**: Radii of different source stars in solar radii and angular units. **Right**: Einstein radii for different lens masses. (All values for $D_{\rm S} = 8$ kpc, $D_{\rm L} = 6$ kpc.)

One clearly sees that mostly giants with radii of $\sim 10\ R_\odot$ and larger have dimensions that correspond to the sizes of planetary caustics and Einstein radii. Therefore in the planetary microlensing regime, especially in the case of a star with a Sub-Jovian companion, finite source effects cannot be neglected (see Figure 2.6) and the source actually can get resolved by the caustic.

Considering binary lenses with mass ratios of $q \sim 1$ the caustic structures can get so large with respect to the source size that one can use caustic passages to study in detail the stellar atmosphere of the source (Cassan et al. 2004; Kubas et al. 2005b). Even in single lens events finite source can occur when the impact parameter is of the order of the source size and the point caustic transits the source, i.e. in high amplification events such as OGLE-2003-BLG-262 (Yoo et al. 2004a) or OGLE-2004-BLG-254 (Chapter 7).

The increase in power of observing campaigns such as OGLE (Udalski 2003), MOA (Bond et al. 2004) and PLANET (Albrow et al. 1998) has lead to an increase in detection and sampling rates of microlensing events and thus to more and more measurements of extended source effects. While finite sources pose a major challenge in the analysis of the data, they open the possibility to break some degeneracies of the lens-source system and so their study is more than worthwhile.

Although a variety of techniques for calculating the amplification of extended sources exist, there is, apart from the point lens case (Witt & Mao 1994a), no all-in-one solution neither analytically nor numerically. To avoid the numerical instabilities in integration schemes arising from the singularities of the caustics in the source plane one has tackled

the problem in the lens plane, where no singularities occur. By contour integration the area of the images is determined to compute the amplification (Kayser & Schramm 1988; Dominik 1995), but even its most efficient implementations (Gould & Gaucherel 1997; Dominik 1998a) using the Stokes theorem (i.e. only integrating along image boundaries) are too slow for modeling tasks, which require to compute at least $\gtrsim 10^5$ different models (Mao & Di Stefano 1995)[4]. The only robust method that works in the source plane is the ray-shooting (Kayser et al. 1986; Wambsganss 1997) technique, explained in the following Section 2.2.1. While this method only allows to compute discrete parameter sets for mass ratio $q$, lens separation $d$ and source profiles, its strengths are that it can deal with arbitrary source profiles and once an *amplification map* (see below) is computed different source trajectories, i.e. lightcurves, can be generated very fast ($\ll 1$ s).

In special cases another speed up of calculation time can be achieved, namely when during a fold-caustic passage the caustic can be approximated as a straight line and its strength does not vary significantly over the scale of the source size. This *straight-fold-caustic* passage case (see Sec. 2.2.2) is most common to occur for $q \sim 1$ binary lenses, which possess sufficiently large caustic structures and which provide the unique opportunity to study the normally un-resolvable source profiles[5].

### 2.2.1 Ray shooting

In ray-shooting the light-path depicted in Fig. 1.2 is reversed. Starting from the observer rays are 'shoot' under different angles onto the lens plane, where they are deflected according to Eq. (1.4) and then collected in the source plane. The density of light rays in the source plane is then directly proportional to the amplification of the source at that position. This way a map of the source plane is created, which contains the value of amplification for each point in the map. Lens and source plane are both modeled as a uniform pixel grid. The pixel size sets the lower limit for the source size for a particular map. Arbitrary source profiles can be easily modeled by convolving the profile with the map, which is best done via an FFT (Fast Fourier Transformation).

When shooting maps one has to take care not to loose too many rays. For instance if the lens plane grid is too small, rays outside this grid which would hit the source plane are lost. To obtain a good signal-to-noise ratio it is necessary to shoot a sufficient number of rays, to be more exact the relative error is $\sim {N_S}^{-1/4}$ (Kayser et al. 1986), where $N_S$ is the number of rays per source area. In the maps used here, we achieve ray densities $\geq 10^4$ per pixel so that the numerical noise is acceptable low. The for our purposes essential lightcurves are then just one-dimensional cuts thru these maps. Fig. 2.6 shows two gray-scale-coded ray shooting maps for a star+planet lens scenario, one unsmoothed map, where the pixel size

[4]Computing one model on a XP9000 workstation with an image integration routine using Stoke's theorem takes about $\sim 1$ min. An optimization process could therefore take several months, unless one has access to more powerful computational resources.

[5]While it was shown that semi-analytical approximations, albeit much more cumbersome in their form, exist for cusp-caustic passages (Gaudi & Petters 2002) up to now no working modeling algorithm implementation is known.

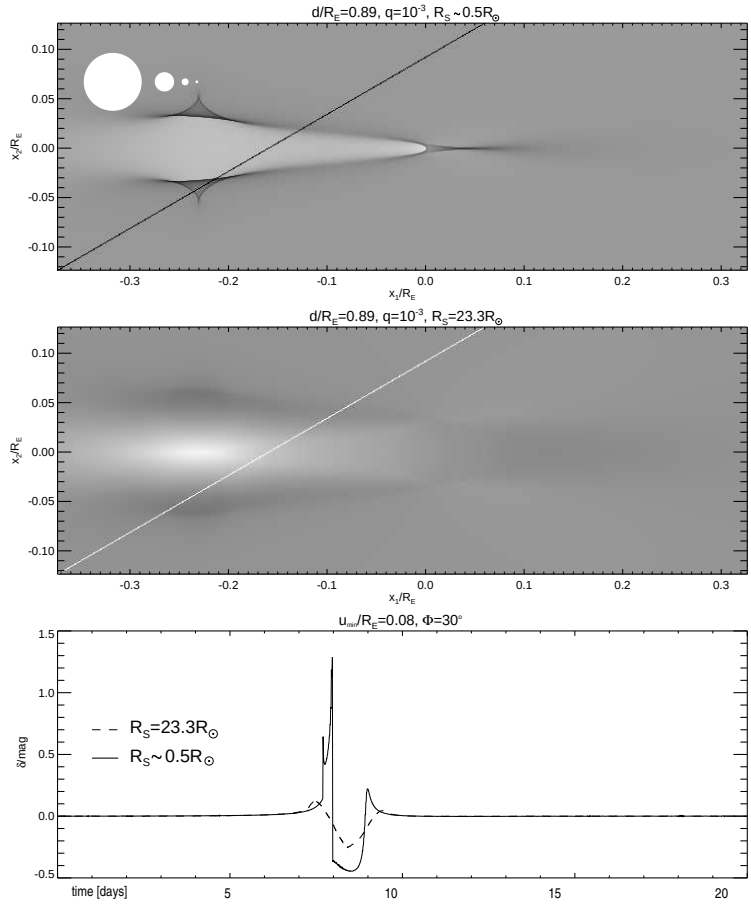


Figure 2.6: **Top**: (Un-smoothed) magnification map for separation $d = 0.89$ and mass ratio $q = 10^{-3}$.The lens star is located at the origin, while the lens planet sits on the positive x-axis at (0.89,0.), i.e. outside the displayed map part. The filled white circles mark to scale 4 different sized (uniform bright) sources with $R_{\rm S}/R_{\odot}$=0.8, 2.3, 7.5, 23.3. **Middle**: Magnification map convolved with the $R_{\rm S} = 23.3R_{\odot}$ source. The originally sharp caustic structures are strongly blurred. **Bottom**: The resulting lightcurve for the drawn source trajectory in the map(s). The amplitude of the caustic passage signal for the large source (dashed line) is significantly damped compared to the unresolved pixel sized source (solid line). Note that in this planetary lens scenario we subtracted the single-lens lightcurve signal of the lens star to show the extended source effects on planetary lightcurve anomalies more clearly.

corresponds to a source $R_{\rm S} \sim 0.5\ R_{\odot}$ and the same map convolved with a giant source of radius $R_{\rm S} = 23.3\ R_{\odot}$. The large source blurs the sharp caustic structure and clearly damps the lightcurve signal of the shown source trajectory. This effect poses a serious problem especially for the detection and characterization of Sub-Jovian planets in current ground based microlensing campaigns, since in general only large sources (mainly Bulge Giants) are bright enough for the $\sim$ 1m class telescopes used[6].

[6]Besides the lack of light gathering power another limiting factor is the needed spatial resolution to

Finally we note that a modified version of the Fortran coded *Microlens* ray shooting program developed by Wambsganss (1999) is used in this work.

### 2.2.2 The Straight Fold Caustic approximation

According to Eq. 2.3 a point source inside a binary lens caustic has five images. As the source exits the caustic, the amplifications of two of these images diverge towards a square-root singularity until the images suddenly disappear. Neglecting any changes of the lens properties in the neighborhood of the caustic crossing, the amplification $A_{\rm crit}$ of these two critical images can be written (Schneider & Weiss 1986) as function of the vectorial impact position $\mathbf{u}$ ,

$$A_{\rm crit}(\mathbf{u}) = \left(\frac{\Delta u_\perp}{u_r}\right)^{-1/2} \Theta(\Delta u_\perp), \tag{2.6}$$

where

$$\Delta u_\perp \equiv \Delta\mathbf{u}\cdot\mathbf{n}_{\rm cc}, \qquad \Delta\mathbf{u} \equiv \mathbf{u}-\mathbf{u}_{\rm cc}, \tag{2.7}$$

$\mathbf{u}_{\rm cc}$ is the position of the caustic crossing, $\mathbf{n}_{\rm cc}$ is the unit vector at $\mathbf{u}_{\rm cc}$ pointing inward normal to the caustic, $\Theta$ is a step function, and $u_r$ is the characteristic rise length of the caustic. The amplification of the three other images varies only little during the caustic crossing, so their total amplification $A_{\rm other}$ can be Taylor expanded,

$$A_{\rm other}(\mathbf{u}) = a_{\rm other} + \mathbf{Z}\cdot\Delta\mathbf{u}, \tag{2.8}$$

where $a_{\rm other}$ is the amplification of the three images at the caustic crossing, and $\mathbf{Z}$ is the gradient of the amplification with respect to $\mathbf{u}$. Hence the total amplification in the neighborhood of the caustic crossing can be approximated as,

$$A(\mathbf{u}) = \left(\frac{\Delta u_\perp}{u_r}\right)^{-1/2} \Theta(\Delta u_\perp) + a_{\rm other} + \mathbf{Z}\cdot\Delta\mathbf{u}. \tag{2.9}$$

For an extended source of radius $\rho_* \equiv \theta_*/\theta_{\rm E}$, the amplification is given by the convolution of $A$ with the source surface brightness profile, which yields (e.g. Schneider et al. 1992, p. 215f),

$$A^s(\mathbf{u}) = \left(\frac{u_r}{\rho_*}\right)^{1/2} G\left(-\frac{\Delta u_\perp}{\rho_*}\right) + a_{\rm other} + \mathbf{Z}\cdot\Delta\mathbf{u}. \tag{2.10}$$

where $G$ is a characteristic profile function depending only on the shape of the stellar profile. For uniform surface brightness, the profile function $G$ in dependence from the distance source center to caustic $\eta$ reads (Schneider & Weiss 1987),

$$G_0(\eta) \equiv \frac{2}{\pi}\int_{\max(\eta,-1)}^{1} \left(\frac{1-x^2}{x-\eta}\right)^{1/2} dx\Theta(1-\eta), \tag{2.11}$$

resolve smaller source stars, a capability which is seriously affected by seeing conditions. Next generation microlensing campaigns therefore aim to use space-bases telescopes or sites at Antarctica's Dome C (Beaulieu et al. 2004), where almost space like seeing conditions prevail.

which can be expressed in terms of elliptical integrals and where $\Theta$ is a step function.

Considering the extended source to move over the caustic with proper motion $\mu = \theta_E/t_E$, at an angle $\phi$ relative to the caustic, the time required for the radius to cross the caustic is

$$\Delta t = \frac{\theta_*}{\mu \sin\phi} = \frac{\rho_* t_{\rm E}}{\sin\phi}\,. \tag{2.12}$$

Note that while the width of the caustic crossing $\Delta t$ can be measured from the caustic-crossing data alone, the three quantities whose product forms $\Delta t$ ($\rho_*$, $t_{\rm E}$, and $\csc\phi$) can only be determined from an analysis of the complete light curve. With the (angular) separation of the source from the caustic as a function of time being $\Delta\mathbf{u} = \boldsymbol{\mu}(t - t_{\rm cc})/\theta_{\rm E}$, where $t_{\rm cc}$ is the time of the caustic crossing[7], the total amplification parameterized with time is given by

$$A(t) = a_{\rm crit} G_0\left(\frac{t - t_{\rm cc}}{\Delta t}\right) + a_{\rm other} + \omega(t - t_{\rm cc})\,, \tag{2.13}$$

with

$$a_{\rm crit} = ((u_r t_{\rm E} \csc\phi)/\Delta t)^{1/2},\ \omega \equiv \boldsymbol{\mu}\cdot\mathbf{Z}/\theta_{\rm E}\ . \tag{2.14}$$

Thus, a caustic crossing can be fit to a five-parameter function of the form of Equation (2.13), the parameters being $a_{\rm crit}, t_{\rm cc}, a_{\rm other}, \Delta t$, and $\omega$ (plus the two parameters $F_{\rm S}$ and $F_{\rm B}$, derived/constrained from a global lens model involving the regions of the lightcurve not affected by finite source effects.).

### 2.2.3 Limb darkening

Observed stellar disks are not uniformly bright but appear to be darker towards the limb. This from our Sun well known phenomena is a geometrical effect. While approaching the edge of the disc the emergent angle of the observed radiation gets smaller with respect to the stellar surface and the optical depth of 1 (where the star gets opaque) is reached already in higher and cooler, i.e. darker layers of the stellar atmosphere. On the other hand, in the disc center one can see into deeper layers which are hotter and brighter.
Empirical limb darkening models for the surface brightness profile $\xi$ are usually expressed in the form (Claret 2000)

$$\frac{\xi(\mu)}{\xi_0} = 1 - \sum_i a_i(1 - \mu^i), \tag{2.15}$$

where $\mu = \cos\vartheta$ is the cosine of the emergent angle of the light ray from the star, $\xi_0$ the brightness at the center and $a_i$ ($i = 1/2, 1, 3/2, 2...$) are the so-called limb darkening coefficients (LDC).

The most common realizations are: the linear ($a_1 \neq 0$) and square root limb darkening ($a_1 \neq 0$ and $a_{1/2} \neq 0$). These limb darkened source profiles can then be modeled by

[7]For practical reasons this time is defined as the time when the limb of the star is tangent to the caustic, not when the center of the source is on the caustic. This way the beginning/end of the caustic passages can be easier predicted from the modeling for special photometric and spectroscopic monitoring.

integration over different sized uniform sources, with different brightness according to the used law, i.e. by dividing the source in rings. For a linear limb-darkened law however a closed semi-analytic form similar to Eq. (2.13) can be given (Schneider & Wagoner 1987), namely

$$A(t) = a_{\rm crit}\left[G_0\left(\frac{t-t_{\rm cc}}{\Delta t}\right) + \Gamma H_{1/2}\left(\frac{t-t_{\rm cc}}{\Delta t}\right)\right] + a_{\rm other} + \omega(t-t_{\rm cc})\ , \tag{2.16}$$

with

$$G_n(\eta) \equiv \pi^{-1/2}\frac{(n+1)!}{(n+1/2)!}\int_{\max(\eta,-1)}^{1} dx\,\frac{(1-x^2)^{n+1/2}}{(x-\eta)^{1/2}}\,\Theta(1-\eta)\,, \tag{2.17}$$

and

$$H_{1/2}(\eta) \equiv G_{1/2}(\eta) - G_0(\eta)\,. \tag{2.18}$$

The limb darkening coefficient $a_1$ hereby has been replaced by $\Gamma$ to avoid introducing an additional net flux term to the un-lensed source flux $F_{\rm S}$. The transformation between the two coefficients is given by

$$a_1 = \frac{3\,\Gamma}{\Gamma+2}. \tag{2.19}$$

Figure 2.7 shows an example lightcurve for a star crossing a straight fold caustic as well as the effect of different source surface brightness profiles: a uniform bright disc and two linear limb darkened profiles with $\Gamma = 0.5$ and $\Gamma = 1.0$.

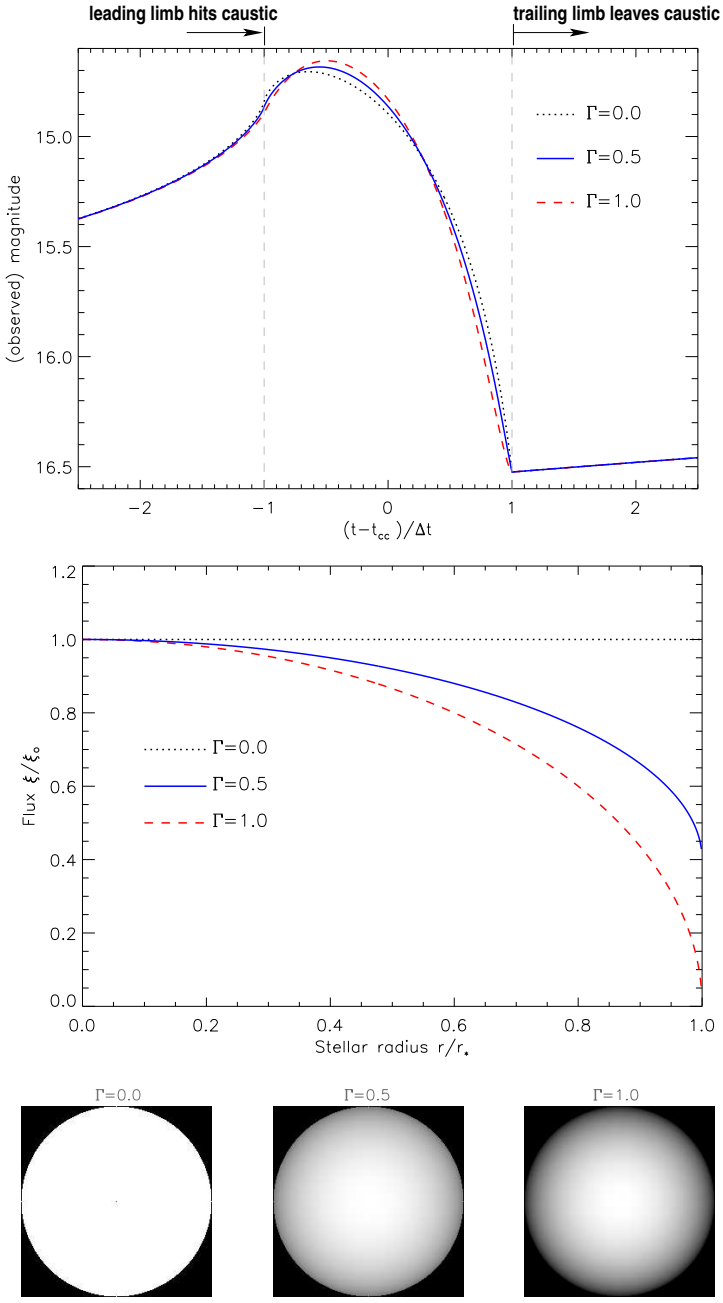


Figure 2.7: **Top:** A lightcurve showing the passage of a star over a straight-fold-caustic for different surface brightness profiles. A uniform bright disc ($\Gamma = 0$, black dotted line) and two linear limb-darkened profiles $\Gamma = 0.5$ (blue solid line) and $\Gamma = 1.0$ (red dashed line). The time axis is normalized to the caustic crossing time $\Delta t$, i.e. the leading source limb exits the caustic at $t = -1$ and the trailing limb at $t = 1$. **Middle:** The shape of the used brightness profiles as 1-dimensional cuts along the normalized stellar disc radius, with the same color scheme as above. **Bottom:** A two dimensional representation of the three surface brightness profiles. From left to right corresponding to $\Gamma = 0.0,\ 0.5,\ 1.0$.

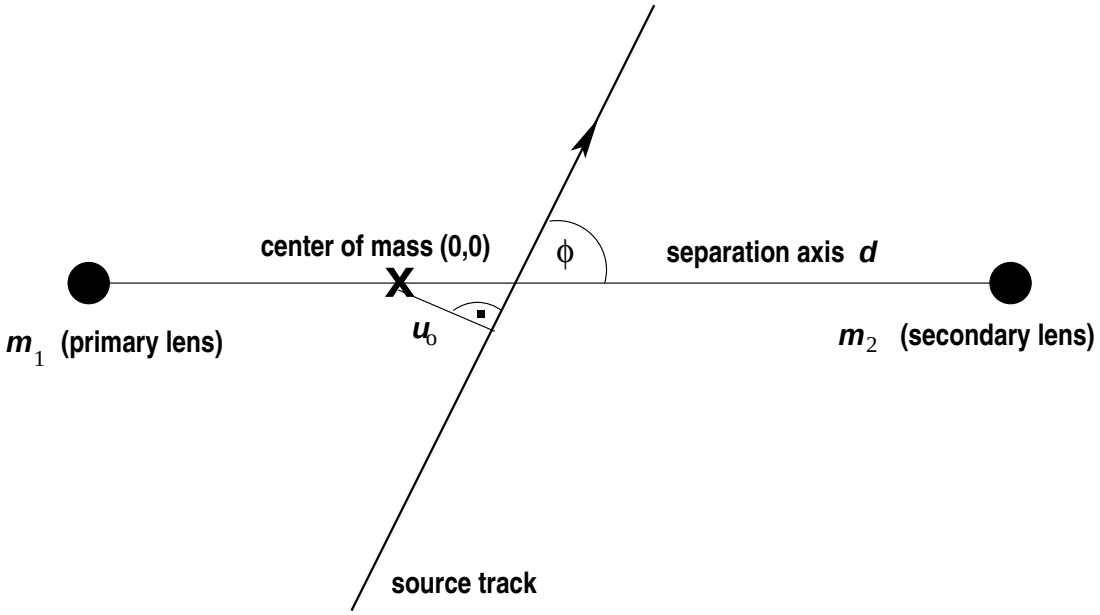


Figure 2.8: Standard coordinate system for binary lens parameterization. The binary axis lies on the x-axis and the more massive primary lens $m_1$ is located left from the origin (0,0), the center of mass. The impact angle $\phi$ is measured from the positive x-axis towards the source track.

## 2.3 Lightcurve parameterization

In addition to the 3 parameters, the minimum impact parameter $u_o$, the time $t_o$ at which $u(t) = u(t_o)$ and the Einstein time $t_{\rm E}$ describing the amplification of single lens (see Sec. 1.7, Eq. 1.17) one needs at least 3 more for the description of the amplification of a binary lens, namely the mass ratio $q$, the lens separation $d$ (measured in fractions of $\Theta_{\rm E}$) and the impact angle $\phi$ spanning between the source track and the binary axis. Including the un-lensed source flux $F_{\rm S}$ and blend contribution $F_{\rm B}$ for each observing site $n$ the measured flux can then be modelled with $6 + 2n$ parameters in the simplest case.

The complexity of nature however often demands a significantly larger parameter set. For example if finite source effects are present then the source size $\rho_*$ (in fractions of $\Theta_{\rm E}$) and 1 or more surface brightness profile parameters have also to be taken into account. Further observable effects include the motion of the Earth (see also Chapter 5), accelerated motion of the source or binary motion of the lens to name just the main higher order effects. Without doubt with the advent of 2nd generation microlensing campaigns this list will have to be extended, due to the improvement in photometric precision revealing more and more subtle lensing effects.

The lightcurves in the following gallery shall give only a short insight into the rich diversity of possible lightcurve shapes. For simplification they are unblended ($F_{\rm B} = 0.$), $F_{\rm S}$ has been set to 1 and rectilinear relative motion is assumed. Fig. 2.8 illustrates the here

adopted convention for the coordinate system in which the binary lens is described. Unless explicitly stated otherwise, the origin is the center of mass, the primary lens is located left of it and $\phi$ is measured from the positive x-axis towards the source trajectory.

### 2.3.1 Lightcurve gallery

The three different caustic topologies (Chapter 2) give rise to an enormous variety of possible lightcurve shapes. Single- or multi peaks (respectively dips, since the amplification can also become $< 1$) with sharp or smooth rises/falls can occur. The following figures shall serve to give a more illustrative idea of possible lightcurves without raising the claim of being complete.

Representing the star+planet lens scenario with a mass ratio $q = 10^{-3}$, three difference amplification maps (i.e. ([star+planet] − star) maps) for the three different topologies were selected, namely with separation $d = 0.71$ (Fig. 2.9), $d = 1.00$, (Fig. 2.10) and $d = 1.41$ (Fig. 2.11). They therefore have 3, 1, respectively 2 closed caustic curves. The reason why in the star+planet lightcurves the reference signal of a single star lightcurve was subtracted is to be able to display the planetary signature more clearly. Note that the dynamic in the amplification relative to the Paczyński curve $\delta$ can go up to $\sim 1$ mag.

Figure 2.12 then gives an example for a star+star lens with mass ratio $q \sim 0.3$ and separation $d \sim 0.3$. Here no reference signal was subtracted.
As source size we used $\rho_* = 0.001$ ($\sim 1\ R_\odot$, assuming a source distance $D_\mathrm{S} = 8$ kpc, lens distance $D_\mathrm{L} = 4$ kpc and lens mass $M = 0.3\ M_\odot$) for all cases, allowing for high amplitudes of the amplification signal.

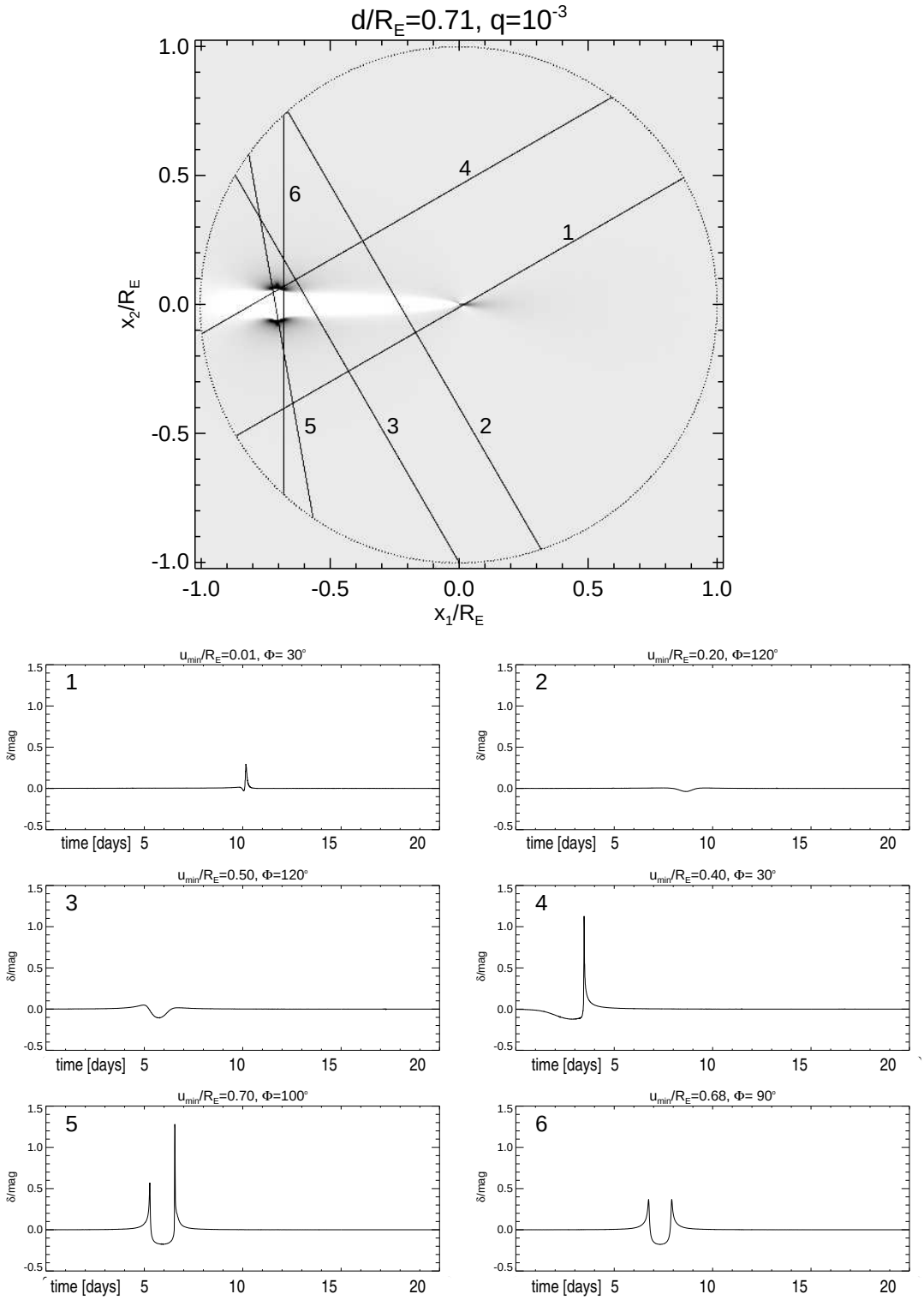


Figure 2.9: The planetary lightcurve signatures (difference lightcurves, where the star-only lightcurve has been subtracted) of the source tracks marked in the amplification map (**Top**) for the 3-caustic topology with planet-star separation $d/R_{\rm E} = 0.71$ and mass ratio $q = 10^{-3}$.

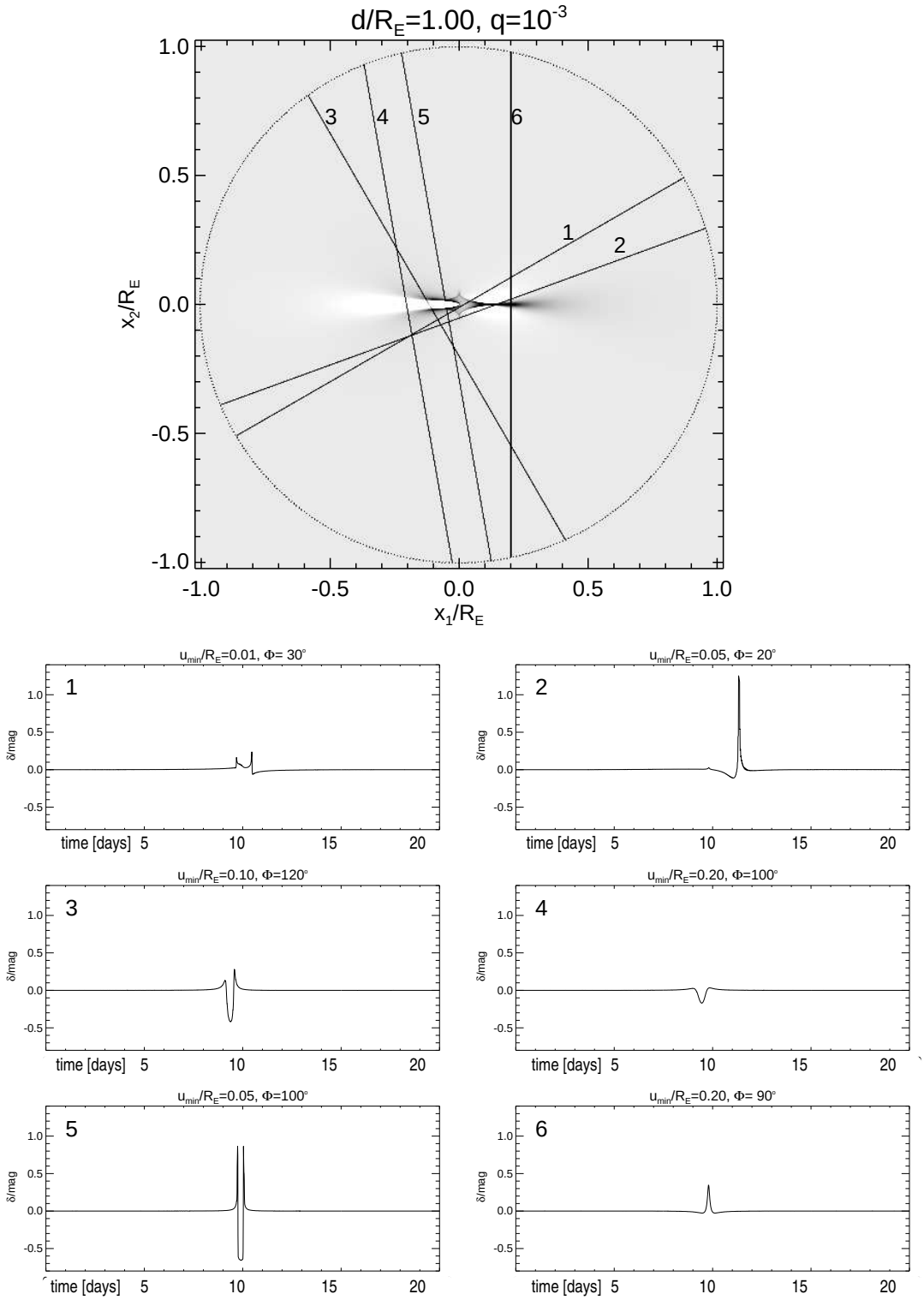


Figure 2.10: As previous Fig., but for a 1-caustic topology with planet-star separation $d/R_{\rm E} = 1.00$ and mass ratio $q = 10^{-3}$.

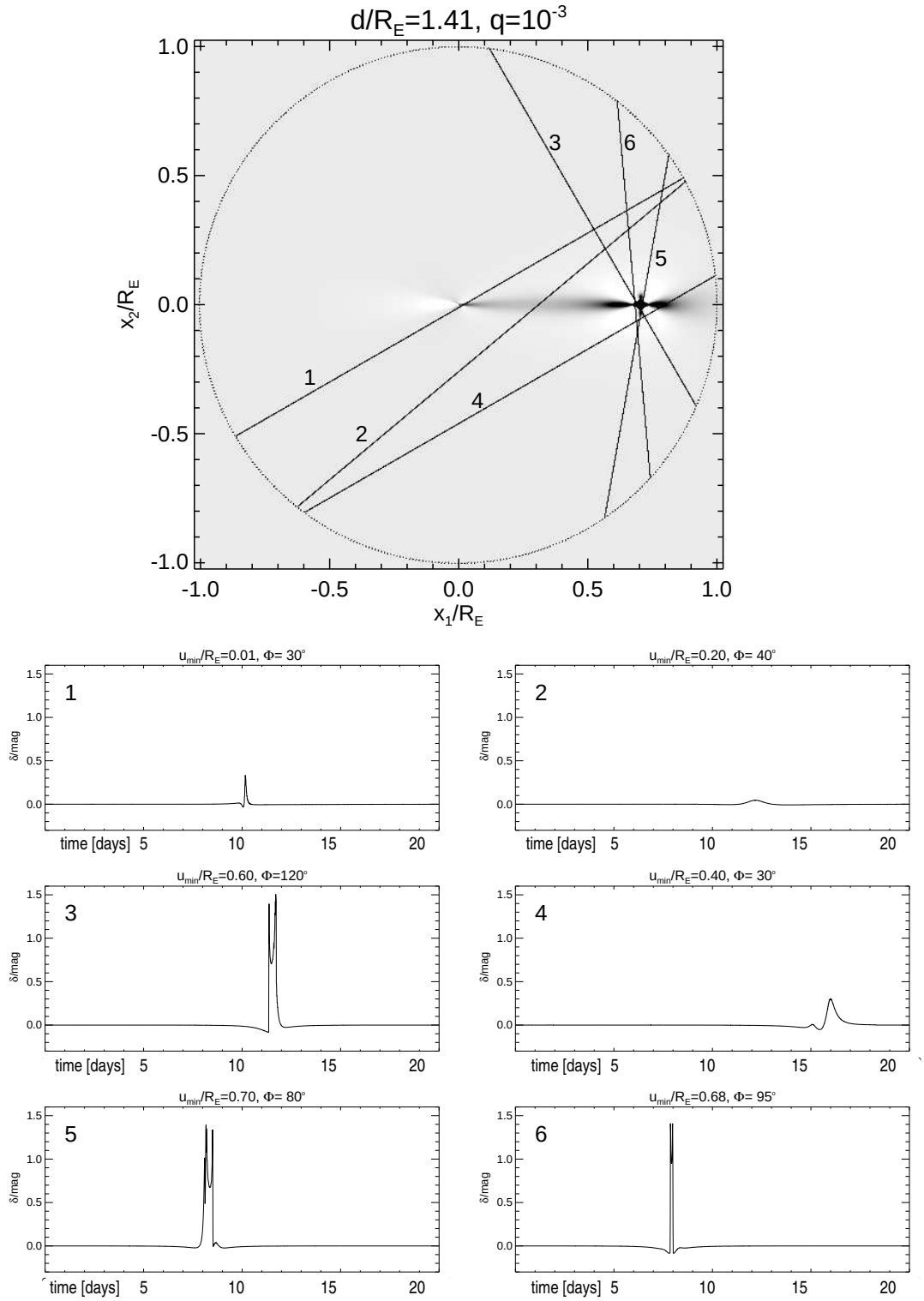


Figure 2.11: As previous Fig., but for a 1-caustic topology with planet-star separation $d/R_{\rm E} = 1.41$ and mass ratio $q = 10^{-3}$.

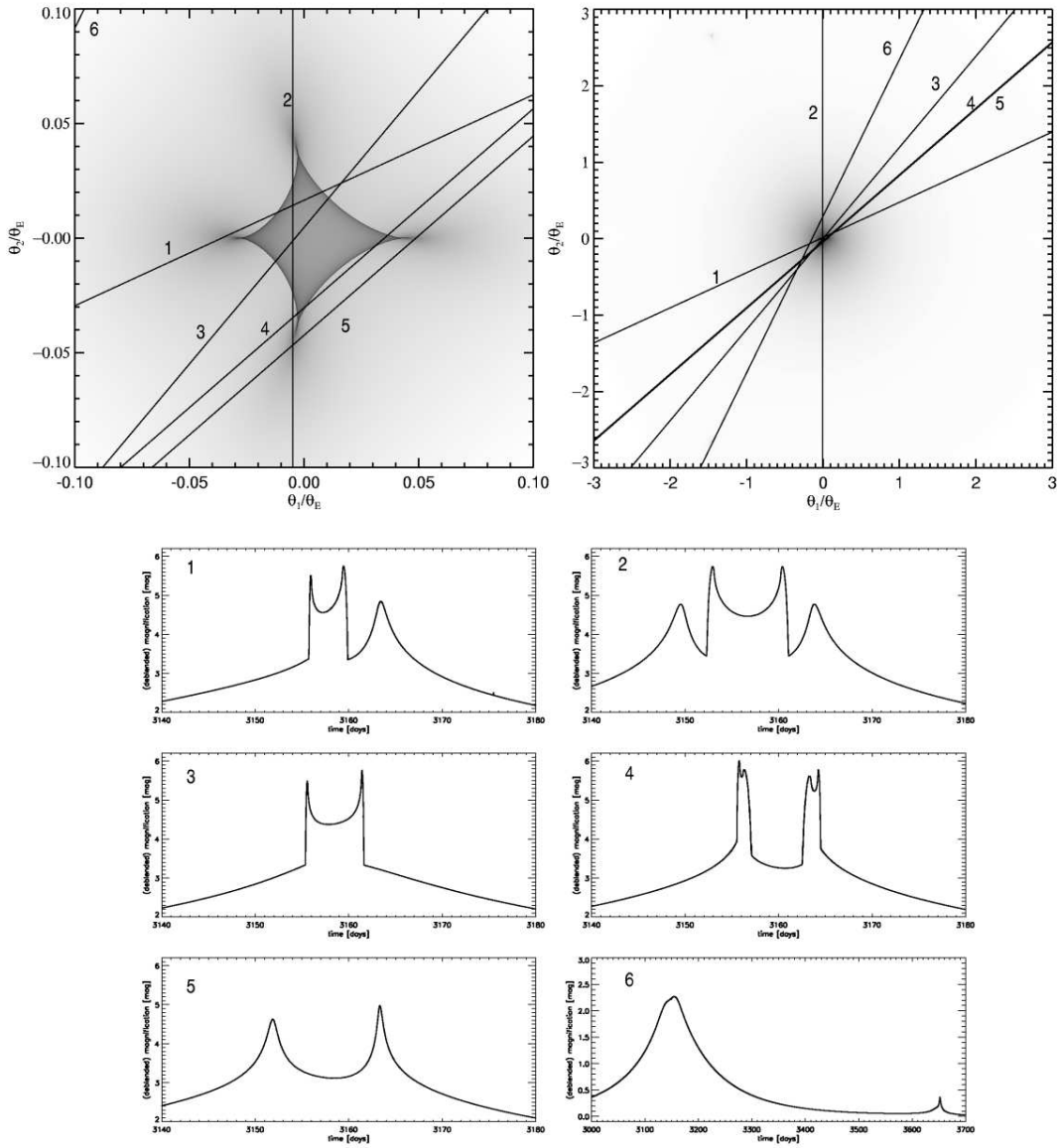


Figure 2.12: **Top**: Caustic structure of a star-star lens with $q \sim 0.3$, $d \sim 0.3$, with the right magnification map showing the full topology, including the secondary caustics. The numbered tracks mark the lightcurve displayed in the lower panels. **Bottom**: The lightcurves (blend-free and no reference curve subtracted) of the tracks marked in the magnification maps above. Note that the scale on plot 6 is different from the others in order to display more clearly the effect of the secondary caustic approach causing a small bump far from the central caustic peak.

# Chapter 3

# Global Optimization

> Test everything. Hold on to the good. Avoid every kind of evil.
>
> *1 Thess. 5:21-22*

## 3.1 Introduction

Posing the question asked in global optimization is simple: given a model, find the set of parameters which best describe the data. In principle there is also an easy answer, namely: try every possible combination of parameters (with a sufficient resolution, if the parameters are continuous) and keep the best. If your model is in a closed analytic form simply follow the curve discussion exercise you learned in school. Unfortunately in real life things are in general much more difficult. The number of parameters can be too large and/or their allowed ranges too wide for applying brute-force grid searches in a justifiable amount of computing time and/or the model is non analytic.

In the following it is assumed that the parameter space is not well suited for grid searches and that the model cannot be expressed in an analytic expression, which is the case in the problem of binary-lens-light-curve fitting. Before explaining the approach investigated in this work I want to present a short overview of some of the current and commonly optimization techniques around to put the strategy chosen by us into a context.

### 3.1.1 Downhill and direction set algorithms

One of the most often used optimizing methods is based on the downhill[1] simplex method by Nelder & Mead (1965) and its most popular incarnation Amoeba (Press et al. 1992). Part of the reason for its popularity is without doubt that it is easy to implement, quick and in general quite robust. Its working scheme is also quite depictive. Starting from a seed point $p_o$ in $n$-dimensional model parameter space you define $n$ more points by following a

[1] Depending on how you define optimization task, i.e. minimization or maximization, you might as well use the term uphill or hill climbing. Here we will stick to the terms minimization and downhill.

recipe like $p_i = p_o + \lambda_i e_i$, where $e_i$ are unit vectors and $\lambda_i$ constants which define a first characteristic length scale of the corresponding parameter space. These n+1 points form the vertices and their interconnecting lines the sides of a so called simplex. For example if your parameter space is 2 dimensional the simplex would be a triangle. By comparing the goodness-of-fit measure at each vertex/solution a gradient can be defined, without the need for calculating derivatives. Using the three geometrical transformations reflection, expansion and contraction the simplex moves along the path of steepest descent until the difference between all vertices has fallen below a given tolerance. Obviously this strategy runs into problems when your starting simplex is located in a large flat region of the chosen goodness-of-fit space and when the desired global minimum is hidden by local minima of either numerical nature or truly ambiguous solutions. The simplex method is therefore a good local optimizer but poorly suited for locating a global extremum. For example the tests done by (Vermaak 2003) show that Amoeba fails to locate the true solution if the seed parameters deviate roughly by more than 5% in the case of binary-lens-lightcurve fitting. Since in practice one almost never can come up with such a good first guess, this approach is not recommended as first weapon of choice to explore the solution space.
While the simplex lives in an $n$-dimensional space, direction set algorithms as the Powell method work along in one-dimensional directions of the parameter space. Since it is much easier to minimize a one-dimensional function (using bracketing for example), the idea is to start from an initial point and initial (vector) direction and successively minimize along lines in the parameter space. The Powell algorithm (Press et al. 1992) ensures that the search directions stay mutually independent in order not to spoil previous minimization progress. Again, this strategy yields fast and good results only if you are already rather close to an acceptable solution, and gets lost in large and highly nonlinear parameter spaces. Finally it is worth mentioning that a-priori both methods do not constrain the allowed parameter values. This is a potential pitfall for problems, where parameters have to obey mathematical or physical restrictions. For example in our case the mass ratio is non negative. To avoid parameter violations a possible strategy is to 'punish' forbidden parameter ranges by setting the goodness-of-fit measure to a bad value there or re-parameterize the model, but such interventions have to be made with care to achieve stable algorithm implementations.

### 3.1.2 Annealing algorithms

A crystal is the state of minimum energy for a slowly cooling down (=*annealing*) liquid metal. The emphasis here lies on *slowly*, to give the atoms or molecules time for their redistribution during the cooling process. Fast cooling will lead to polycrystalline or amorphous states of higher energy. The trick of nature to find this minimal energy state is that according to the laws of thermodynamic the energy states $E$ of system in thermal equilibrium at temperature $T$ follow the Boltzmann probability distribution $P(E) \propto e^{-E/kT}$. This ensures that even at low temperature there is a small chance to be in a higher energy state and so the system can occasional go *uphill* to escape from a local minimum. This behavior of sometimes disregarding a possible better candidate state to explore other states of the

configuration/model space was first put into an algorithm by Metropolis et al. (1953) which was the seed for a large variety of annealing algorithms. One current realization of this idea, the Metropolis-Hastings Markov Chain Monte Carlo (Geyer 1992) algorithm, defines the minimization process as a *Markov chain* $\{Z_k\}_{k=1}^{M}$ of length k, where each element $Z_k$ of the chain is a set of model parameters. The characteristic of a Markov chain is that it is a correlated sequence of random variables, where the probability of moving to state $Z_{k+1} = j$ given the current state $Z_k = i$ is independent of the $k-1$ states prior to state $k$. Naturally the more iterations, i.e. the longer the chain, the better the parameter space is explored in a stochastic way and the likelier the global minimum can be found. This strategy has been successfully applied on the problem of binary lens modelling by Rattenbury (2003). Unfortunately a direct performance comparison between his code and the one developed here cannot be made, since they operate on complete different computational resources. On the one hand a cluster of 400 CPUs (called Kaláka) at the University of Auckland for the Rattenbury's Markov-Chain code and on the other hand a single workstation, respectively PC for the TANGO code, which will be introduced below.

### 3.1.3 Neuronal networks

Being inspired by the fact that a sum of rather simple interconnected processing units (neurons) as the human brain is capable of performing quite some complex tasks, the design and use of artificial neural networks has attracted a lot of interest since the late 1950s. Capturing the essence of its biological counterpart an artificial neuron receives a number of weighted input signals (either from original external data/input or from other neurons in the network) and if the sum of these inputs exceeds a certain threshold the neuron *fires* a signal (passed thru an activation/transfer function) to its connected neighbor neurons or the output of the network. In a typical *feed-forward* network the signal flows from the (external) inputs via layers of neurons (where each layer is fully connected with the adjacent layers) to the output neurons. Using a training library of models and test data to teach the network which input (data) corresponds to which output (model), the network can then be used to find a model (within the parameter ranges of the training set) for real data, thanks to its ability of interpolating complex and nonlinear mappings from data to model. Vermaak (2003) first applied a neural network to the problem of binary-lens-lightcurve fitting. While his network was quite successful on ideal simulated data sets (i.e. regular sampling and no scatter) it could not handle gaps in the data. Although interesting, a lot of further studies are needed to decide if neural networks are suited for this particular problem.

### 3.1.4 Genetic algorithms

At least since Darwin (1859) we know that the driving mechanism of evolution is *natural selection*, which ensures that on average 'fitter', i.e. better adapted, individuals reproduce more often. In order to make the selection work, two main principles are needed. First, offsprings must inherit the characteristics that make its parents fit (i.e. *heredity*). Second,

there has to be at any time a spectrum of fitness among the population (i.e. *diversity*), otherwise natural selection cannot operate. Before having a closer look inside the working scheme of a genetic algorithm (GA) we need to define some more biological terms.
There are two different realizations of individuals (respectively models) in a GA. The *genotype*, which is the genetic construction plan for the individual stored in the DNA-sequence, and the *phenotype*, the actual living and breathing individuum. While nature uses 4 as base of the DNA, experience has shown that switching to the more familiar base 10 (or a binary base) has little effect on the performance of genetic algorithms (Charbonneau 1995). We further note that in the following the term *fitness* $S$ is synonym for goodness-of-fit, which in our case is the commonly used least-square test defined by

$$\chi^2 = \sum_i^n \left( \frac{y_i - y(x_i; a_1, ..., a_m)}{\sigma_i} \right)^2 \quad , \tag{3.1}$$

where $y_i$ is the data point, $y(x_i; a_1, ..., a_m)$ the corresponding prediction of the $m$-dimensional model at $x_i$ depending on the parameters $(a_1, ..., a_m)$ and $\sigma_i$ the error of the measurement. For clarity we note that since in our problem we deal with time series the $x_i$'s turn to $t_i$'s. Although the use of the $\chi^2$-statistic only applies in a strict sense to models that depend linearly on the $a_i$'s and for Gaussian distributed errors, it remains a useful measure if handled with care (regarding outliers for example) even if both assumptions are violated as it is the case in microlens-lightcurve modeling. Defining the *number of degrees of freedom* $(d.o.f.) = n - m$, where $n$ is the number of measurements and $m$ the number of parameters, a 'good' fit will have a $\chi^2 \sim d.o.f.$ on the background that the $\chi^2$ distribution has the mean $d.o.f$ and for large $d.o.f$ approaches the normal distribution.

With this in mind a top-level view of a GA would look like:

1. Construct a random initial population and evaluate the fitness of its members.
2. Construct a next generation population by *breeding* selected individuals of the old population and evaluate the fitness of these new members.
3. Replace old population by the new one.
4. Go to step 2 until a prescribed number of generations is reached or the fittest individuals match the desired goodness of fit.

All the 'magic' of a GA lies in step 2, the breeding of selected individuals. Before we reveal the trick of the selection process let us have a look at the breeding process shown in detail in Fig. 3.1 for a two dimensional model with parameters $q$ and $d$. To build the gene sequence (respectively the genotype) the significant digits from the model parameters are cut out and stitched together[2]. The two selected parent genotypes reproduce

[2]Note that in the GA investigated here, Pikaia (Charbonneau 1995), the model parameters are remapped to the interval [0,1] prior to their encoding. Besides enabling bounds on the parameters useful for constrained optimization, this allows the easy cut-and-stitch-encoding recipe presented here.

themselves by exchanging (i.e. *crossover*) their genes at a prescribed gene position thereby creating two offsprings. Additionally a gene of the offspring can be subject to *mutation* to enhance diversity in the population. They are decoded again into model parameter space to compute their $\chi^2$ and infer their fitness. To find out which individuals/models become a couple and are allowed to reproduce, Pikaia spins the so-called *Roulette-wheel* algorithm (Appendix A.1). The probability for an individual $i$ of being selected for breeding is therein defined as the probability of hitting a wheel sector of angular size $\hat{S}_i/(2\pi F)$, where $F$ is a normalization constant and $\hat{S}_i$ the *relative fitness* of the individual. The reason for introducing this relative fitness and not taking the $\chi^2$ directly as selection criteria is to avoid premature convergence by privileging good models too much and in this way sustain besides mutation the diversity within the population. Using a *ranking* strategy, where based on its (absolute) fitness a rank $r_i$ to each individual is given, so that $r = 1$ marks the best adapted individuum and $r = n_\mathrm{p}$ the least adapted in a population of size $n_\mathrm{p}$, the relative fitness is defined as

$$\hat{S}_i = \frac{n_\mathrm{p} - r_i + 1}{n_\mathrm{p}} \quad . \tag{3.2}$$

This way a fitness differential for each generation is ensured that is independent of the actual distribution of fitness values. Natural selection then always has a choice and the possible parameter space can be globally explored. In practice this exploration process is illustrated in the flip-book movie shown in Fig. 3.2 for the example of optimizing the 2-dimensional function $f$ defined as

$$f(x,y) = [16x(1-x)y(1-y)\sin(n\pi x)\sin(n\pi y)]^2, \qquad x,y \in [0,1],\ n = 1,2,... \tag{3.3}$$

with $n = 9$ in this case. This function is a nightmare for classical optimization codes, since it is virtually plastered with local minima (to be exact there are 81 minima for $n = 9$). In the random initial population, only a few individuals lie anywhere near the tallest peak and none close enough for local hill-climbing algorithms. After only ten generations the population in the outer low-level regions has been decimated and groups of the population have converged on some peaks close to the highest central peak. As generations go by, a few individuals have been catapulted by crossover and mutation to the wings of the central peak, where rapidly a base camp is established. Favored by natural selection this subgroup now gradually conquers the central peak at expense of its neighbors. By the 40th generation basically the whole population now resides on the highest mountain, with only a few mutants occasionally appearing in some other locations. In the 90th generation the sporadic explorations still have led to no new discoveries and the central peak appears to remain the best environment for the inhabitants of this landscape. For some applications the best individual of the last generation may not be good, respectively accurate enough, but this can easily be improved by handing this individual over to local gradient optimizers such as Amoeba or Powell as introduced above.
Fig. 3.3 explains why there is no straight forward termination criteria based on $\chi^2$ gradient information in GAs. The convergence behavior as function of number of generations reveals a stair like structure with stairs of different width, which make criteria that compare the

differences between generations in terms of their adaption success not reliable. While an absolute $\chi^2$-threshold in principle could do the job, fixing its value can be tricky in cases where the gaussianity of measurement errors is questionable as in the real life microlensing data. Therefore it is more practical to let the GA run for a prescribed number of generations and then switch to a gradient optimizing routine such as Amoeba or Powell for final refinement and final stop. This then however brings up the question of defining a prescribed number of generations.

It is no secret to any modeler that the performance of an optimizing routine depends on the posed problem. There is no cure-all recipe that works equally well in every model and parameter space. Often the only way is trial and error and/or a systematic empirical study of the behavior of the algorithm on a test case like the one described in the next section 3.2 which is as close to the real thing as possible. Among the control parameters of a GA, the population size and the number of generations are the most influential controls for the effectivity and directly determine the estimated CPU-time. In the (at least in GA literature) absence of a mathematical strict prescription, a series of test runs on an artificial data set was performed to find a reliable setup for our algorithm, as explained below (Sec. 3.2.3).

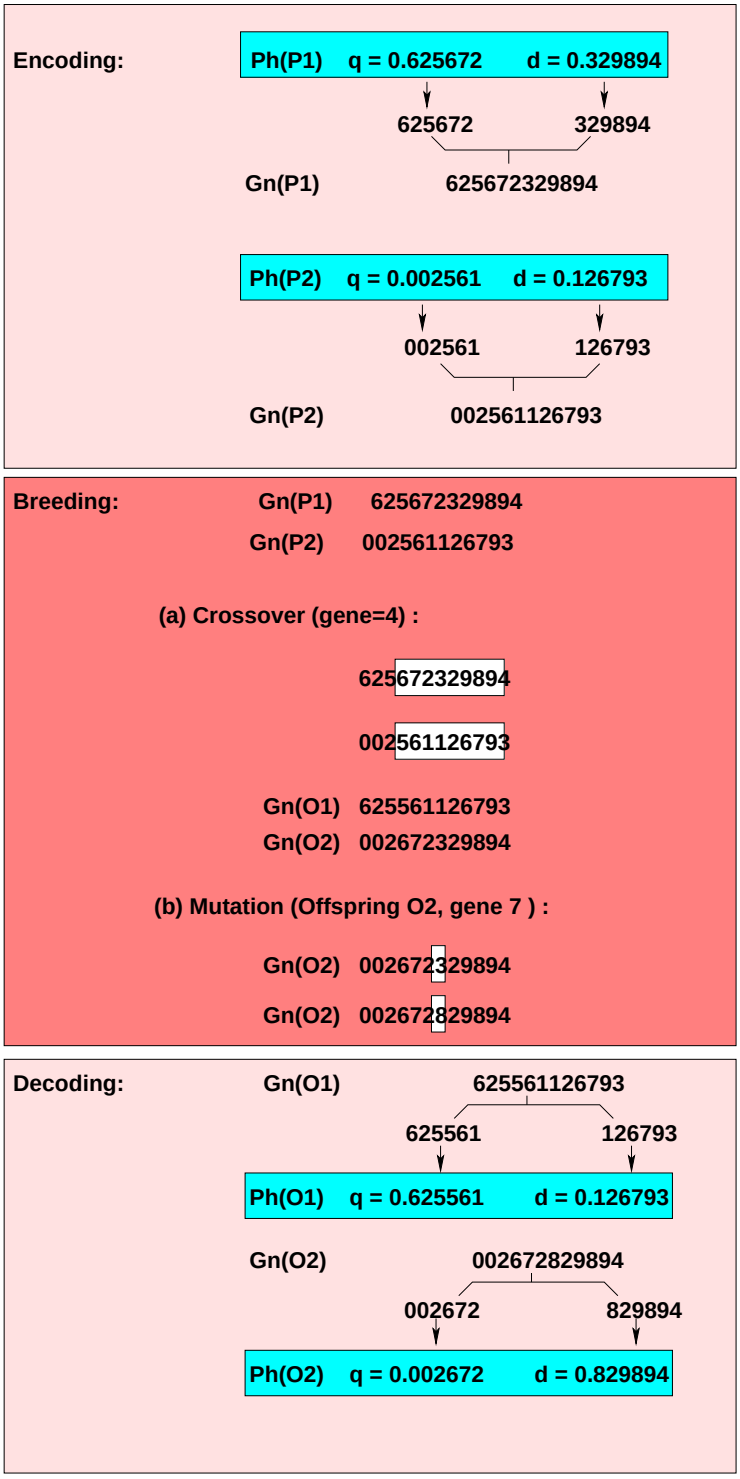


Figure 3.1: Encoding, breeding and decoding in genetic algorithms. The models (phenotypes) in this example are 2 dimensional and chosen to be the mass ratio $q$ and the lens separation $d$. The parameters are encoded into a real decimal 12-digit string (6 for each parameter), the genotype. 'Ph(P1)' translates to 'phenotype of parent 1' and 'Gn(02)' means 'genotype of offspring 2'. Note that one breeding event creates two offsprings and that both crossover and mutation operations occur only if a given probability threshold is passed, i.e. offsprings can also be true clones of their parents.

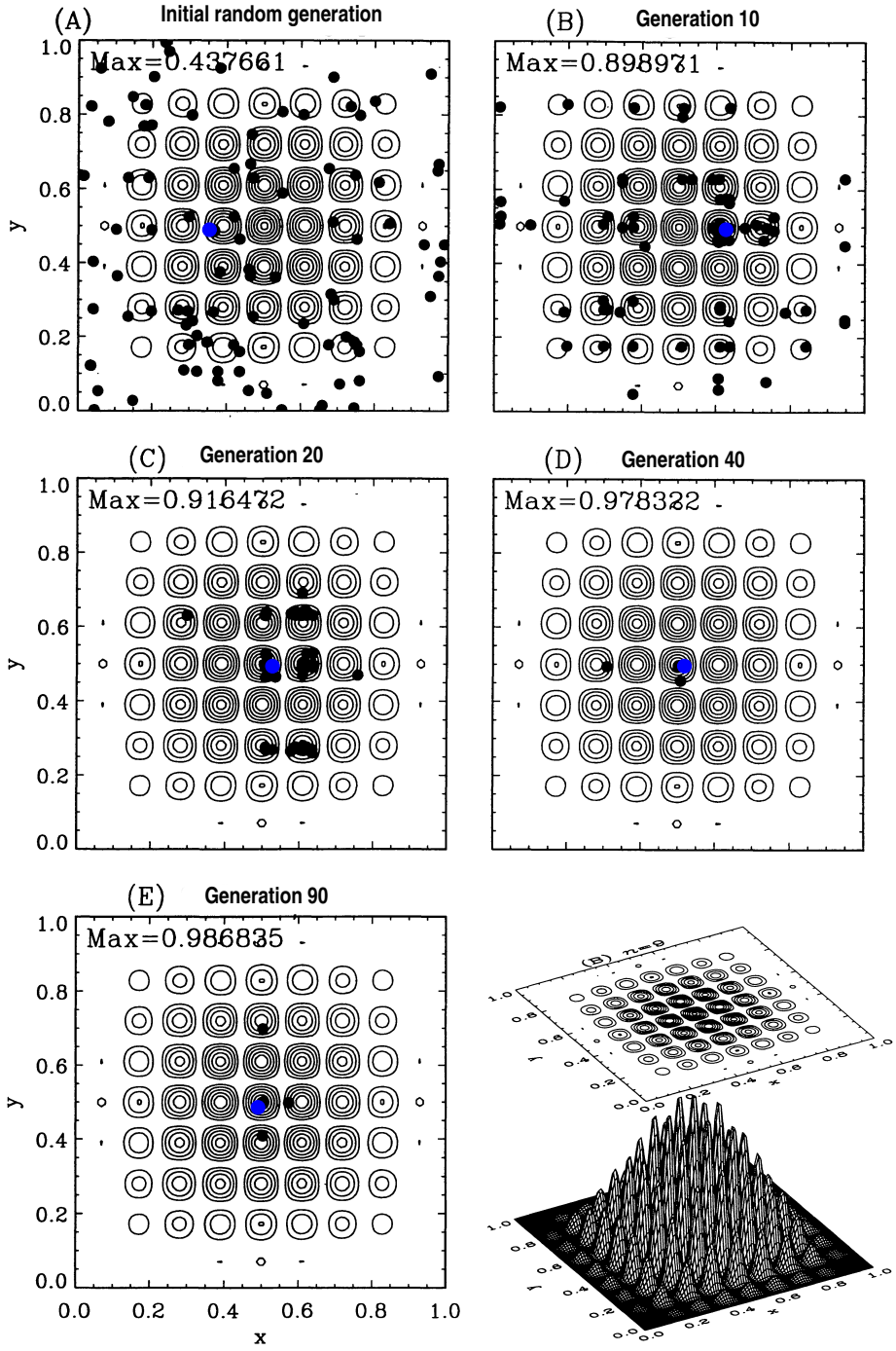


Figure 3.2: Example of Genetic Algorithm optimization exploration of the intricate 2-dimensional parameter space of the function $f$ (see text) displayed in the lower right corner. The filled black circles represent individual members of the population of size 100. The bold blue circle marks the fittest/best individual. Starting from the initial randomly distributed first generation (top left corner), the evolution of the population is shown for generations, 10, 20, 40 and 90. (Adopted and modified from Charbonneau (1995))

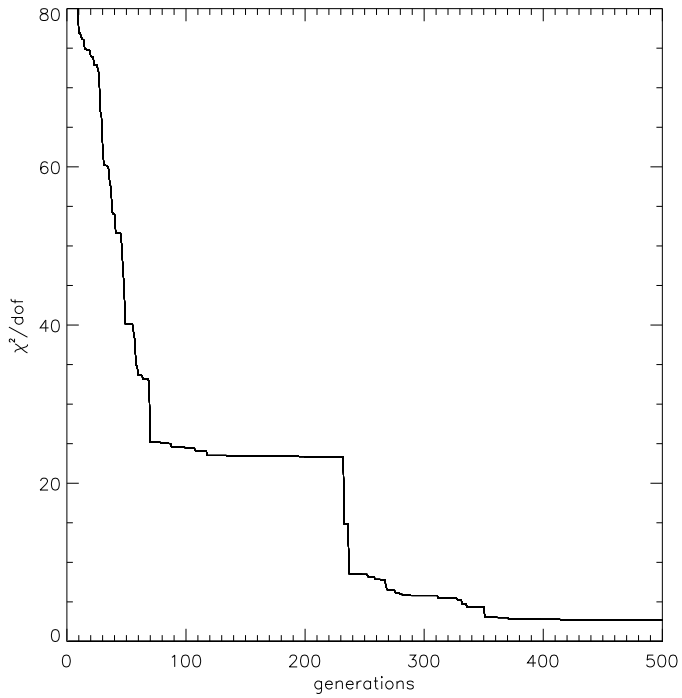


Figure 3.3: A typical example of how the goodnes-of-fit converges in a genetic algorithm over the course of 600 generations. Any termination criteria based on a gradient of $\chi^2$ can be fooled easily by short and long periods of stagnation, manifested in the numerous stairs of different width.

## 3.2 TANGO: a binary lens fitting code

A main part of the thesis work was devoted to develop a new and user friendly binary-lens-fitting routine, which was named TANGO (**T**ool for **AN**alyzing **G**ravitational lens **O**bjects), to analyze the microlensing data of the PLANET collaboration (see Sec. 4). TANGO makes use of the genetic algorithm Pikaia (Charbonneau 1995) and the simplex optimizer Amoeba (Press et al. 1992). It calculates the amplification of point sources by solving the 5th order polynomial of the binary lens equation (2.3), uses ray-shooting (Wambsganss 1999, see also Sec. 2.2.1) for extended source as well as the straight-fold-caustic approximation (Schneider & Wagoner 1987, see Sec. 2.2.2). While a short guide to the code is given in Appendix A, the following Section focusses on its application and performance on simulated data and later, in Part II of this thesis, on its successes on real events.

### 3.2.1 Simulated events

To test how TANGO performs in the often quoted highly intricate and complicate parameter space of binary lenses we simulate a typical caustic crossing binary lens event. In this context typical stands for choosing a sampling rate and photometric accuracy based on current available data sets from PLANET (Albrow et al. 1998), OGLE (Udalski 2003) and MOA (Bond et al. 2004). This means that in general, since the first caustic passage of such an event is practically not predictable[3], the caustic entry is less well sampled than the exit.

We choose a data set where both caustic crossings are visible in the data and also ensure a rather complete coverage of the lightcurve. The reason for being that picky is that even well sampled lightcurves are plagued by ambiguities (Dominik 1999a; Gaudi & Han 2004) and studying the well known fact that one basically can fit 'anything' to a poorly sampled light curve seems not very valuable.

The artificial data are drawn from an amplification map convolved with an extended limb-darkened source. To mimic the effect of irregular but strategic[4] sampling, several time windows can be defined (for example covering the caustic plateau or the caustic exit) with different ideal sampling rates, from which the data points are randomly picked (to simulate gaps due to technical failure and/or bad weather). We then convolve the data with Gaussian noise on both measurements and errors, whereby we use a magnitude dependant relation for the photometric errors $\sigma_i$ of the form

$$\sigma_i = \frac{\sigma_o}{1 + \Delta m_i} \ , \tag{3.4}$$

where $\sigma_o$ is the photometric precision at baseline and $\Delta m_i$ the de-blended magnitude of measurement $i$, to reflect the fact that the photometric precision improves as the brightness

[3]During the rise towards the caustic entry, the ambiguities in the model space are enormous and in general the data of the rising can be easily fitted by single lens models, hiding hints for a caustic entry.

[4]Depending on the assumed nature and status of the event, the observing strategy in campaigns like PLANET is permanently adapted and changed in real time in order to try to cover critical regions, as the caustic exit, with sufficient quality.

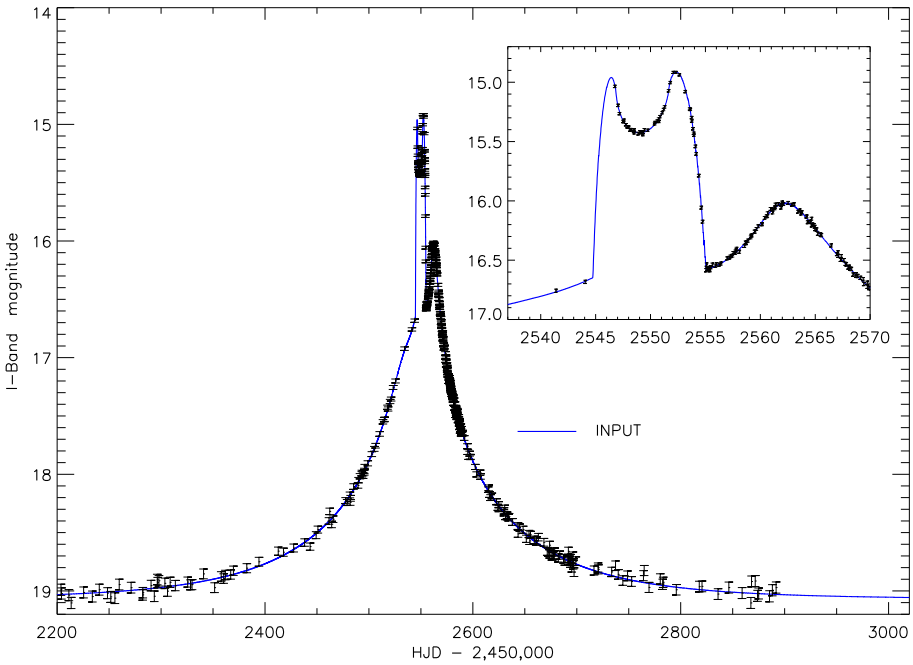


Figure 3.4: Simulated data set of a typical binary-lens event with a fold caustic passage. While the practically unpredictable caustic entry is poorly sampled, the caustic exit and the following cusp approach is well covered. At baseline the photometric precision is $\sim 5$ %. For the caustic passage and the cusp approach an accuracy of about $\sim 1$ % is reached.

of the target rises. To avoid however unrealistic small error bars we limit the maximal achievable photometric precision to $\sim 0.5\%$. Figure 3.4 shows the lightcurve of the artificial event (AE-1) and Fig. 3.5 the corresponding lens geometry.

For simplicity we assume a homogenous data set, i.e. the 'measurements' are taken from a single 'observing site', and a linear relative motion between observer, lens and source. Noting that the surface brightness profile of the source is modelled with a linear limb darkening law (see 2.15), we are left with 10 parameters underlying our simulated binary lens event. These are the mass ratio $q = 821$, separation $d = 0.372\ R_{\rm E}$, impact angle $\phi = 193.1^o$, impact parameter $u_o = 0.027\ R_{\rm E}$, impact time $t_o = 2550.000$ HJD$'$, Einstein time $t_{\rm E} = 164.00$ days, un-lensed source light $F_{\rm S} = 19.256$ mag, blended light $F_{\rm B} = 21.083$ mag, limb darkening parameter $\Gamma = 0.51$ and source size $\rho_* = 0.0059\ R_{\rm E}$. Since the calculation of extended source effects with respect to the complete lens model is computational expensive (Sec. 2.2) the fit strategy is to separate data which are affected by finite source effects from data where the point source approximation is valid. In cases when no clear distinction can be made the only remaining options for modeling are CPU-intensive grid searches on ray-shooting maps or image plane integration schemes.

A first look on the AE-1 lightcurve reveals 2 caustic passages, a caustic entry at $\sim$ 2545 HJD$'$ and an exit at $\sim$ 2555 HJD$'$, where HJD$'$ = HJD $- 2,450,000$. While the entry

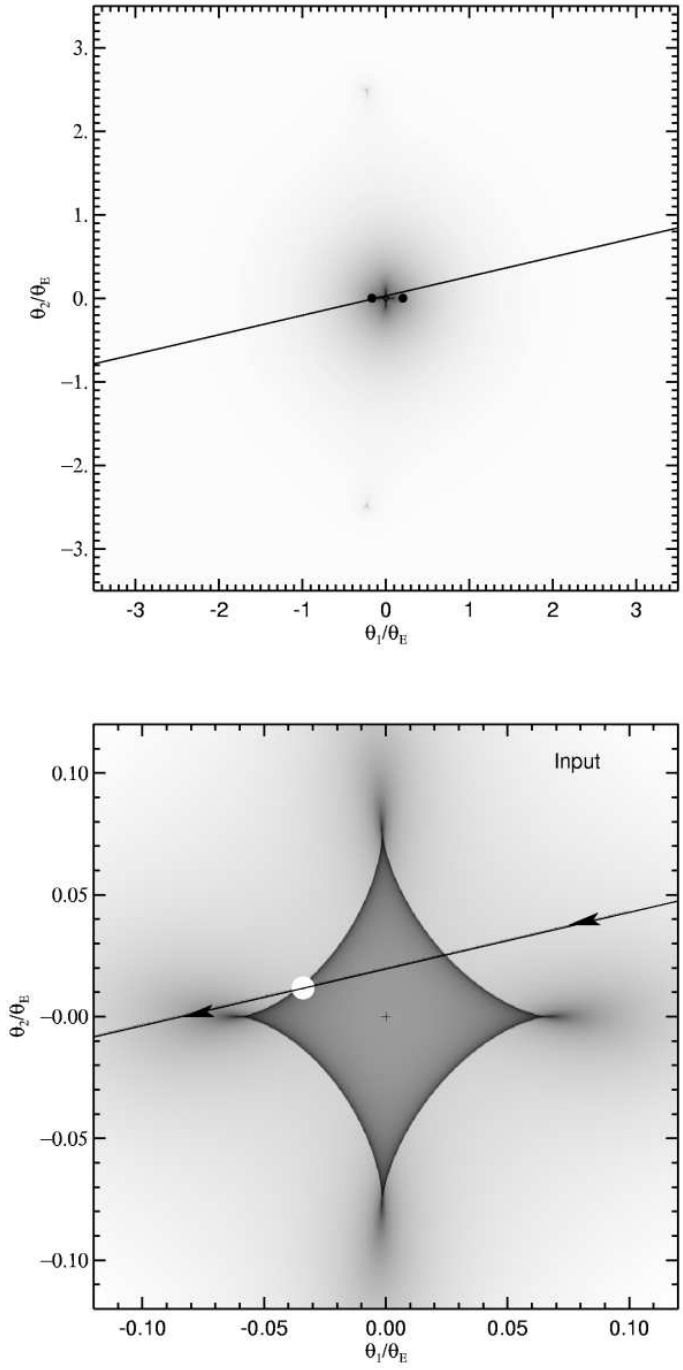


Figure 3.5: The input model: A binary lens with mass ratio $q = 0.821$, and separation $d = 0.372$. The solid line marks the trajectory and direction of motion of source. The **upper** amplification map displays the complete topology with the central caustic and the two triangular secondary caustics. The filled black circles indicate the position of the lens components. The **lower** map shows a zoom onto the central caustic. The white filled circle here represents the source scale.

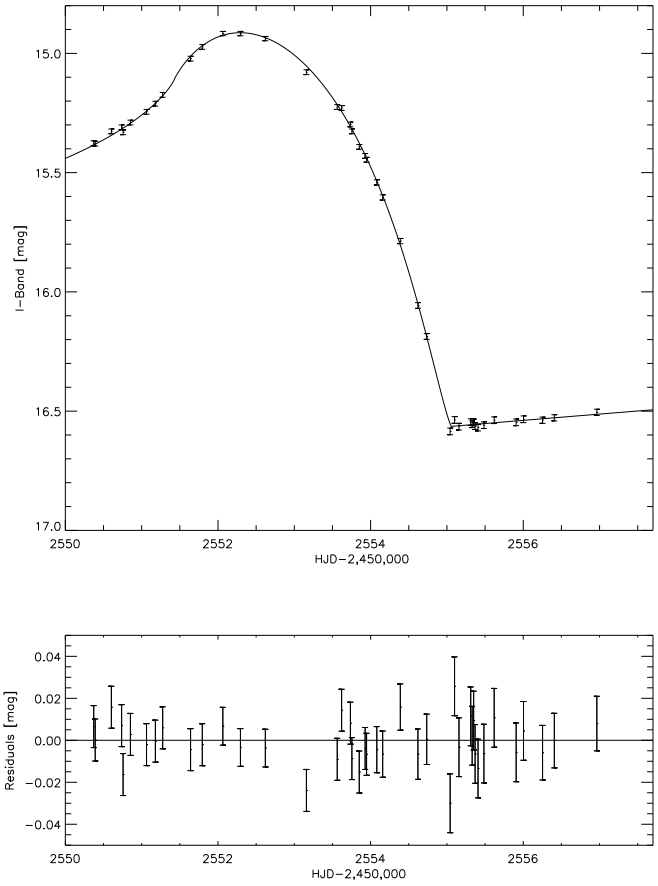


Figure 3.6: The best fit model for the caustic exit and its residuals, derived from the straight-fold-caustic approximation (For parameters see Table. 3.1).

is only sparsely sampled, the exit has a fairly complete coverage and can provide useful constraints on the source and the complete photometric model. Performing an optimization of a straight-fold-caustic model with linear limb darkening (Sec. 2.2.2) on the caustic exit, picking 'by eye' the time range from 2550.0 HJD′ to 2558.0 results in the model shown in Fig. 3.6 with the parameters given in Table 3.1

To exclude the data points which are affected by finite source effects we apply the argument given in Albrow et al. (1999a) . There it was shown, that for times $\gtrsim 3\Delta t$ away from the fold caustic, where $\Delta t$ is the time in which the source radius crosses the caustic, the point source approximation is accurate enough for photometric errors of $\gtrsim 1\%$. Based on the measured caustic crossing time(s) above we cut out data between $2544.5 \leq \mathrm{HJD}' \leq 2547.1$ and $2551.2 \leq \mathrm{HJD}' \leq 2557.0$.

Table 3.1: Derived linear limb-darkening coefficient and fold-caustic model parameters of the caustic exit of artificial event AE-1. (See Fig. 3.6 for the corresponding lightcurve)

| | Linear |
|---|---|
| $t_{\rm f}$ (days) | 2554.986 |
| $\Delta t$ (days) | 1.76 |
| $\omega$ (days$^{-1}$) | 0.21 |
| $a_{\rm crit}$ | 11.90 |
| $a_{\rm other}$ | 5.54 |
| $\Gamma$ | 0.64 |
| $\chi^2$/dof | 1.10 |

To explore the binary-lens-point-source space, several options are viable. For example one can let Pikaia do the job on its own leaving all parameters free and 'blindly' believe that the outcome is close to the global best solution. However this strategy would leave too many doubts about the crediblity of such a model, if it is the only base of analysis. Since the computation of the point-source models is reasonably fast ($\sim$0.03 sec for a data set with 500 measurements) it is worthwhile to sacrifice some computational efficiency for being more convincing and to get an overview over possible lens models by scanning the parameter space on a grid in mass ratio $q$ and separation $d$, the two parameters which characterize the lens.

We choose the grid to cover the range $q = 0.01, 0.05, 0.10, 0.15, ..., 1.00$ and $d/R_{\rm E} = 0.01, 0.05, 0.10, 0.15, ..., 5.00$. The space spanned by $d$ hereby is choosen in such a way that it corresponds to physical binary separations of $\sim 0.04 - 40$ AU for typical lens scenarios, i.e. ensures coverage of the most frequently observed separations (with a distribution peak around $\sim$ 30 AU as found by Zinnecker et al. (2004)). While larger and smaller separation binaries outside these bounds do exist, the caustics shrink rapidly to sizes of the order of the source and below in these cases leading to complete different lightcurve structures (see Sec. 7) which are ruled out a priori by the extended-source and caustic-passage effects seen in the lightcurve of our artificial event.

For the minimization on each grid point we apply a hybrid strategy, i.e. using Pikaia first and then Amoeba for refinement. The result of this grid search is displayed in Fig. 3.7, with dark greyscales corresponding to low $\chi^2$ regions and brighter greyscales to high, i.e unfavourable $\chi^2$s. Two regions of interest can be easily identified. In the lower part a dark strip stretching almost over the complete mass ratio range and a width in separation $d$ ranging from $\sim$ 0.7-0.2. In the upper part another pattern is visible, however not as dark (respectively deep) and with a more fuzzy cloudy appearance.

To locate the best model for each of the features, we conduct now parameter searches with all 6+2 binary-lens-point-source parameters being free, however bounded (in Pikaia) to the promising regions. For the close binary we choose as conservative bounds $q = [0.01, 1.0]$, $d = [0.1, 1.0]R_{\rm E}$, $\phi = [0, 360]^o$, $u_o = [0.0, 1.0]R_{\rm E}$, $t_o =$

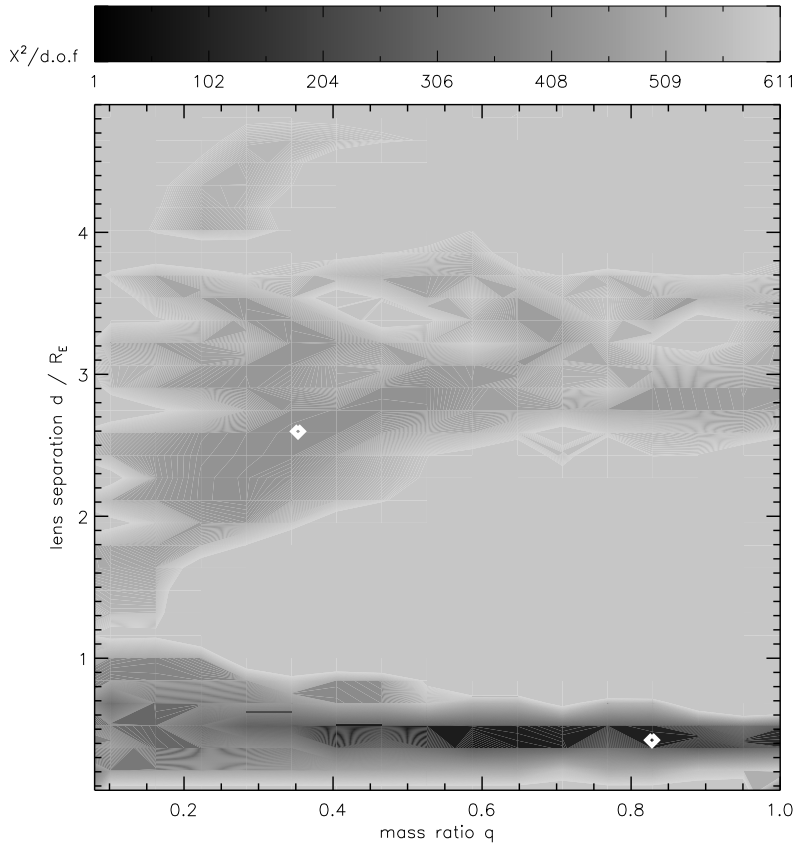


Figure 3.7: The scan of the mass-ratio-separation-$(q, d)$ grid (see text) reveals two interesting regions in the $\chi^2$-scape shown here. A dark (low $\chi^2$) strip stretching almost over the entire mass range and bounded in separation by $0.2 \lesssim d \lesssim 0.7$ and a fuzzy cloudy region in the upper part ($1.0 \lesssim d \lesssim 4.0$), which however nowhere is as dark (respectively deep). The white diamonds mark the best solutions found after bracketing the suggested minima and allowing $q$ and $d$ to vary freely during the optimization process.

$[2540.0, 2560.0]$ HJD$'$, $t_{\rm E} = [50, 300]$ days. To explore the wide binary solution space we restrict the parameters to $q = [0.01, 1.0]$, $d = [1.0, 5.0]R_{\rm E}$, $\phi = [0, 360]^o$, $u_o = [0.0, 5.0]R_{\rm E}$, $t_o = [2300.0, 2700.0]$ HJD$'$, $t_{\rm E} = [50, 300]$ days. Note that since there is no central caustic in the wide separation binary lens scenario, $t_o$ is not well constrained a priori from the data and one has to allow for much larger bounds than in the close binary case. As during the grid search the parameters derived from Pikaia serve as seed for Amoeba for refining the models. This way we find as best close binary solution $q = 0.828, d = 3.82$ as lens parameters (see Table 3.2 for full parameter set) and for the best wide model $q = 0.35$, $d = 2.59$ (both marked in the $\chi^2$ map with white diamond symbols). While the close model gives a very good fit (see Fig. 3.8) with no systematic residuals and a reduced $\chi^2$ of 1.1, the best wide model clearly fails to explain the data and is formally ruled out at the $> 10$ $\sigma$-level. The reason for the failure of the wide model lies in the fact, that the source trajectory of AE-1 also approaches a cusp and thus constrains the overall geometry

of the crossed caustic to be rather symmetric along the x- and y-axis and that this point symmetry behavior is in general more strict for central caustics of close ($q \sim 1$) binaries than for wide binary caustics, which are more elongated along the x-axis (see also Figures 2.1 and 2.2).

We note that if no acceptable global point-source-binary-lens (PSBL) fit would have been found this could have been an indication that the cusp approach may violate the point source treatment, but luckily this is not the case[5]. Being conservative, the causting crossing time gives us an upper limit via Eq. (2.12) for the source size $\rho_* = \frac{\Delta t}{t_{\rm E}} \sin\phi \leq \frac{\Delta t}{t_{\rm E}} = 0.011$. Using the also from the straight-fold-caustic model inferred source profile a best-lens-configuration map is convolved with source sizes from $\rho_* = 0.0001, 0.0002, ..., 0.0110$ to optimize the source size parameter, resulting in $\rho_* = 0.0062$. The Fig. 3.9 shows the caustic structure and lightcurve of the best found complete model.

| parameter | fit result | input |
|---|---|---|
| $q$ | $0.828^{+0.07}_{-0.07}$ | 0.821 |
| $d$ | $0.382^{+0.010}_{-0.011}$ | 0.372 |
| $u_0$ | $0.0286^{+0.0006}_{-0.0007}$ | 0.027 |
| $\alpha$ [deg] | $193.336^{+0.5}_{-0.4}$ | 193.1 |
| $t_{\rm E}$ [days] | $155.447^{+0.4}_{-0.4}$ | 164.000 |
| $t_0$ | $2549.963^{+0.10}_{-0.05}$ | 2550.000 |
| $r_*$ | $0.0062^{+0.05}_{-0.07}$ | 0.0059 |
| $\Gamma$ | $0.64^{+0.16}_{-0.17}$ | 0.50 |
| $h$ | $0.116^{+0.02}_{-0.02}$ | 0.157 |
| $\chi^2$/d.o.f. | 492.51/ 472 | 641.92 / 472 |

Table 3.2: Best Fit parameters with $2\sigma$ uncertainties in comparison to the 'true' input parameters.

[5]In real life of course there are many more possible causes for non acceptable fits indicating the presence of up to then unaccounted effects such as nonlinear relative motion, due to the Earth orbiting the sun (annual parallax) for instance, significant orbital motion of the binary lens or a more than two-body lens system to name just a few. In the 'controlled' environment of our simulations however we know here that at least these possibilities are ruled out as cause for potential trouble in fitting AE-1.

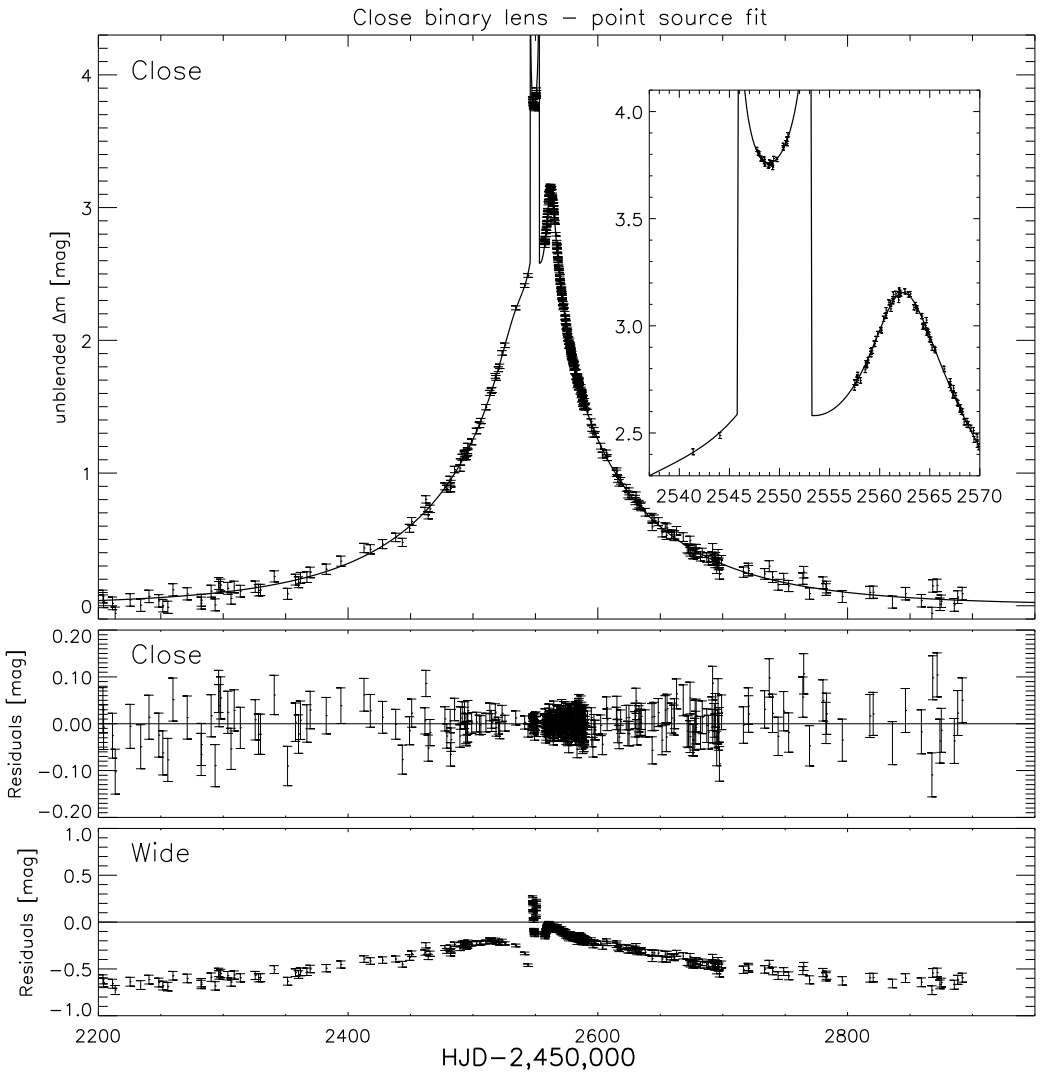


Figure 3.8: After bracketing in the promising regions in the $(q, d) - \chi^2$-map (Fig. 3.7), the best binary-lens-point-source model shown in the **top panel** is a close binary lens with $q = 0.828, d = 0.382, u_o = 0.0286, \alpha = 193.336, t_o = 2549.963, t_{\rm E} = 155.447$ and a $\chi^2/d.o.f. = 1.08$. Its residuals are displayed in the **middle panel**. The **lower panel** shows the residuals of the best wide binary lens model found at $q = 0.35, d = 2.59$, which is clearly inconsistent with the data. Note that at least the non-caustic region of the wide binary lens could in principle be reconciled with the data with a significant amount of negative blending, but since in the creation of data positive blending was added it was also restricted to be non-negative. However it is important to keep in mind that in real data, at least the ones reduced via Difference Imaging (Alard & Lupton 1998) negative blending can occur.

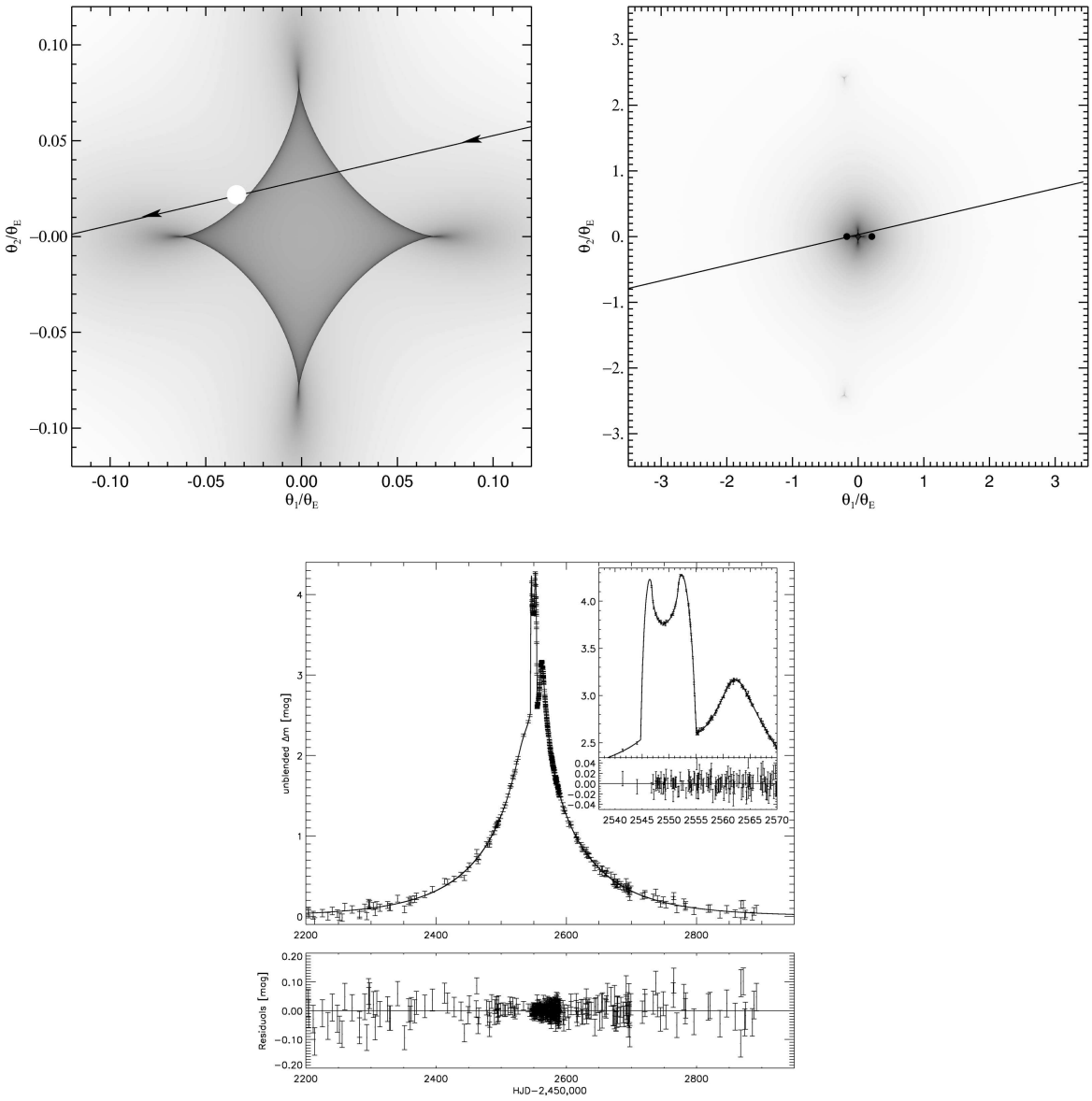


Figure 3.9: **Top:** Amplification maps of the best fit model, a $q = 0.828, d = 0.382$ close binary lens with one central caustic and two secondary (visible only in the large field map on the right). The white filled circle in central caustic map (left) marks the source size and the arrows indicate the direction of source motion (solid line). the positions of the lenses are marked as filled black circles in the big scale map on the right. **Bottom:** The corresponding lightcurves and residuals of the complete model. The inset is a zoom on the caustic passage and the subsequent cusp approach.

### 3.2.2 Error estimation

To assess the uncertainties of our parameter estimates we apply the marginalization technique, i.e. stated confidence intervals correspond to projections of the $\Delta\chi^2 = \chi^2 - \chi^2_{\min} =$ const. hyper-surfaces onto the parameters axis. Assuming 1 degree of freedom, the intervals $\Delta\chi^2 = 1, 4, 9$ are then the $1\sigma, 2\sigma, 3\sigma$ errors. In practice we vary the parameter we are interested in, on a one-dimensional grid around its found minimum, while optimizing the remaining parameters to generate plots as shown in Fig. 3.10 where one can read off the specific confidence intervals. The scatter of the points in these plots partly reflects the failures of Amoeba ('fed' with a seed point from Pikaia) and partly the roughness of the different $\chi^2$-hypersurfaces. For completeness we note that since the fit of source and blend flux is a linear problem, the uncertainty of the blend fraction can be more easily computed directly assuming the standard error propagation law $\sigma_F^2 = \sum_i \sigma_i^2 \left(\frac{\partial F}{\partial y_i}\right)^2$. Comparing the best-fit parameters to the known true model parameters shows that the majority is within $2\sigma$ of the truth, the mass ratio and separation even within $1\sigma$. The only 'outlier' $t_{\rm E}$ has a relative error of $\sim 6$ %, which is acceptable having in mind that a large fraction of data (close to baseline) has an accuracy of $\sim 5$ %. All in all this result is more than encouraging and raises some trust in TANGO for its application on real data in Part II.

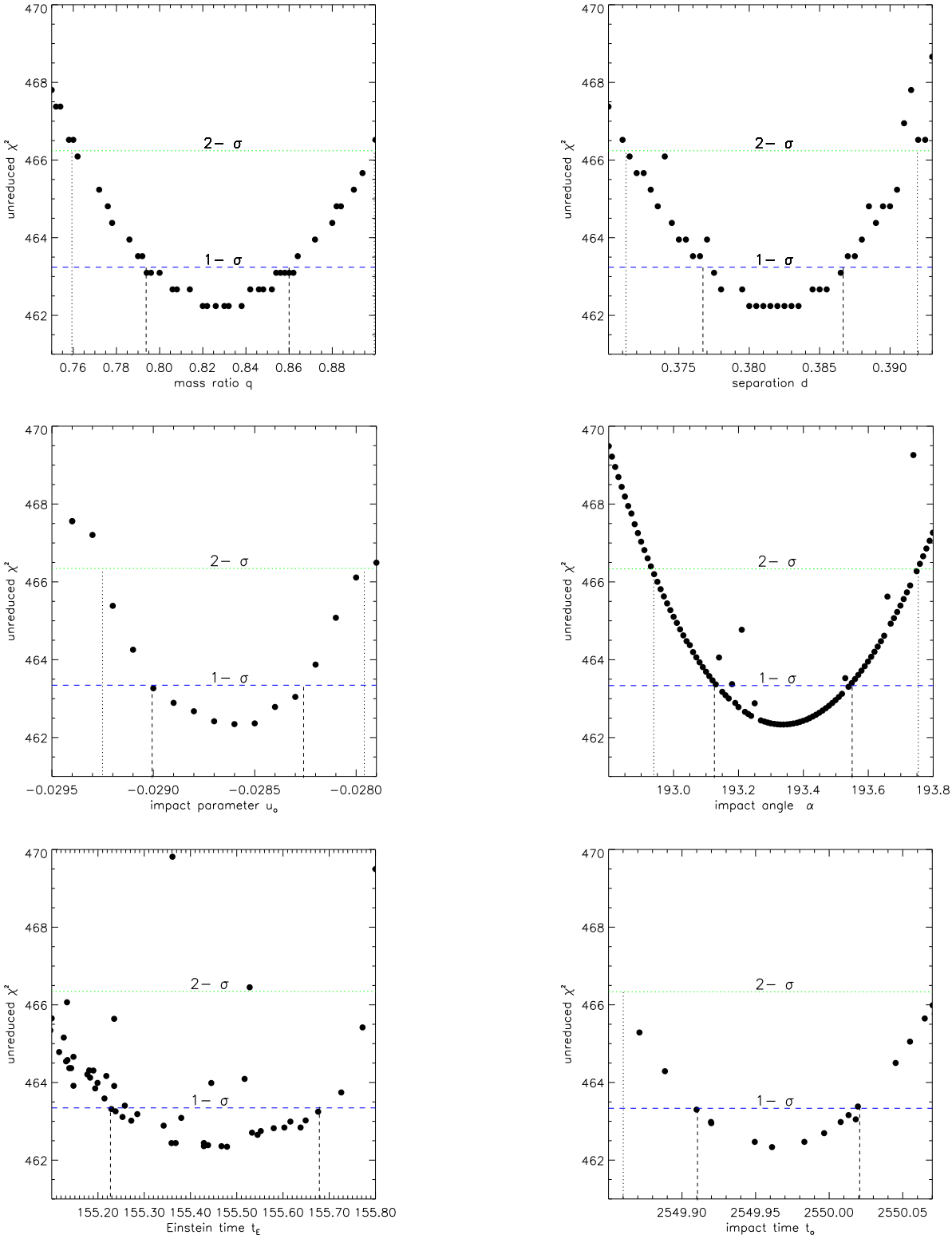


Figure 3.10: Confidence limits for fitted PSBL- parameters derived from marginalizations over the parameter of interest. Horizontal lines mark the $\Delta\chi^2$ levels corresponding to 1- and 2-$\sigma$ confidence.

### 3.2.3 GA setup

As mentioned in Sec. 3.1.4 genetic algorithms do not necessarily require a termination criterion. As seen from Fig. 3.3 the stochastic nature of their convergence behavior makes it difficult to even define one based on $\chi^2$-gradients[6]. The standard and robust way usually taken therefore is to prescribe a fixed number of generations, respectively iterations. For that purpose we perform a series of test runs of TANGO on our simulated event AE-1 to display the dependence of convergence from the two critical parameter population size $n_{\rm pop}$ and number of generations $n_{\rm gen}$. As quality criteria for convergence (as understood in this context here) we demand that the interesting parameters mass ratio $q$ and separation $d$ of the best individual/model lie within $\sim 15\%$ of 'true' parameters, which turns out to roughly correspond to demand that the reduced $\chi^2$/d.o.f $\lesssim 2$. This choice is inspired by the result of Vermaak (2003), where it was shown that for errors $\lesssim 15\%$ in the starting seed of local gradient optimizers their success rate of finding the 'true' minima starts to get significantly ($\sim 20\%$ for starting error $\sim 15\%$). Fig. 3.11 indicates that for the case where a priori very little is known on the lens parameters (apart for example that it is a non-planetary lens[7]) reasonable models are found for $n_{\rm pop} \gtrsim 250$ and $n_{\rm gen} \gtrsim 500$.

If one tightens the allowed range of parameters around a suggested good model space, effectively increasing the population density, the convergence success is significantly improved and setups with $n_{\rm pop} \gtrsim 50$ and $n_{\rm gen} \gtrsim 500$ can be recommended.

However it is important to keep in mind that the process of genetic optimization is highly nonlinear and there can of course be no guarantee for a specific setup to be the best for every lensing event. We therefore decided to pursue a strategy as given above, i.e to additionally conduct grid searches in the mass-ratio-separation plane to get an overview over possible solutions that can be explored in detail. This way the outcome of runs where all (point-source-binary-lens) parameters are allowed to vary can be put into a consistent context.

To give an impression on the speed of TANGO we state that a $n_{\rm pop} \times n_{\rm gen} = 200 \times 500$ run takes about one hour for a point-source-binary-lens model. Compared to gradient methods (with convergence times $\lesssim 1$ min for Amoeba) this is rather slow, but after all genetic algorithms are not built for accuracy and speed, but for the exploration of intricate parameter spaces. Details on how to use TANGO are given in Appendix A.

Figure 3.12 summarizes the modeling approach described in this Chapter in an illustrative way.

[6] In fact the absence of a termination criteria is one of the essential pillars of evolutions, which always has to proceed to search for the perfect individuum, especially when the environment is not absolute but subject to changes. There is always the chance that the discontinuous changes from one individuum to his offsprings miss a possibility to create a better adapted offspring.

[7] This can be concluded from comparisons between 'anomaly' duration with respect to total time scale of the event and the anomaly strength. (See also Sec. 2.1.2.)

| RUN | $q$ | $d$ | $u_o$ | $\phi$ [deg] | $t_{\rm E}$ [days] | $t_o$ [HJD$'$] |
|---|---|---|---|---|---|---|
| *large* | $[0.01, 1.0]$ | $[0.1, 2.0]$ | $[0.0, 1.0]$ | $[0.0, 360]$ | $[40, 400]$ | $[2540, 2560]$ |
| *tight* | $[0.6, 1.0]$ | $[0.3, 0.6]$ | $[0.0, 0.1]$ | $[180, 200]$ deg | $[140, 200]$ | $[2548, 2552]$ |

Table 3.3: The parameter bounds for two different scenarios. The **top row** reflects the situation when very little is known a priori on the lens event, apart from assuming that it is a non planetary binary lens. The **bottom row** reflects the case when an interesting region of parameter space has been identified and one tries to bracket it in. These bounds have been used in the genetic setup tests displayed in Fig. 3.11.

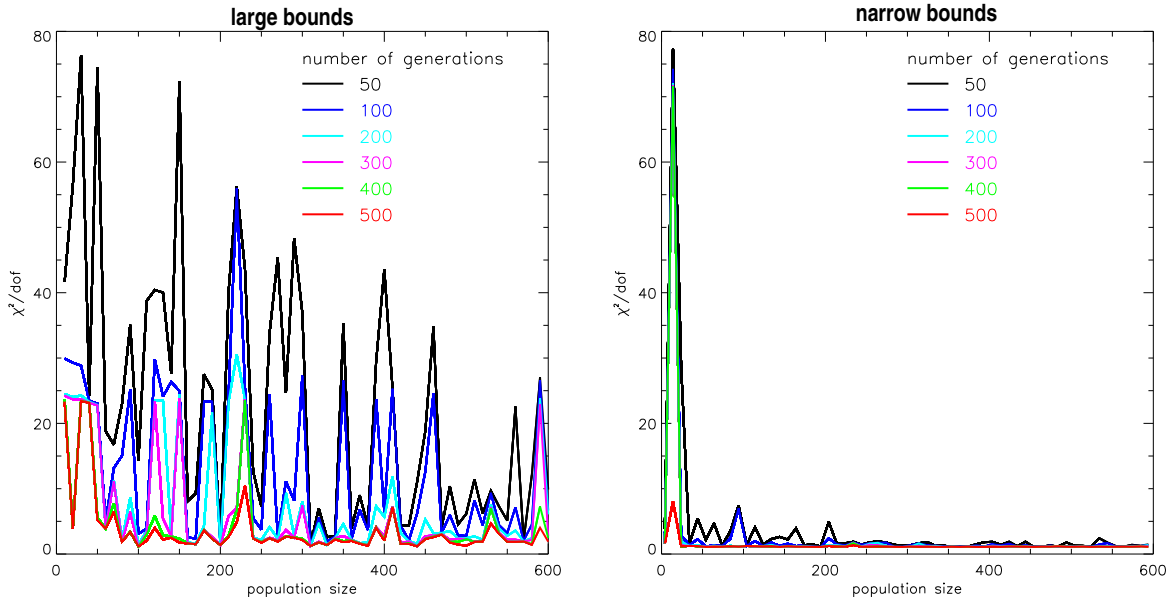


Figure 3.11: The convergence behavior of the genetic algorithm in the $6+2$ dimensional binary-lens-point-source model space on our test event as function of population size and number of generations (see described color code above). While on the **left** little knowledge on the lens model was assumed (apart from ruling out planetary models), i.e. rather large parameter bounds were allowed, the bounds on the **right** were tightened around a suggested minima (see Table 3.3 above for exact values of parameter bounds)

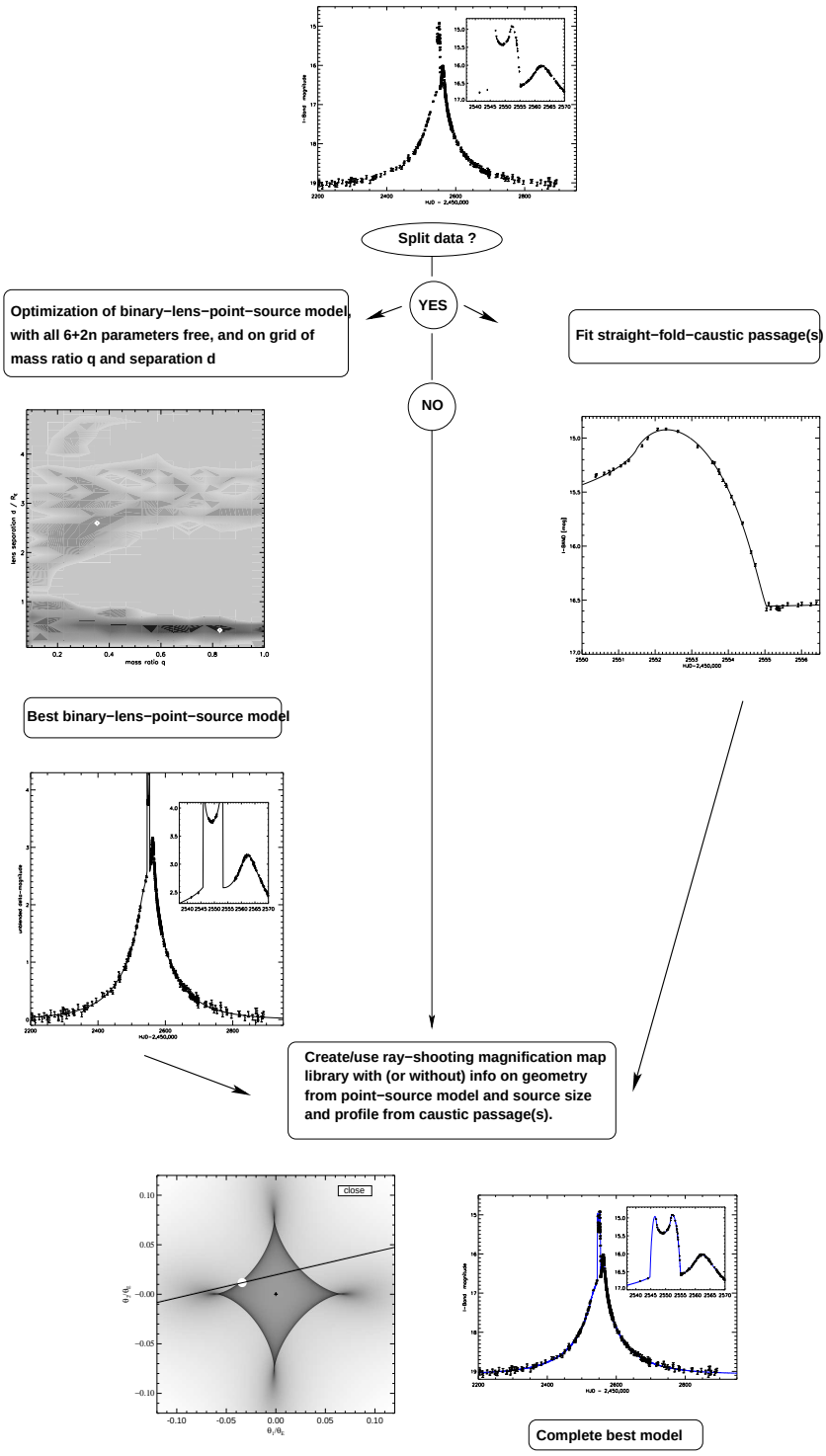


Figure 3.12: The 'big picture' of the scheme for modeling binary-lens events. If possible data exhibiting the passage of a straight fold caustic is separated from the rest, to infer the source profile. The best binary-lens-point-source model found, after conducting grid- and grid-free parameter searches, is then combined with the best source model via ray-shooting maps. If no data splitting can be made, a large library of amplification maps has to be created/used for the modeling process, being far more intensive with respect to disc space and CPU-time.

# Part II

# Analysis of PLANET campaign Microlensing Events

# Chapter 4

# The PLANET project

The **P** robing **L** ensing **A** nomalies **NET** work PLANET (Albrow et al. 1998), founded in 1995, is an international collaboration devoted to continuous and high precision follow-up observations of microlensing events alerted by survey teams such as OGLE (Udalski 2003) or MOA (Bond et al. 2004). Its telescopes are placed along different longitudes (see Fig.4 and corresponding Table) such that PLANET can observe its targets 24h a day during its operation in the prime galactic microlensing season from April to September, when the Bulge is best observable from the Southern Hemisphere.

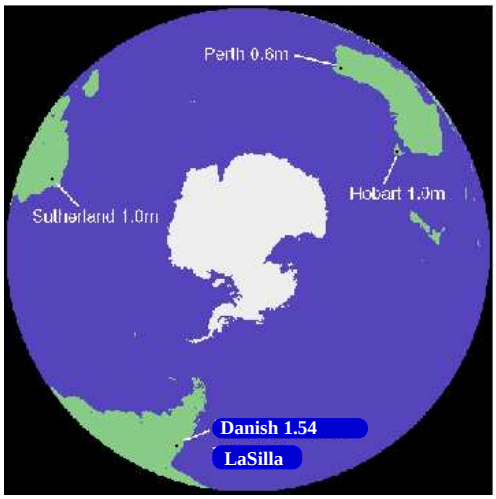


| Telescope | Location (longitude/ latitude) | CCD size (Pixel) |
|---|---|---|
| 1.0m Canopus (Hobart, Australia) | 147° 32' −43° | 512 × 512 0.47"/Pixel |
| 0.6m Bickley (Perth, Australia) | 116° 8' −32° | 576 × 384 0.58"/Pixel |
| 1.0m Elizabeth SAAO (Sutherland, Southafrica) | 20° 49' −32° | 512 × 512 0.35"/Pixel |
| 1.54m Danish (La Silla, Chile) | 289° 16' −29° | 8192 × 8192 0.238"/Pixel |

Figure 4.1: The telescopes of the PLANET group building its main backbone are located on the three continents Africa, Australia and South America to allow a round-the-clock monitoring of microlensing events in the Galactic Center during the observing seasons from April to September. Occasionally additional telescopes like the ESO 2p2 join the network, depending on the granted observing times of the particular season.

## 4.1 Data flow

The collected data is reduced online at each telescope using the PLANET pipeline QUYLLURWASI developed by Jean-Philippe Beaulieu, where the photometry is derived from point-spread-function (PSF) fitting with a modified version of Dophot (Schechter et al. 1993). At a later stage and depending on the data quality an additional rereducing with the ISIS package (Alard & Lupton 1998) is performed. Each site sents their data to a central server (currently located in Paris) which is managed by the scheduled *Homebase*, who coordinates the incoming data, visualizes the different data sets in a complete and consistent way using interactive web pages, decides the observing strategy and is responsible for issuing public anomaly alerts. Note that due to the different telescope/detector characteristics and observing conditions the data sets from each site have to be treated as independant from one another during the analysis[1].

Since 2001 the author is a member of PLANET and has besides his work on data analysis and modeling also conducted several observation runs[2] and homebase shifts[3].

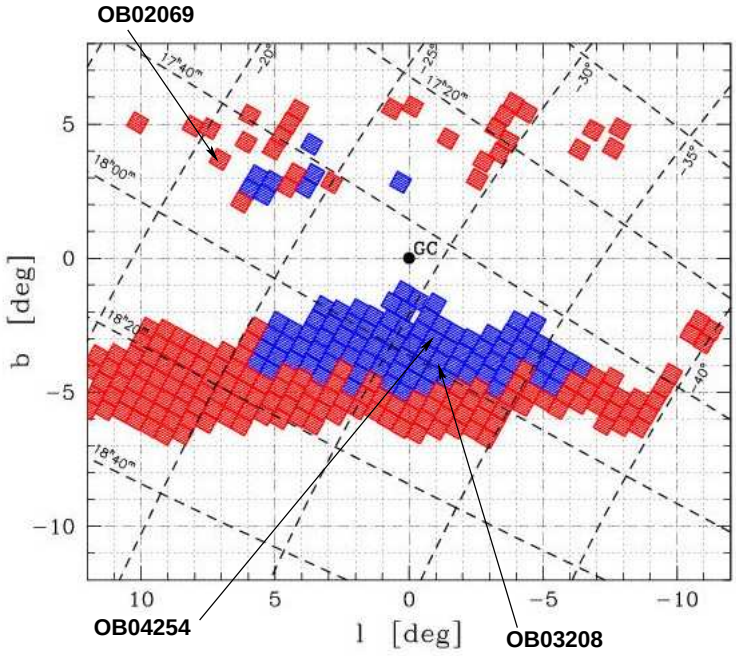


Figure 4.2: The positions on the sky in galactic and equatorial coordinates of the in this work studied microlensing events OGLE-2002-BLG-069, OGLE-2003-BLG-208 & OGLE-2004-BLG-254 . The filled black circle marks the Galactic center and the filled squares the fields observed by OGLE, where blue marks the fields of OGLE I and red marks the fields added up to the current OGLE III phase (adapted from OGLE webpage and modified)

[1]For example different pixel resolution and/or seeing conditions will lead to different blend fractions.
[2]At Canopus 19.5-9.6. 2001, ESO 2p2 21.7-6.8. 2002 and Danish 1.7-18.7 2004
[3]1.7.-21.7 2002, 1.6-17.6 & 12.7-20.7 2003 and 9.8.-25.8 2004.

# Chapter 5

# OGLE-2002-BLG-069

Never ask a woman what age she is.

*Murilo's father, Lesson 3*

## Abstract

We analyze the photometric data obtained by PLANET and OGLE on the caustic-crossing binary-lens microlensing event OGLE-2002-BLG-069. Thanks to the excellent photometric and spectroscopic coverage of the event, we are able to constrain the lens model up to the known ambiguity between close and wide binary lenses. The detection of annual parallax in combination with measurements of extended-source effects allows us to determine the mass, distance and velocity of the lens components for the competing models. While the model involving a close binary lens leads to a Bulge-Disc lens scenario with a lens mass of $M = (0.51 \pm 0.15)\ M_{\odot}$ and distance of $D_{\rm L} = (2.9 \pm 0.4)$ kpc, the wide binary lens solution requires a rather implausible binary black-hole lens ($M \gtrsim 126\ M_{\odot}$). Furthermore we compare current state-of-the-art numerical and empirical models for the surface brightness profile of the source, a G5III Bulge giant. We find that a linear limb-darkening model for the atmosphere of the source star is consistent with the data whereas a PHOENIX atmosphere model assuming LTE and with no free parameter does not match our observations.

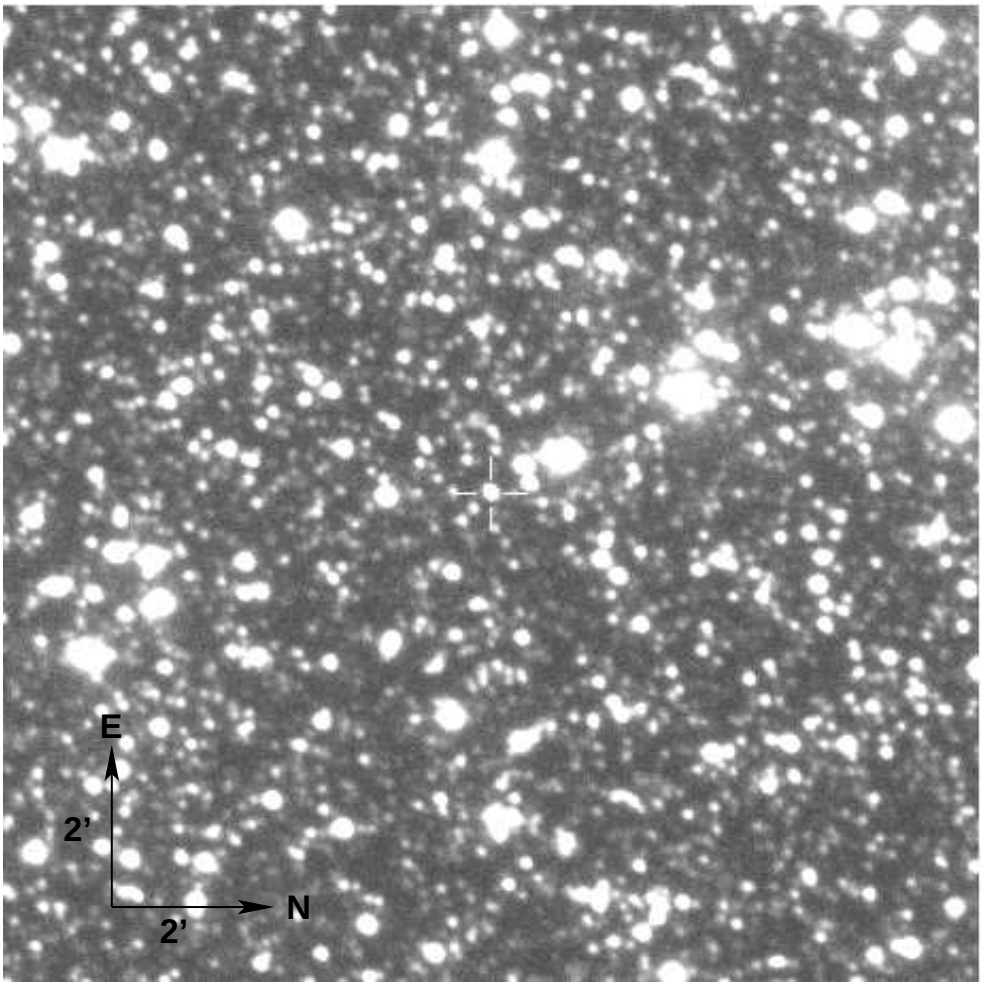


Figure 5.1: Finding chart of OGLE-2002-BLG-069 event. North is right and East is up on this $2' \times 2'$ sized frame. The position of the lensed source is at the center of the cross. It is a clear and bright ($I_{\rm OGLE} \sim 16.1$ mag) target leading to a rather smooth data reduction process. (credit: OGLE's page www.astrouw.edu.pl/∼ogle/ogle3/ews/ews.html)

## 5.1 Introduction

In recent years there has been a remarkable increase in the power of microlensing survey alert systems like OGLE-III (Udalski 2003)[1] and MOA (Bond et al. 2001)[2]. As a consequence, binary-lens microlensing events have become a unique and valuable tool to study, in unprecedented detail, members of the source and lens population within our Galaxy and in the Magellanic Clouds (Abe et al. 2003; Fields et al. 2003; An et al. 2002; Albrow et al. 2001b, 2000a,b, 1999b,a). The OGLE-2002-BLG-069 event is an ideal example for showing the current capabilities of microlensing follow-up observations.
The passage of a source star over a line-shaped (fold) caustic as created by a binary lens produces a characteristic peak in the light curve which depends on the stellar brightness profile. The data obtained for OGLE-2002-BLG-069 clearly reveal a pair of such passages consisting of an entry and subsequent caustic exit, where the number of images increases by two while the source is inside the caustic.
This binary-lens event is the first where both photometric and high-resolution spectroscopic data were taken over the whole course of the caustic exit. The previous attempts on EROS-2000-BLG-5 (Afonso et al. 2001) had good coverage but low spectral resolution (Albrow et al. 2001a), or a pair of spectra taken with high resolution but low signal-to-noise (Castro et al. 2001). Prior to this study, we presented a fold-caustic model of the OGLE-2002-BLG-069 photometric data comparing a linear law and a model derived from PHOENIX v2.6 synthetic spectra for the limb-darkening and analyzed variations in the $H\alpha$ line as observed in high-resolution UVES spectra taken over the course of the caustic passage (Cassan et al. 2004). A full account of the spectral observations in $H\alpha$, $H\beta$, $CaII$, $Mg$ and other lines will be given in Beaulieu et al. (2005). Here, we concentrate on the photometric data alone in order to present the full binary-lens model.
For the majority of observed microlens events all information about lens mass, relative lens-source distance and proper motion is convolved into one single characteristic time scale. Binary-lens events however are especially sensitive to effects caused by finite source size and parallax, so that in combination with the determination of the angular source radius, these three lens quantities can be measured individually (Refsdal 1966; Gould 1992). This is only the second binary microlensing event, after EROS-BLG-2000-5 (An et al. 2002), for which this has been achieved. Despite our high sampling rate and the small uncertainty of our photometric measurements, we still encounter the well known close/wide-binary ambiguity originating in the lens equation itself (Dominik 1999b) and which may only be broken with additional astrometric measurements as proposed in Dominik (2001) and Gould & Han (2000).

[1] www.astrouw.edu.pl/∼ogle/
[2] www.physics.auckland.ac.nz/moa/

## 5.2 OGLE-2002-BLG-069 photometry data

Alerted by the OGLE collaboration (Udalski 2003) on June 1 2002 about the ongoing Bulge microlensing OGLE 2002-BLG-069 event (R.A.=$17^h48^m1^s.0$ , decl.= $-21°16'9''.3$), the PLANET collaboration network began photometric observations on June 18, using 6 different telescopes, namely SAAO 1m (South Africa), Danish 1.54m (La Silla), ESO 2.2m (La Silla), Canopus 1m (Tasmania), Stromlo 50" (Australia) and Perth 0.6m (Australia). Data were taking in $I$- (UTas, Danish, SAAO, Perth), $R$- (La Silla) and $V$-bands (Stromlo). Since the $V$-band data set of Stromlo contains only 8 points, which is less than the number of parameters we fit, we do not use it in the modeling process.
The photometry reductions were done by point-spread-function (PSF) fitting using our own modified version of DoPHOT (Schechter et al. 1993), implemented as part of the PLANET reduction pipeline. The full raw data set including the public OGLE data (available from www.astrouw.edu.pl/∼ogle/ogle3/ews/ews.html) consists of 675 points. Data that were obviously wrong according to the observational log books or for which the reduction software did not succeed in producing a proper photometric measurement have been eliminated. Moreover, PLANET data taken under reported seeing that was significantly above the typical value for the given site were removed according to the cut-offs listed in Table 5.1. Altogether about 2 % of the data were rejected, leaving us with a total of 651 points (Fig.5.2).

| telescope | median seeing (arcsec) | seeing cut (arcsec) | number of points |
|---|---|---|---|
| ESO 2.2m | 1.13 | $\leq 2.5$ | 150 |
| Danish | 1.62 | $\leq 2.5$ | 108 |
| UTas | 3.13 | $\leq 3.6$ | 58 |
| SAAO | 1.93 | $\leq 2.6$ | 153 |
| Perth | 2.43 | $\leq 2.8$ | 86 |

Table 5.1: Selection criteria for PLANET photometric dataset.

Thanks to the favourable brightness at baseline ($I_{\rm OGLE} = 16.15 \pm 0.01$ mag) and low crowding of this event, the correlation between seeing and observed flux is negligible and does not yield a significant signature in the data, contrary to some previously analyzed events (e.g. Albrow et al. 2000b).

## 5.3 Binary-lens model

### 5.3.1 Parametrization and general approach

We recall that for a caustic crossing binary-lens event a minimum of $7 + 2n$ parameters are required, namely $t_0, u_0, t_{\rm E}, q, d, \alpha$, and $\rho_*$, plus $F_{\rm S}$ and $F_{\rm B}$ for each of the $n$ different

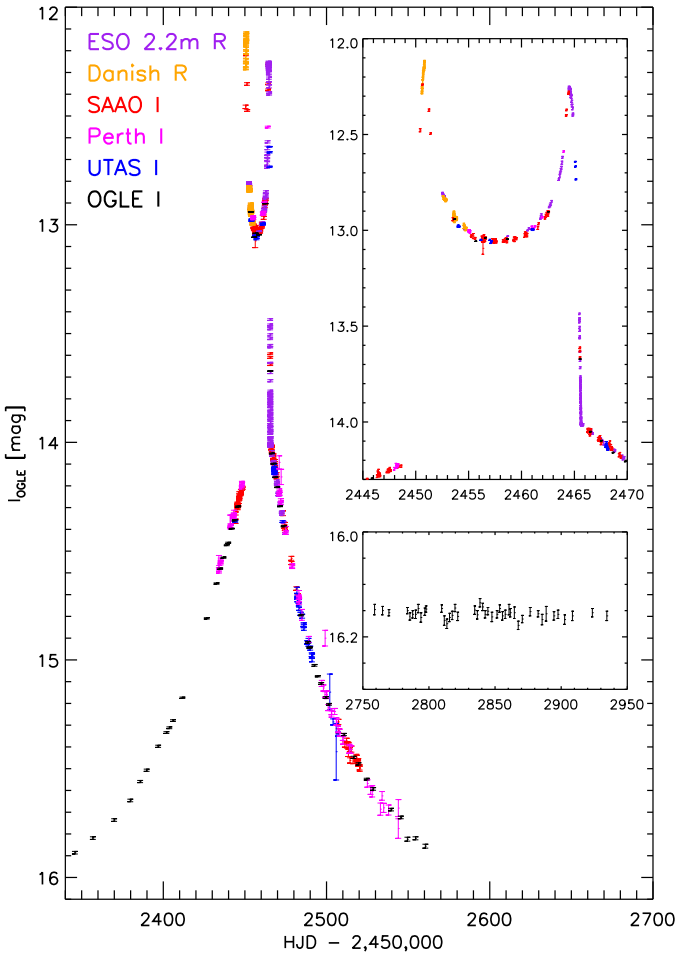


Figure 5.2: Complete photometric I- and R-band datasets of PLANET and OGLE, with PLANET calibrated to the OGLE filter. The **upper inner panel** shows a zoom of the caustic passages, while the **lower panel** displays the baseline measurements of OGLE made in the 2003 season, i.e. one year after the lensing event occurred.

observing sites (here $n = 6$). Here $t_0$ denotes the time of closest approach to the center of mass of the binary, $u_0 \geq 0$ the impact parameter at time $t_0$, $t_E$ is the time needed to cross the angular Einstein radius, which is defined as

$$\theta_{\mathrm{E}} = \sqrt{\frac{4GM}{c^2}\frac{D_{\mathrm{LS}}}{D_{\mathrm{L}}D_{\mathrm{S}}}}\,, \tag{5.1}$$

where $D_{\mathrm{L}}, D_{\mathrm{S}}$ and $D_{\mathrm{LS}}$ are the observer-lens, observer-source, lens-source distances and $M$ the total mass of the binary lens. The lens is characterized by the mass ratio $q = m_2/m_1$ between the secondary and the primary and their angular separation $d\,\theta_{\mathrm{E}}$. The impact angle $\alpha$ is measured between the line from the secondary to the primary and the positive direction

of source motion relative to the lens. The angular source size is given by $\rho_\star\,\theta_{\rm E}$. The flux of the unlensed source star is $F_{\rm S}$ and $F_{\rm B}$ is the flux contribution of any other unlensed sources (including the lens) within the aperture. For every observing site, $F_{\rm B}$ and $F_{\rm S}$ are determined independently to account for different background and flux characteristics of the individual telescopes/detectors. Modeling the parallax effect due to the orbital motion of the Earth requires 2 more parameters, the length $\pi_{\rm E}$ of the semi-major axis projected onto the sky plane and a rotation angle $\psi$, describing the relative orientation of the transverse motion of the source track to the ecliptic plane. The source surface brightness profile in this study is described by either a 1- or 2-parameter law so that the complete photometric model consists of up to 23 parameters.
Our initial search for the lens model involves only data outside the caustic-crossing region, where extended-source effects are negligible. Moreover, we also neglect parallax effects. We then scan the parameter space on a grid of fixed values of mass ratio $q$ and lens separation $d$, optimizing the remaining parameters $t_0, u_0, t_{\rm E}$ and $\alpha$ with the genetic algorithm Pikaia (Charbonneau 1995; Kubas et al. 2005a) and subsequently with a gradient routine to obtain $\chi^2$-maps such as shown in Fig. 5.3, which give an overview of possible model solutions. The values of $F_{\rm S}$ and $F_{\rm B}$ are simultaneously computed by inexpensive linear fitting. To explore in more detail the minima that are found we conduct a search with Pikaia over a restricted range of $q$ and $d$ but this time allowing these parameters to be optimized as well and again use gradient based techniques for final refinement. The results from the fold-caustic-crossing modeling in combination with the point source fits are then used to generate magnification maps with the ray-shooting technique (Wambsganss 1997). These maps contain the full information on the lens-source system.
We note that in crowded fields the raw photometry errors given by the reduction process clearly underestimate the true errors (Wozniak 2000a). To achieve a reduced $\chi^2$ of unity in our best fit model the photometric error bars would have to be rescaled by factors of 1.51 (SAAO), 1.92 (UTas), 1.34 (Danish), 1.16 (ESO 2.2m), 1.59 (Perth) and 2.3 (OGLE).

### 5.3.2 Preferred lens parameters

To exclude the data points which are affected by finite source effects we apply the argument given in Albrow et al. (1999a). There it was shown, that for times $\gtrsim 3\Delta t$ away from the fold caustic, where $\Delta t$ is the time in which the source radius crosses the caustic, the point source approximation is accurate enough for photometric errors of $\lesssim 1\%$. Based on the measured caustic crossing times (see section 5.4) we cut out data between 2450.0 $\leq$ HJD' $\leq$ 2452.8 and 2463.0 $\leq$ HJD' $\leq$ 2466.0, where HJD' = HJD $-$ 2450000. We then search for promising regions in parameter space on a grid of mass ratio $q$ and lens separation $d$, the two parameters that characterize the binary lens, with $q = 0.01, 0.05, 0.10, 0.15, ..., 1.00$ and $d = 0.01, 0.05, 0.10, 0.15, ..., 4.70$. The result is shown in Fig. 5.3. While the apparent close binary solution around $q \sim 0.6$ and $d \sim 0.5$ seems to be well defined, the numerical routines converge poorly in the vicinity of the wide-binary solution, reflecting the intricacy of binary-lens parameter space. By bracketing apparently interesting subsets of the $(q, d)$ plane, our algorithm identifies the best wide solution at $q \sim 0.16$ and $d \sim 3.7$.

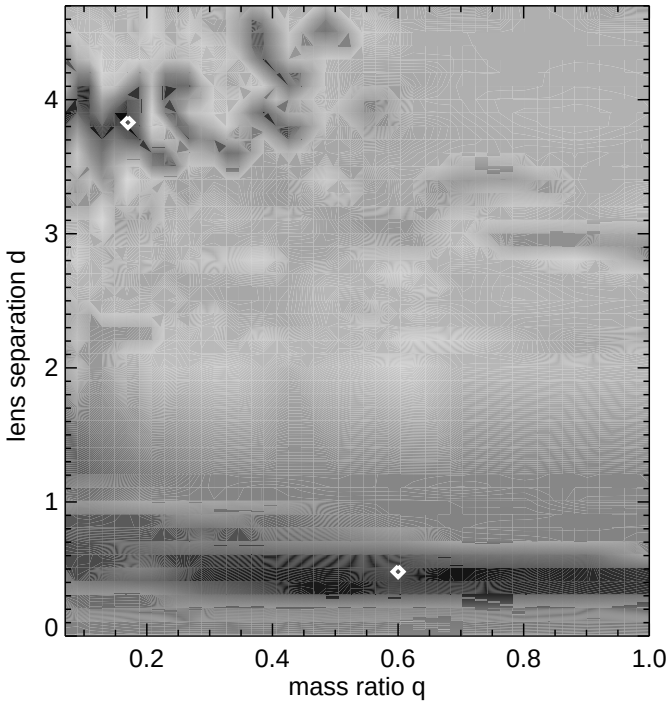


Figure 5.3: Gray-scale $\chi^2$ map of full grid in mass ratio q and lens separation d, with darker regions representing lower values of $\chi^2$. The irregularity of parameter space is reflected by the patchy appearance of the map, especially around the wide binary model in the upper left part of the plot. The best models are marked by the white diamonds at $q \sim 0.6$, $d \sim 0.5$ (close binary) and at $q \sim 0.16$, $d \sim 3.7$ (wide binary).

### 5.3.3 Annual parallax

Close-binary-lens models that neglect the motion of the Earth around the Sun show a significant asymmetry in the residuals which disappears if parallax is taken into account. Adapting the convention in Dominik (1998b) and illustrated in Fig. 5.4 we introduce as a parameter the projected length $\pi_{\rm E}$ of the Earth's semi-major axis in the sky plane, which is defined as

$$\pi_{\rm E} = \pi_{\rm LS}/\theta_{\rm E} = \frac{1\ {\rm AU}}{\theta_{\rm E}} \left( \frac{1}{D_{\rm L}} - \frac{1}{D_{\rm S}} \right) , \tag{5.2}$$

where $\pi_{\rm LS}$ is the relative lens-source parallax. The second additional parameter is the angle $\psi$ describing the relative orientation of the source motion to the ecliptic. The heliocentric ecliptic coordinates $(\varphi, \chi)$ used for the parallax modeling are derived from the standard geocentric ecliptic coordinates $(\lambda, \beta)$ by applying $\chi = \beta$ and $\varphi = \lambda + \pi + \varphi_\gamma$, where $\varphi_\gamma$ is the angle of the vernal equinox measured from the perihelion.
In 2002 Earth reached the perihelion at $\sim$ 2277.1 HJD' and the time of the vernal equinox was $\sim$ 2354.3 HJD'. This yields $\varphi = 163.3^\circ$ and $\chi = 2.1^\circ$ for OGLE-BLG-2002-069.

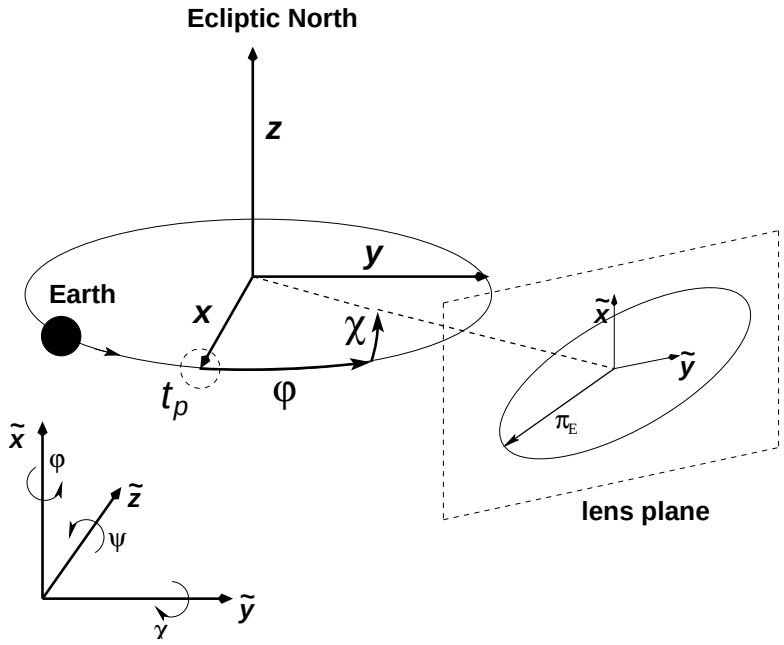


Figure 5.4: The coordinates $(\tilde{x}, \tilde{y})$ are chosen so that the right hand system $(\tilde{x}, \tilde{y}, \tilde{z})$ fulfils $\tilde{x} = z,\ \tilde{y} = y,\ \tilde{z} = -x$ for $\varphi = \chi = \psi = 0$. The longitude $\varphi$ is measured from the perihelion $t_p$ towards the Earth's motion and the latitude $\chi$ from the ecliptic plane towards Ecliptic North.

## 5.4 Source model

The data taken when the source transits the caustic show the corresponding characteristic shape. The caustic entry is not well sampled, because in the early stage of the event it was difficult to distinguish between a binary and a single lens, and the practically unpredictable rise of the light curve was rather short. On the other hand, the caustic exit has very good coverage thanks to our predictive online modeling. Hence, we focus our study on the caustic exit. We estimate that the exit occurred for (2463.45 $\leq$ HJD' $\leq$ 2467) approximately. The corresponding subset of data comprises 95 points from ESO 2.2m, 21 points from SAAO and 17 points from UTas, giving a total of 133 points. We assume the source to move uniformly and neglect the curvature of the caustic as well as the variation of its strength on the scale of the source size. This approximation (which is justified in Sec. 5.5) allows us to increase computational efficiency significantly by using a fold-caustic-crossing model (e.g. Cassan et al. 2004). We recall (Sec. 2.2.2) that during a caustic crossing, the total magnification $A^{(s)}$ of the source is the sum of the magnifications of the two critical images and the three other images :

$$A^{(s)} = a_{\rm crit}\ G_{\rm f}\left(\frac{t_{\rm f} - t}{\Delta t}\ ;\ \xi^{(s)}\right) + a_{\rm other} + \omega(t - t_{\rm f}). \tag{5.3}$$

Here $\Delta t$ is the time needed for the radius of the source to cross the caustic, $t_{\rm f}$ is the date at which the limb exits the caustic and $G_{\rm f}$ is a characteristic function (Schneider & Wagoner 1987) depending on the surface brightness profile $\xi$. The blending parameters

and the baseline magnitudes for each site are derived from the point-source model on the non-caustic-crossing part of the light curve ; they are held fixed in the following.
Limb-darkening is frequently characterized by a sum of power-laws:

$$\frac{\xi(\mu)}{\xi_0} = 1 - \sum_i a_i(1-\mu^i), \tag{5.4}$$

where $\mu = \cos\vartheta$ is the cosine of the emergent angle of the light ray from the star, and $a_i$ ($i = 1/2, 1, 3/2, 2...$) are the so-called limb darkening coefficients (LDC). We investigate the two most popular realizations : the linear ($a_1 \neq 0$) and square root limb darkenings ($a_1 \neq 0$ and $a_{1/2} \neq 0$). Performing a $\chi^2$ minimization on our fold-caustic data provides us with the parameters listed in Table 5.2 that best describe our photometric data. The value of $\chi^2$/d.o.f. tells us about the relative goodness of the fits among the studied models. Claret (2000) also introduced a 4-parameter law which fits the limb-darkening curves derived from spherical atmosphere models. However, as pointed out by Dominik (2004a), for coefficients beyond the linear law, the differences in the light curve are much smaller than the differences in the profiles, and it is not possible to find a unique set of coefficients given our data set. Finally, we also consider a PHOENIX atmosphere model that resulted from a spectroscopic analysis of the source star by Cassan et al. (2004), where corresponding broad-band brightness profiles for R- and I-band were computed.
In the upper panel of Fig. 5.5, the best model (with square-root limb darkening) is plotted with the data. The fit residuals obtained with the linear, square-root and PHOENIX limb darkening are displayed in the lower panels. With free limb-darkening coefficients, even the linear law describes the data reasonably well, while the square-root law allows a better match. In contrast the parameter-free PHOENIX model computed assuming LTE fails. The residuals for the caustic-crossing region show systematic trends that are typical for an inappropriate limb-darkening profile, as discussed by Dominik (2004b). A new analysis taking into account NLTE effects will be done in a forthcoming paper.
In the following sections, we will use the square-root limb darkening to describe the source star.

## 5.5 A complete model

With the point-source model and the brightness profile of the source determined from the data in the caustic-crossing region, we can now derive a complete and consistent model of the lens, yielding its mass $M$, distance $D_{\rm L}$ and relative transverse velocity $v$. This is done by generating magnification maps with the ray-shooting method (Wambsganss 1997) for the best-fit values found for mass ratio $q$ and lens separation $d$ and then convolving these maps with the source profile modeled in section 5.4. The maps and the corresponding light curves derived from them, are shown in figures 5.6, 5.7, and 5.8.
These maps also serve as a check on the validity of the straight-fold-caustic approximation (see Sec. 5.4). We find that the effect of curvature of the caustic is negligible and does not

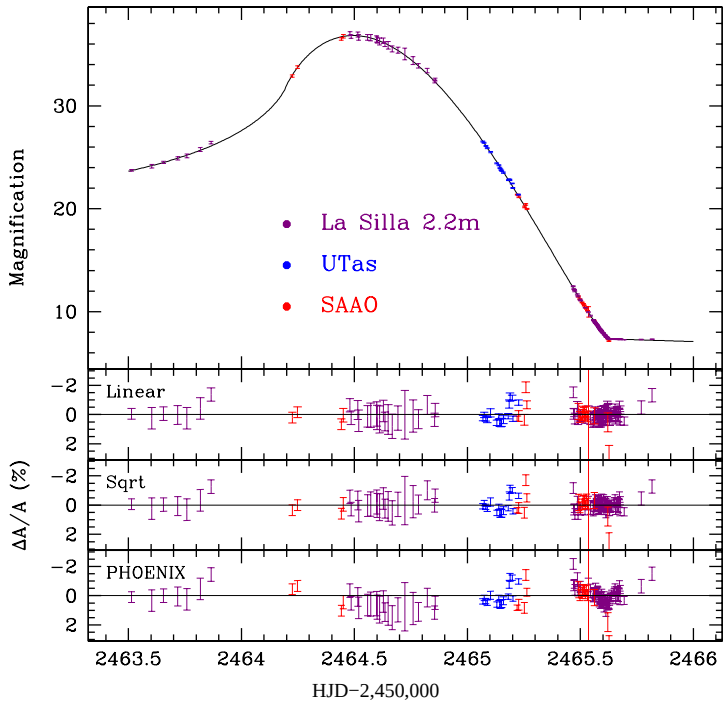


Figure 5.5: Data points and light curve obtained with square-root limb darkening (upper panel), and residuals coming from the linear, square-root and PHOENIX laws.

Table 5.2: Limb-darkening coefficients (LDC) derived from the fit of OGLE-2002-BLG-069 during the caustic exit. Each set of LDC corresponds to the best fit obtained (no error rescaling here) by using the LDC as well as the fold-caustic model parameters as free parameters.

| | Linear | Square root | PHOENIX |
|---|---|---|---|
| $t_{\rm f}$ (days) | 2465.624 | 2465.626 | 2465.636 |
| $\Delta t$ (days) | 0.71 | 0.72 | 0.72 |
| $\omega$ (days$^{-1}$) | $-0.10$ | $-0.10$ | $-0.11$ |
| $a_{\rm crit}$ | 19.98 | 20.03 | 19.85 |
| $a_{\rm other}$ | 7.33 | 7.35 | 7.33 |
| $a_1$ | 0.62 | 0.10 | - |
| $a_{1/2}$ | - | 0.80 | - |
| $\chi^2$/d.o.f. | 2.230 | 1.937 | 3.528 |

influence the results of the stellar surface brightness modeling. Table 5.3 lists all fit parameters for the best close- and wide-binary solution. The quoted 1-$\sigma$ error bars correspond to projections of the hypersurfaces defined by $\Delta\chi^2 = \chi^2 - \chi^2_{\rm min} = 1$ onto the parameter axes.

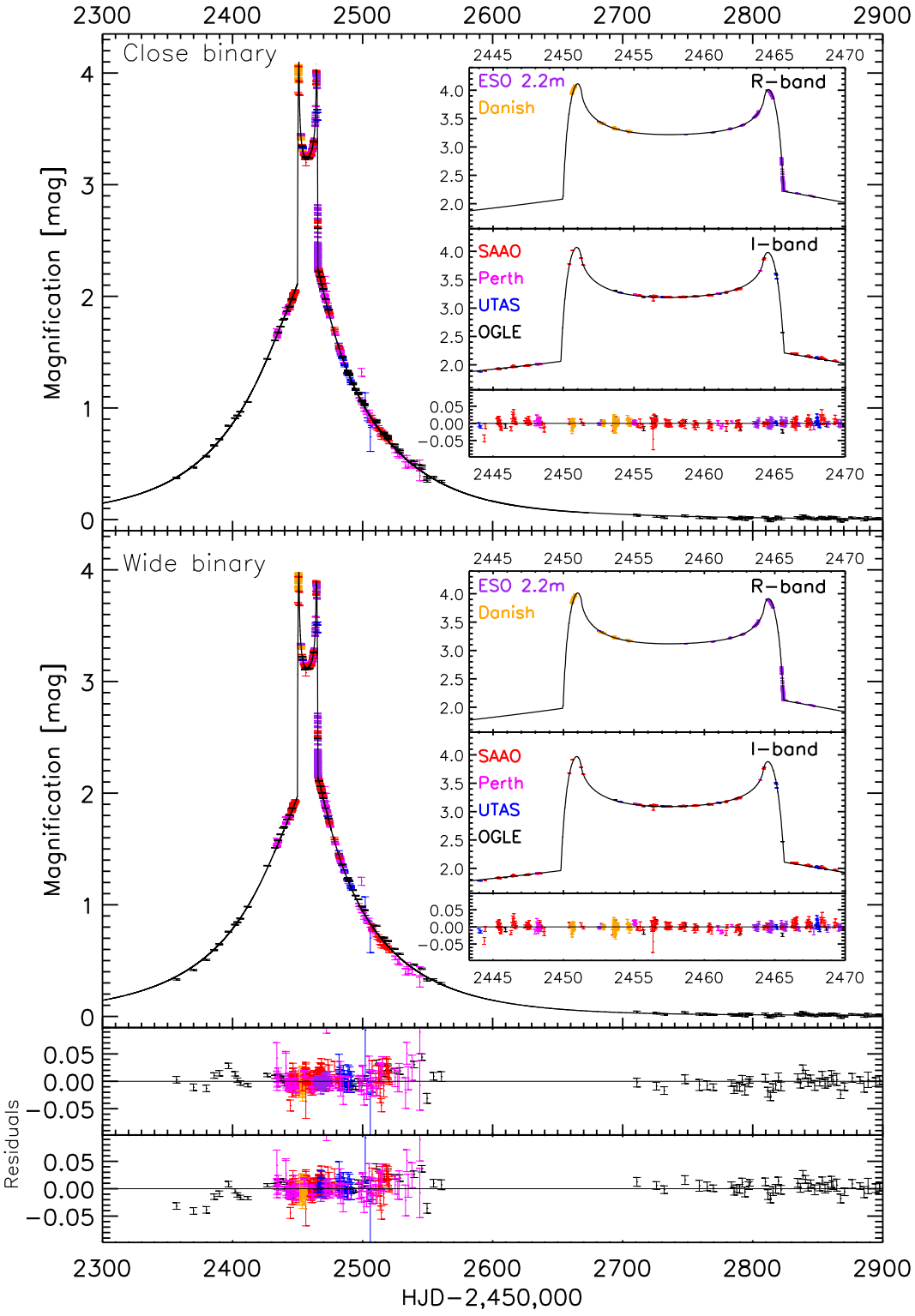


Figure 5.6: Lightcurves of close and wide binary-lens models and their residuals. Insets show a zoom of the caustic passages in the two different bands taken.

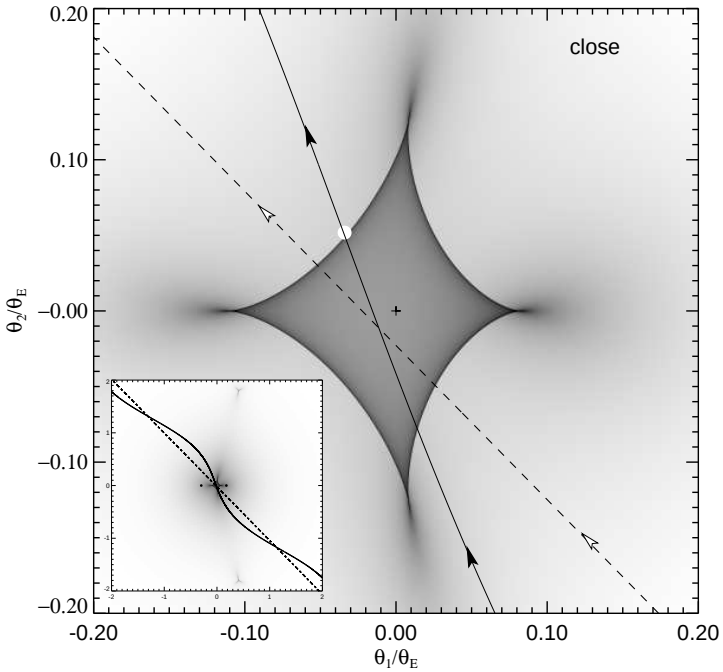


Figure 5.7: Magnification map and source trajectory for the close-binary model. The solid curve is the track of the source including annual parallactic motion and the dashed line represents the source motion (with direction indicated by the arrows) as seen from the Sun. The origin marked with the cross is the center of mass and the filled white circle indicates the source size. The grey-scale marks the magnification scale in the source plane, with dark regions corresponding to high magnification and bright regions referring to low magnification. The inset shows the full caustic topology, with the two filled black circles marking the positions of the binary lens components.

### 5.5.1 Physical lens properties

The measured finite source size and the parallax effect yield two independent constraints for determining the lens mass $M$, its distance $D_{\rm L}$ and transverse velocity $v$. Assuming a luminous lens we can put upper limits on its mass using our knowledge of the absolute luminosity and distance of the source star. These were determined in Cassan et al. (2004) from spectroscopic measurements combined with the measured amount of blended light (which includes any light from the lens) inferred from the light curve modeling.
Fig. 5.9 plots the implied blend fraction $h = F_{\rm B}/(F_{\rm S} + F_{\rm B})$ if both components of the lens are main-sequence stars (from A0 to M9, Allen 1972) put at distances of $2, 4, 6$, and 9 kpc along the line of sight to the lens in comparison with the blend fractions derived from OGLE data. If we assume the lens is the only source of the blended light, the inferred blend fraction from our best fit models gives an upper limit for the total lens mass of $\sim 2.5$ $\rm M_\odot$ for the close-binary and $\sim 0.8$ $\rm M_\odot$ for the wide-binary-lens model.

We use the source radius caustic crossing time $\Delta t$ from the straight-fold-caustic model,

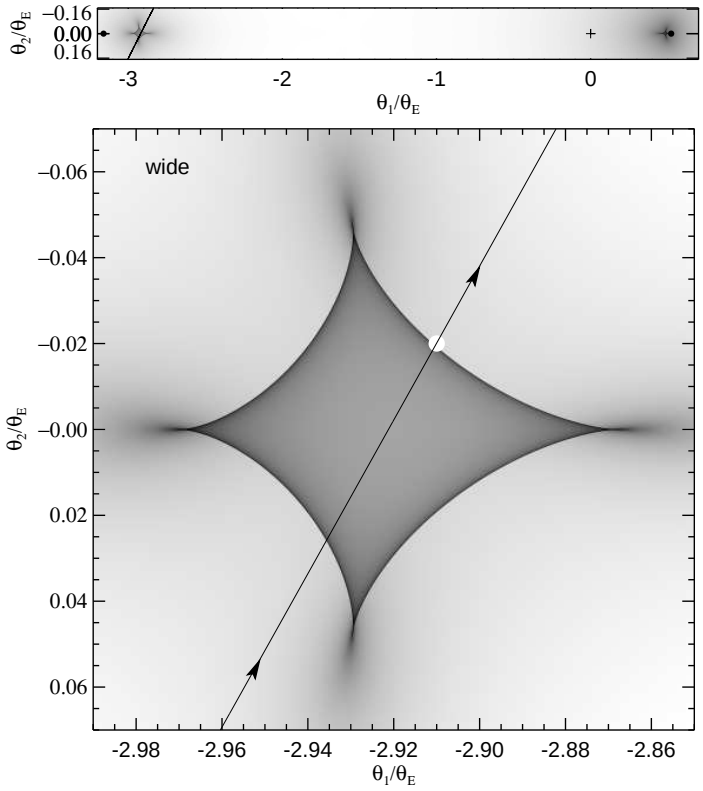


Figure 5.8: Magnification map and source trajectory for the wide-binary. The effect of parallax is negligible. The top panel shows the full caustic topology, where the lens positions are marked with the black filled circles and the center of mass by the cross. In the zoom around the secondary lens, **lower panel**, the filled white circle marks the source size, the arrows indicate the direction of source motion. As in Fig. 5.7 dark regions mark high magnification and bright regions represent low magnification areas.

together with the lens geometry given by $(q, d)$ and time-scale $t_{\rm E}$ from the point source model, to derive the relative angular source size $\rho_*$, which expressed as a fraction of the angular Einstein radius reads

$$\rho_* = \frac{\Delta t}{t_{\rm E}} \sin\phi \ , \tag{5.5}$$

with $\phi$ being the angle between source track and caustic tangent. The source size parameter $\rho_*$ is refined by fitting on a grid of magnification maps convolved with different source sizes. So with the inferred physical source size of $R_* \simeq 10\ R_\odot$ and source distance $D_{\rm S} = (9.4 \pm 1.4)$ kpc from the spectral measurements (Cassan et al. 2004) the constraint on the lens mass from extended-source effects can be inferred from

$$\frac{M(x)}{M_\odot} = \frac{c^2}{4GM_\odot D_{\rm S}} \frac{{R_*}^2}{{\rho_*}^2} \frac{x}{1-x} \ , \tag{5.6}$$

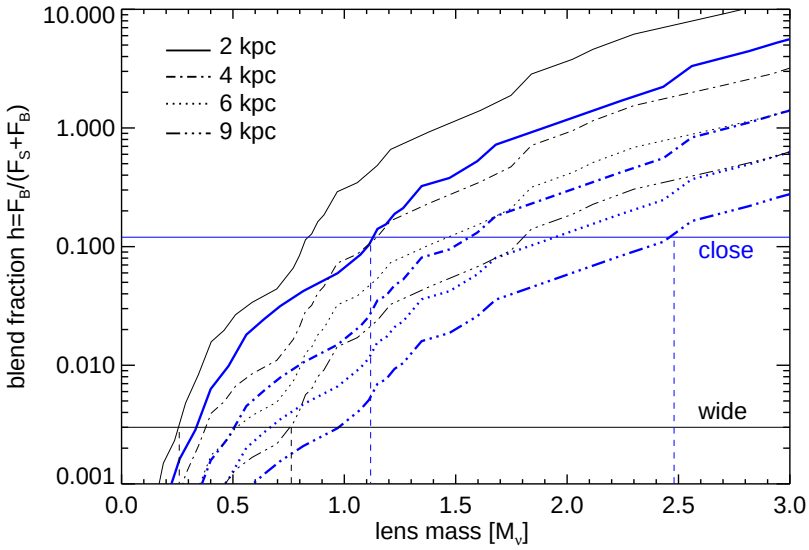


Figure 5.9: Assuming the lens to be composed of two main-sequence stars according to each of our models, the blend fraction $h = F_{\rm B}/(F_{\rm S} + F_{\rm B})$ for OGLE data (horizontal solid lines) yields upper limits (vertical dashed lines) on the total lens mass for the known brightness and distance of the source ($M_V = +0.9$, $(V - I) = 0.95$) and $D_{\rm S} = (9.4 \pm 1.4)$ kpc from Cassan et al. (2004). While the close-binary model is compatible with lens masses up to $\sim 1.1 - 2.5$ M$_\odot$, the wide-binary model only allows lens masses up to $\sim 0.3 - 0.8$ M$_\odot$ for lens distances between 2-9 kpc (where the thin lines represent the wide binary lens and the thick lines the close binary lens).

with $x = D_{\rm L}/D_{\rm S}$. The dependence of the lens mass upon annual parallax effects reads

$$\frac{M(x)}{M_\odot} = \frac{c^2}{4GM_\odot D_{\rm S}} \left(\frac{1\ {\rm AU}}{\pi_{\rm E}}\right)^2 \frac{1-x}{x} \quad . \tag{5.7}$$

The curves arising from these two relations are plotted in Fig. 5.9 for our best fit parameters $\pi_{\rm E}, \rho_*$ (see Table 5.3) of the wide and close binary-lens model. From this we obtain the following physical lens parameters,

$$M_{\rm close} = (0.51 \pm 0.15)\ M_\odot\ ,\ {\rm at}\ D_{\rm L} = (2.9 \pm 0.4)\ {\rm kpc} \tag{5.8}$$

and

$$M_{\rm wide} \gtrsim (126 \pm 22)\ M_\odot\ ,\ {\rm at}\ D_{\rm L} \gtrsim (9.0 \pm 2.3)\ {\rm kpc}\ . \tag{5.9}$$

The close-binary solution yields a Bulge-Disc lens scenario similar to that for EROS-BLG-2000-5 (An et al. 2002), namely an M-dwarf binary system with a projected separation of $(4.5 \pm 1.1)$ AU located most likely just beyond the Orion arm of the Milky Way. The marginal detection of parallax effects in the wide-binary model however allows us to put lower limits on the mass and velocity of the lens, suggesting a rather implausible binary system consisting of two super-stellar massive black holes in the Galactic bulge with $v_{\rm wide} \gtrsim$

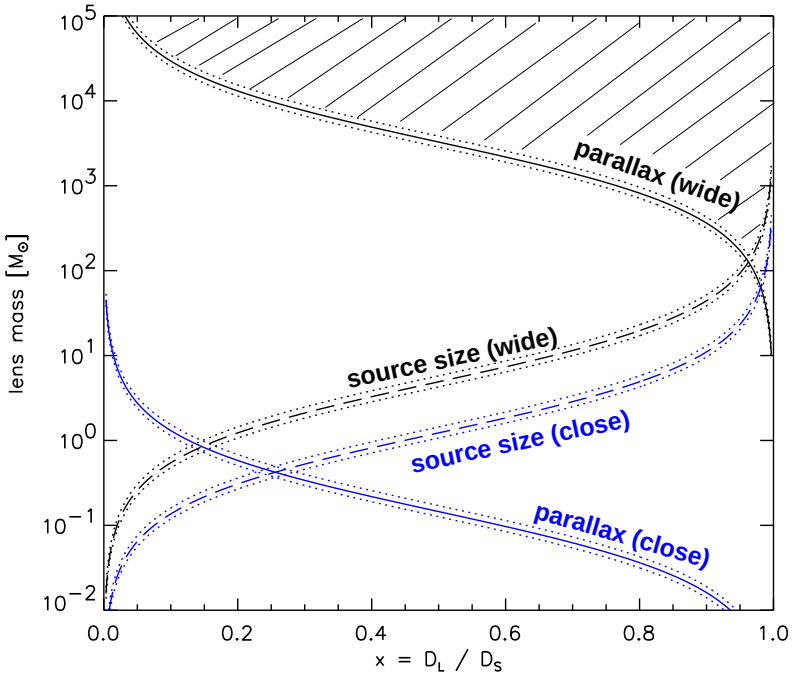


Figure 5.10: The independent constraints on the lens mass from the source size (dashed line) according to Eq. (5.6) and from parallax effects according to Eq. (5.7) (solid line) for the close and wide separation binary models as function of $x = D_{\rm L}/D_{\rm S}$. The dotted lines mark the uncertainty due to the error in the source distance measurement. While the close-binary constraints intersect at the plausible lens mass of $(0.51 \pm 0.15)$ $\mathrm{M}_\odot$ implying a disc lens at $D_{\rm L} = (2.9 \pm 0.4)$ kpc, the wide binary favours a rather implausible scenario of a binary black hole of $M \gtrsim (126 \pm 22)$ $M_\odot$ in the Bulge at $D_{\rm L} \gtrsim (9.0 \pm 2.3)$ kpc, with the hatched region marking the allowed parameter space for the wide-binary solution.

129 km s$^{-1}$. We therefore reject the wide binary model and derive for the transverse velocity of the close binary model

$$v_{\rm close} = \frac{R_*}{t_{\rm E}(\frac{\pi_{\rm E}}{1\ {\rm AU}}\ R_* + \rho_*)} = (49.8 \pm 2.7)\ {\rm km\ s^{-1}}\ . \qquad (5.10)$$

## 5.6 Summary and Conclusions

While the number of observed galactic microlensing events has now reached an impressive count of over 2000 (with about 5 % of them being identified as binary-lens events), still very little is known about the physical properties of the lens population, since in general the information on mass, distance and velocity of the lens needs to be inferred from one single parameter, the event time scale $t_{\rm E}$. The present work is the second successful attempt (after An et al. 2002) at putting strong constraints on lens and source properties in a microlensing event. This event involves a G5III cool giant in the Bulge at a distance of $D_{\rm S} = (9.4 \pm 1.4)$ kpc lensed by an M-dwarf binary system of total mass $M = (0.51 \pm$

| parameter | close | wide |
|---|---|---|
| $q$ | $0.58^{+0.05}_{-0.02}$ | $0.17^{+0.06}_{-0.02}$ |
| $d$ | $0.46^{+0.01}_{-0.02}$ | $3.68^{+0.02}_{-0.02}$ |
| $u_0$ | $0.016^{+0.001}_{-0.003}$ | $2.562^{+0.005}_{-0.002}$ |
| $\alpha$ [deg] | $134.4^{+0.5}_{-0.5}$ | $60.8^{+0.5}_{-0.5}$ |
| $t_{\rm E}$ [days] | $104.5^{+1.0}_{-1.0}$ | $286.5^{+3.0}_{-2.0}$ |
| $t_0$ | $2456.92^{+0.10}_{-0.10}$ | $2825.32^{+0.12}_{-0.12}$ |
| $\pi_{\rm E}$ | $0.23^{+0.02}_{-0.02}$ | $0.002^{+0.05}_{-0.02}$ |
| $\psi$ [deg] | $258.551^{+12.2}_{-12.2}$ | $189.0^{+10.5}_{-10.5}$ |
| $\rho_*$ | $0.0048^{+0.0005}_{-0.0005}$ | $0.0023^{+0.0009}_{-0.0009}$ |
| $h_{\rm OGLE}$ | $0.10^{+0.02}_{-0.02}$ | $0.00^{+0.03}_{-0.00}$ |
| $\chi^2$/d.o.f. | 2029.8 / 631 | 2251.0 / 631 |

Table 5.3: Fit parameters of best close and wide-binary models with $1\sigma$ uncertainties. The $\chi^2$ values are based on the raw photometric errors. i.e. without rescaling factors.

0.15) $M_\odot$ located at $D_{\rm L} = (2.9 \pm 0.4)$ kpc. These conclusions could only be achieved by the use of a network of telescopes to ensure a continuous, dense and precise coverage of the event, whereas data obtained from a survey with mainly daily sampling are insufficient for achieving this goal (Jaroszyński et al. 2004). The parameter space exploration, for both lens and source properties, described here provides a template for our future analysis of binary-lens events with fold-caustic crossings.

# Chapter 6

# OGLE-2003-BLG-208

The way I used to love you Baby, that's the way I hate you now.

*B.B. King*

## Abstract

Photometric observations performed by PLANET, OGLE and MicroFUN on the high amplification event ($A_{\max} \approx 30$) OGLE-2003-BLG-208 reveal a deviation from the single-lens behavior at the peak region lasting about 3.5 days. Although a rather dense sampling of the anomaly was achieved the modeling analysis led to a highly ambiguous lens parameter space. While the data set is consistent with a Jovian companion to the lens, a non-planetary binary lens model with mass ratio $q \approx 0.2$ is slightly preferred (by $\Delta\chi^2 = 187.4$). We note however that in principle the competing models could have been disentangled, if one of our network sites would not have been clouded out during a critical phase of the anomaly.

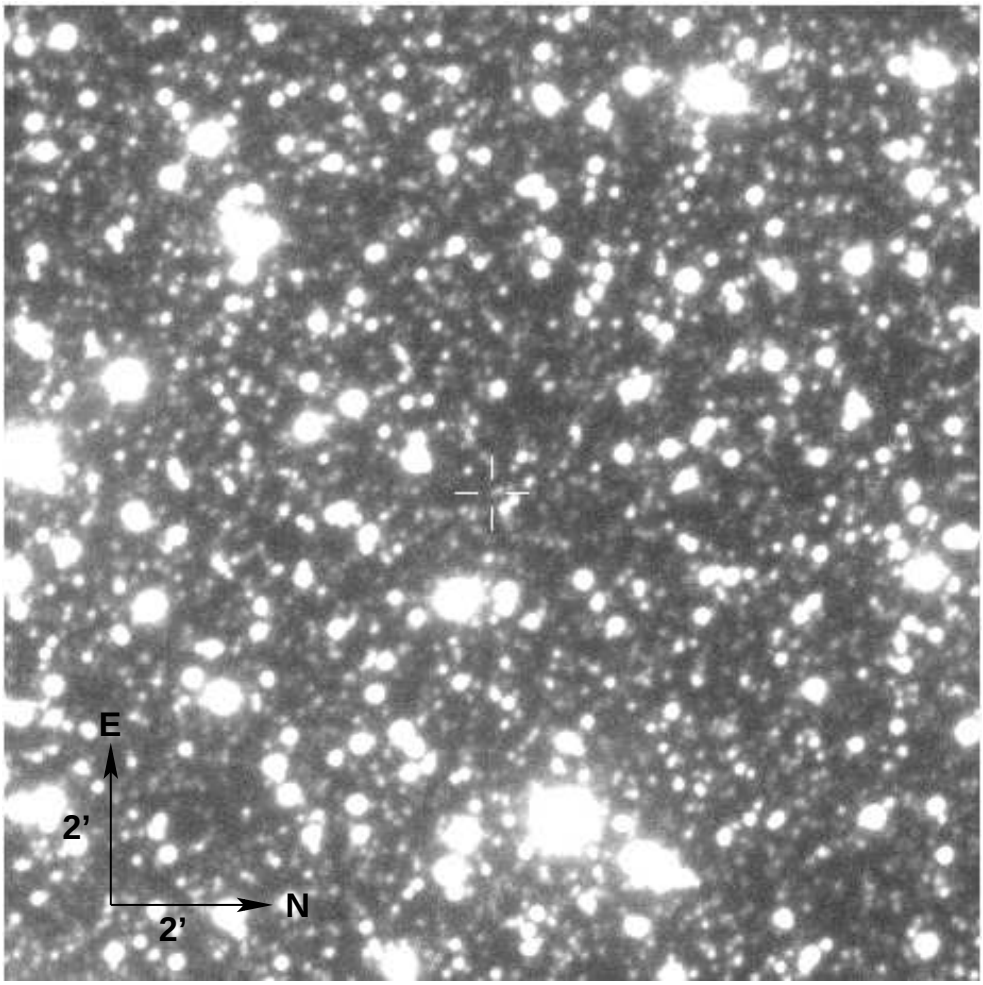


Figure 6.1: Finding chart of OGLE-2003-BLG-208 event. As before North is right and East is up on this $2' \times 2'$ sized frame and the position of the lensed source is at the center of the cross. This at baseline very faint event ($I_{\rm OGLE} \sim 19.4$ mag) has a brighter companion to the North-East causing additional trouble in the reduction process. (credit: OGLE's page www.astrouw.edu.pl/∼ogle/ogle3/ews/ews.html)

## 6.1 Introduction

The work of Griest & Safizadeh (1998), claiming that planets present in the lensing zone around the lens can be detected with a probability of almost 100% in *High Amplification Events* (HAE's with $A_{\max} \gtrsim 20$) had a huge impact on the observing strategy of microlensing campaigns such as PLANET. Their claim was based on the fact, that for sufficient small impact parameters (resulting in high maximal amplification, roughly speaking $A_{\max} \sim 1/u_o$) one can probe the central caustic of a binary lens system and any possible planetary companion would leave a detectable mark in the peak region of the lightcurve. HAE's then (although more rare[1]) became the prime hunting objects of microlensers. The extra bonus that possible deviations from the single-lens behavior would then occur at a predictable time, namely at the peak, and observational resources could be optimized in their efficiency, caused a kind of planetary gold rush atmosphere around the turn of the millennium.

In a long and painful process however, one had to realize that one had been vastly too optimistic. One simply had ignored or underestimated the fact that the central caustic is affected by any object not only planets and that star companions outside the lensing zone could mimic planetary signatures, leading to severe ambiguities in the models. For a phenomena which is not reproducible this was a strong set back and together with a series of false planetary alerts, scepticism inside and outside the lens community grew. The first and to this day the only un-disputable planet found with microlensing (OGLE 2003-BLG-235/MOA 2003-BLG-53 Bond et al. (2004)) was a big relief and brought back new life to the community.

Nevertheless one implication of Griest & Safizadeh (1998) remains fruitful, namely that the absence of lightcurve anomalies in HAE's puts strong constraints on the presence of possible planetary companions. So while a characterization of possible planets in HAE's is difficult they can be at least excluded with reasonable confidence. Of course it is more spectacular to find planets but putting constraints on their abundance is also a very worthwhile scientific undertaking (see Chap. 8). The event presented in this Section is an example for the situation where one already was close to open the champaign and celebrate the first lensing planet but then had to put it back into the fridge and drown the frustration in another toxic liquid. OGLE-2003-BLG-208 reached a maximum amplification[2] of $A_{\max} \sim 30$ and shows a clear deviation from a single-lens lightcurve at the peak. This anomaly, lasting about 3.5 days, looks as if the single lens peak has been cut off asymmetrically. Although planetary models are consistent with the data the binary lens models are slightly preferred with a $\Delta\chi^2 = 187.4$. However even if a re-reduced data set would favor statistically slightly the planet solution, claiming a planet detection here would leave too many doubts given the many ambiguities in the model space of this event.

[1]The distribution of impact parameters is uniform and therefore the fraction of high amplification events is only a few percent.

[2]Note that we state here the un-blended amplification, not the amplification above baseline. We further note that the given $A_{\max}$ is also model dependant and that the stated value corresponds to the best single lens model.

## 6.2 Photometry data

PLANET follow-up observations of the OGLE-2003-BLG-208 (R.A.=$17^h58^m20^s.0$ , decl.= $-33°31'50''.0$) event began on June 11, 2003. The data set in the $I$-Band consists of 120 points from SAAO (1m Elizabeth, Sutherland, South Africa), 27 points from UTas (1m Canopus, Hobart, Australia), 93 points from Perth (0.6m Bickley, Australia). and 170 points in $R$-Band from the Danish (1.54, LaSilla, Chile). Furthermore 48 points from OGLE and 29 points of MicroFUN (CTIO, Chile) both in $I$-Band were taken into account in the analysis. The high crowdiness (a brighter and very close companion to the North-East is visible in the finding chart Fig. 6.1) and faintness at baseline ($I_{\mathrm{OGLE}} \sim 19.4$ mag) of the target limits severely the photometric precision and causes a lot of scatter. Even an ISIS re-reduction does not solve all the problems, for example the Perth data unfortunately remain useless (and are omitted from the plots).

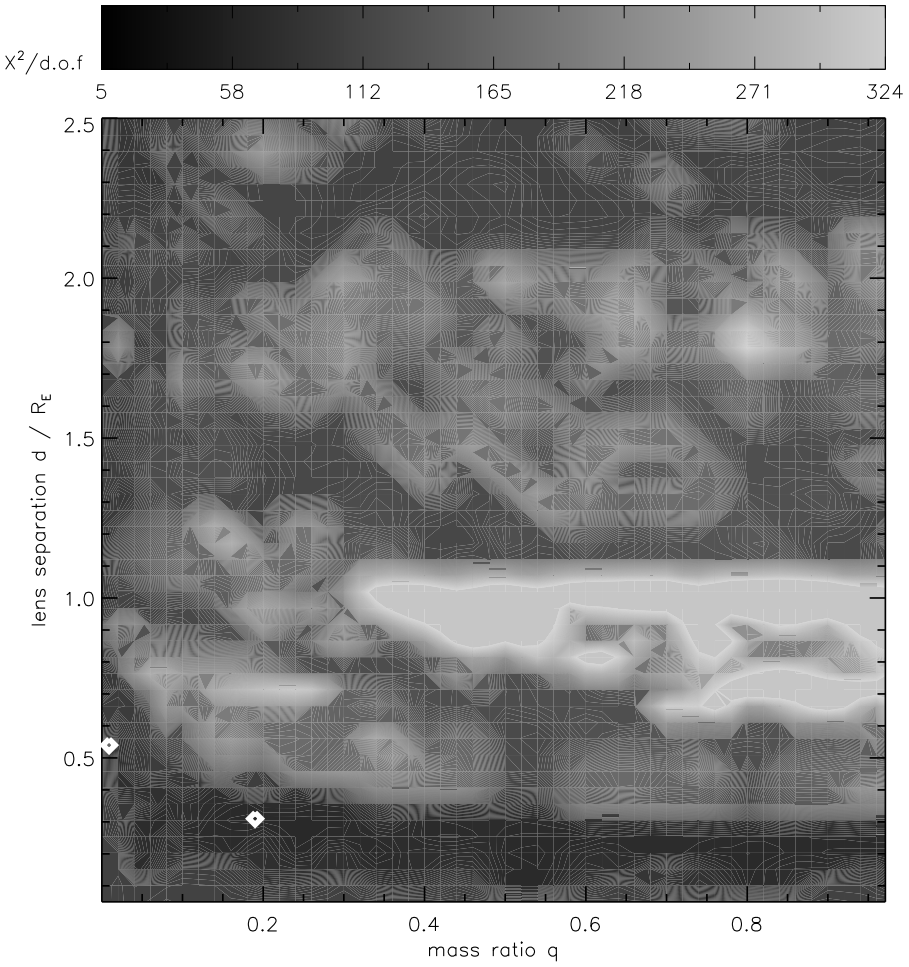


Figure 6.2: The $\chi^2$-landscape of OGLE-2003-BLG-208's mass-ratio-$q$-separation-$d$ parameter space is highly ambiguous. Parameter optimizations leaving all point-source-binary-lens parameters free, converge at $q = 0.009$ and $d = 0.54$ in the planetary regime and at $q = 0.19$ and $d = 0.31$ in the non planetary case (marked as white diamonds).

## 6.3 Preferred lens parameters

Using a point-source-binary-lens model the performed grid scan of the plane spanned by mass ratio $q$ and separation $d$ displayed in Fig.6.2 with $q \in [0.0001, 1.0]$, $\Delta q = 0.0005$, $d/R_{\rm E} \in [0.05,\ 2.6]$, $\Delta d = 0.1$ reveals a highly ambiguous lens parameter space. At first glance the safest conservative conclusion to be drawn is that lens configurations with separations $d \sim 1$ for $q \gtrsim 0.3$, i.e. one-caustic topologies (see Chapter 2), are excluded and that especially the region $d \lesssim 0.6$ looks interesting. After verifying that no competing models outside the grid up to $d \sim 10$ (corresponding to $30 - 70$ AU over the range of standard lens scenarios) exist, we restrict the mass ratio to $q \leq 0.01$ in order to look for the best planetary solution. Our optimizing routine TANGO (Sec. 3.2) converges at the model shown in Fig. 6.3 with $q = 0.009$ and $d = 0.54$ (see Table 6.1 for complete parameter set). While the model looks reasonable the fact that the found value for $q$ is close to the allowed boundary of 0.01 calls for attention. Freeing the mass ratio from this upper bound we arrive at the model displayed in Fig. 6.4 with $q = 0.19$ and $d = 0.31$ improving the fit by $\Delta\chi^2 \sim 187.4$. This model has a more pronounced curvature at peak and seems to reproduce the anomaly a bit better. The little bump at around HJD$' \sim 2905$ results from a secondary caustic approach. The significance of this feature given the current data quality in the wings is however questionable.

The corresponding caustic structures of both models are shown in the amplification maps of Fig. 6.5 and Fig. 6.6. An impression of the similarity and differences of the central caustics of the two competing models is given Fig. 6.7, where both caustics have been plotted together in the same scale.

The absence of sharp slope discontinuities in the residuals of both models, that extended source effects could have induced, seems to justify our point source approximation. This means that the inferred minimum impact parameter $u_o$ gives an upper limit on the source size $\rho_*$ measured in fractions of $\Theta_{\rm E}$, namely $\rho_* \lesssim 0.034$ from the planet model, respectively $\rho_* \lesssim 0.066$ from the non planetary model. This is consistent with already measured source sizes, which are in the range of $\sim 0.001$ to $\sim 0.04$ (An et al. 2002; Kubas et al. 2005b).

The effect of annual parallax is marginally detected in both models with $\Delta\chi^2 \sim 30$. Unlike the case of OGLE-BLG-02-069 (Kubas et al. 2005b) however, both models are consistent with rather typical lens scenarios as displayed in Fig. 6.8, with the non-planetary model favoring the lens to be closer to us than the planetary model. Unfortunately the lack of appropriate multi-band/spectroscopic measurements needed to unravel the nature and location of the source star, prevents us to put more tight physical constraints on this event.

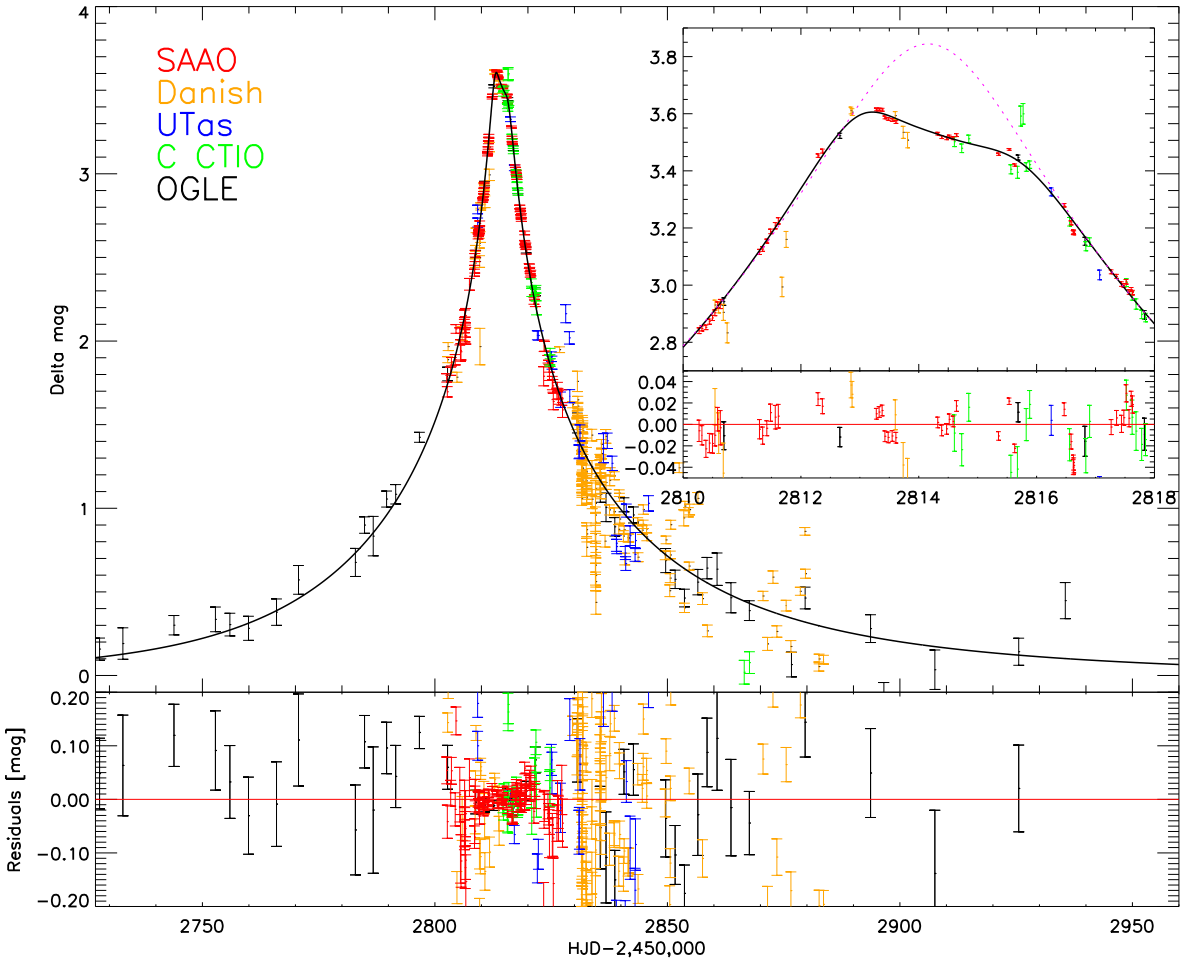


Figure 6.3: The best planetary model found for OB-2003-BLG-208 has the mass ratio $q = 0.009$ and the separation $d = 0.54$. The dotted line in the Zoom panel shows the best single lens model for comparison.

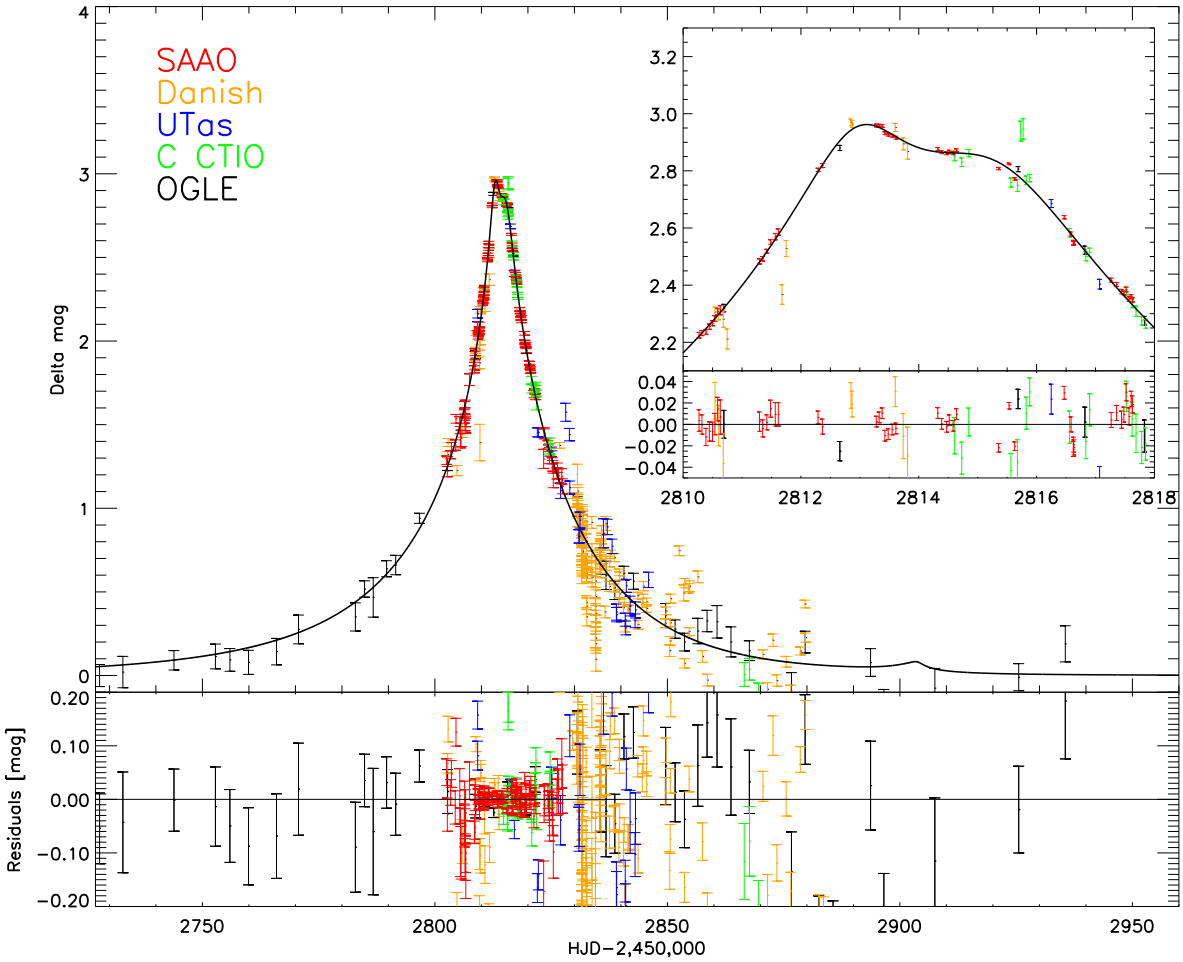


Figure 6.4: The best non-planetary, i.e. ordinary binary model found for OB-2003-BLG-208 has a mass ratio of $q = 0.19$ and a separation of $d = 0.31$.

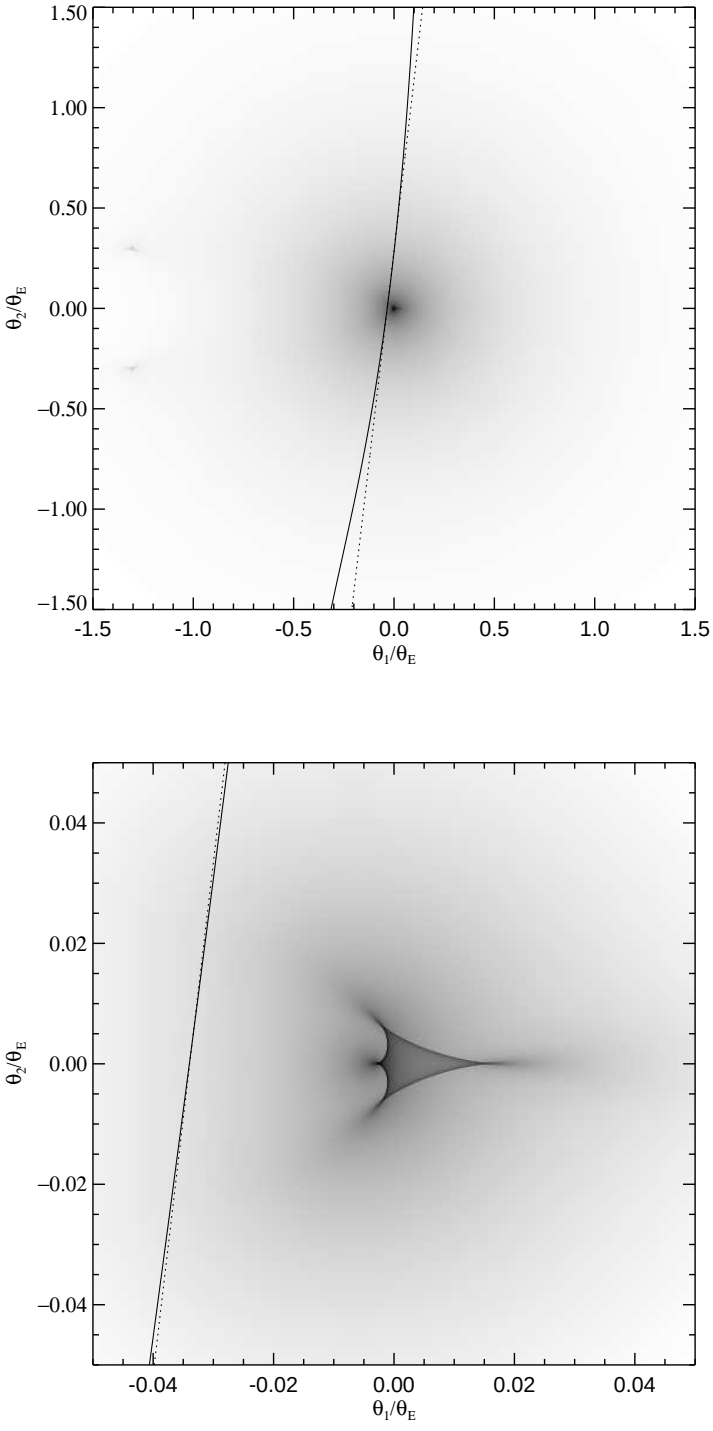


Figure 6.5: The caustic topology of the best planetary model. **Top:** Complete caustic topology with one central and two small triangular-shaped secondary caustics on the left side at $\sim (-1.4, \pm 0.3)$. **Bottom:** Zoom on the central caustic. Solid lines mark the source trajectory including annual parallax, and the dashed line the trajectory as seen from the Sun.

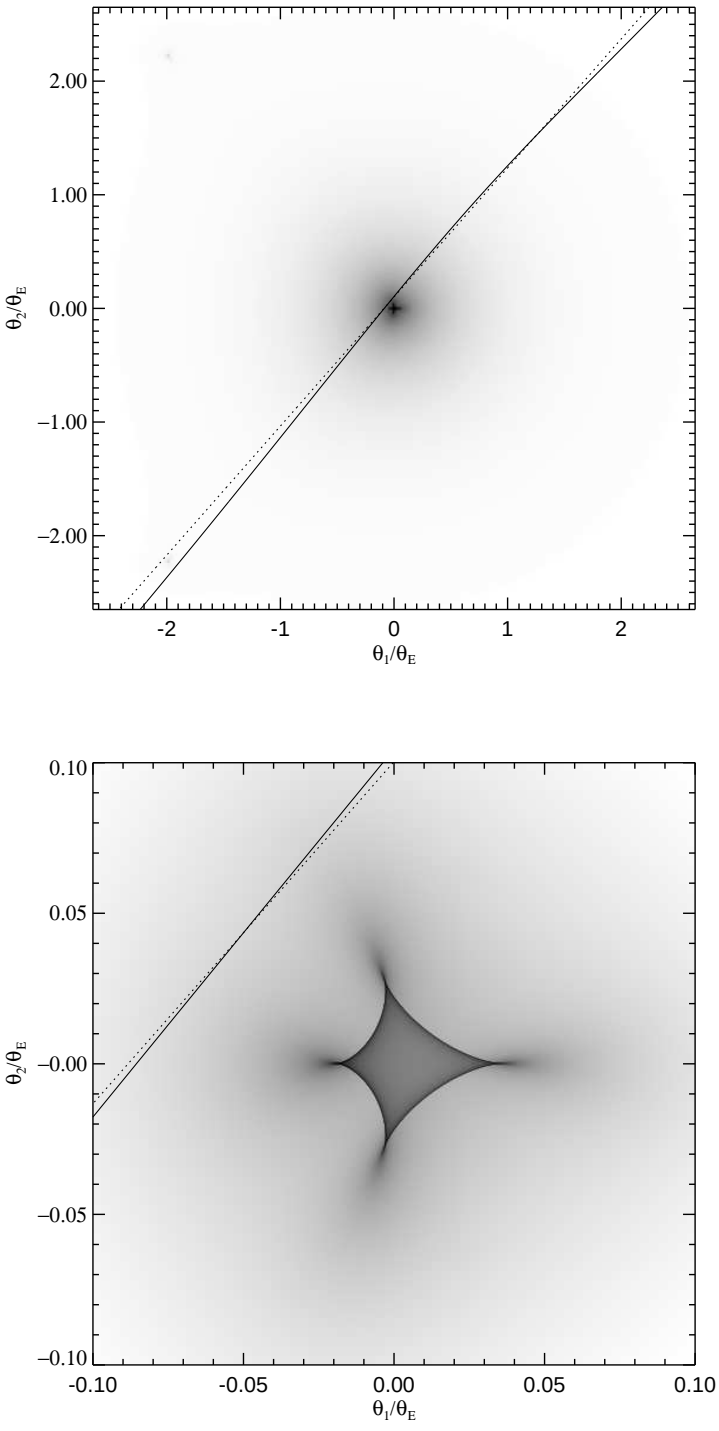


Figure 6.6: The caustic topology of the best non-planetary model. **Top:** Complete caustic topology with one central and two small triangular-shaped secondary caustics on the left side at $\sim (-2.0, \pm 2.2)$. **Bottom:** Zoom on the central caustic. Again, solid lines mark the source trajectory including annual parallax, and the dashed line the trajectory as seen from the Sun.

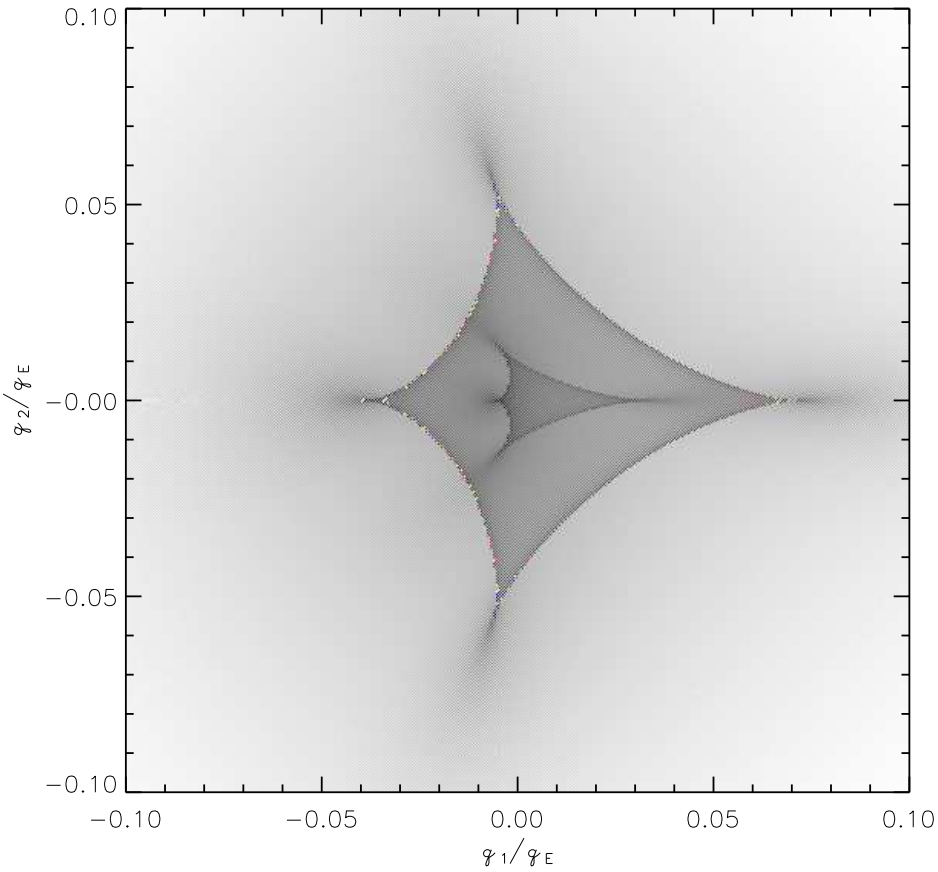


Figure 6.7: The central caustics of the planetary (inside) and non-planetary (outside) models plotted at the same scale. Although similar they are different enough to be distinguishable for observing campaigns like PLANET if the sampling is continuous over the course of the anomaly as the lightcurve models (Fig. 6.3, 6.4) show.

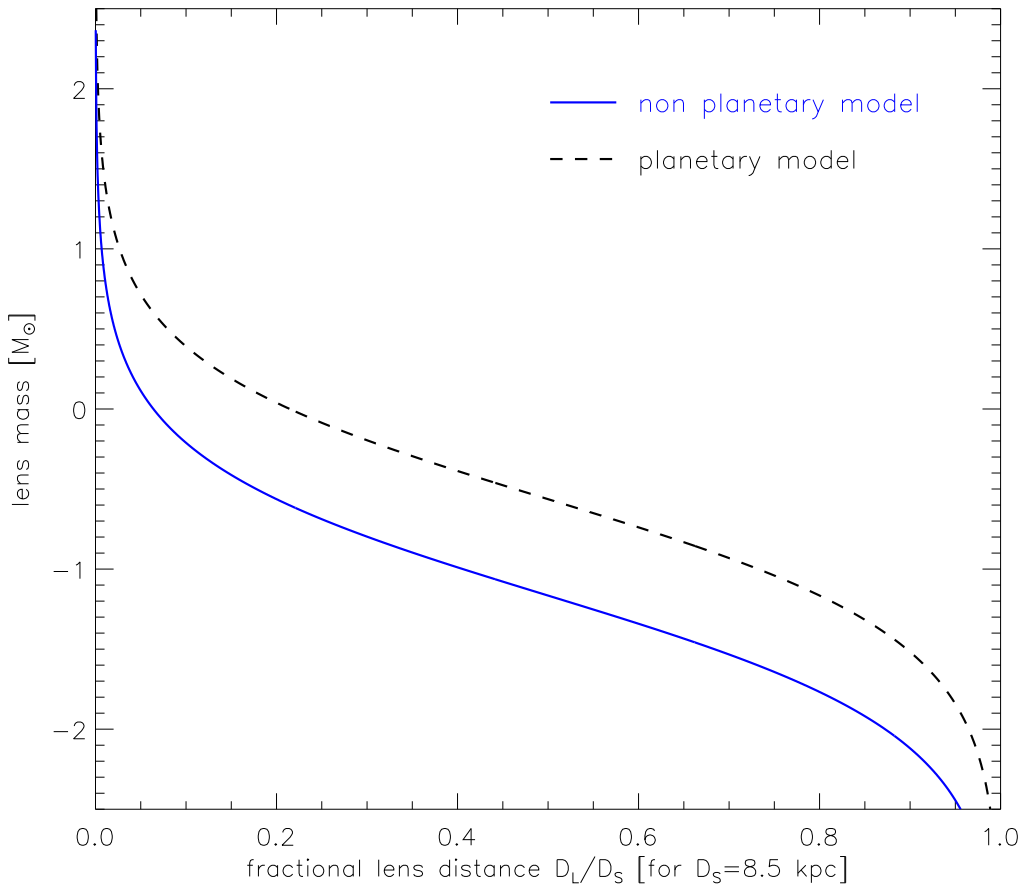


Figure 6.8: Lens mass constraints for planetary (dashed) and non-planetary (solid line) models from the annual parallax effect. Both models imply reasonable lens masses for typical lens scenarios, albeit the non-planetary model favors a closer and less massive lens than the planetary model.

| parameter | no planet | planet |
|---|---|---|
| $q$ | 0.187 | 0.009 |
| $d$ [$/R_{\rm E}$] | 0.312 | 0.537 |
| $u_0$ [$/R_{\rm E}$] | 0.0663 | 0.0337 |
| $\phi$ [deg] | 228.64 | 263.292 |
| $t_{\rm E}$ [days] | 32.216 | 63.877 |
| $t_0$[HJD$'$] | 2814.282 | 2814.130 |
| $\pi_{\rm E}$ | 0.46 | 0.23 |
| $\psi$ [deg] | 216.115 | 351.853 |
| $h_{\rm OGLE}$ | 0.61 | 0.78 |
| $\chi^2$/d.o.f. | 2141.35 / 376 | 2328.72 / 376 |

Table 6.1: Fit parameters of best planetary and non planetary models. The $\chi^2$ values are based on the raw photometric errors. i.e. without rescaling factors.

## 6.4 Conclusion

We note that the re-reduction of the data still is in progress (in particular the Danish data set) and could not be completed before submission of this thesis, so the exact values of the model parameters have to be taken with care, but that it is unlikely that the ambiguities in the models will disappear, cause the critical data gaps at the peak and the wings will persist. Despite the rather sobering result that the detection of planets in high amplification event peak anomalies is much more challenging than previously promoted (Rattenbury 2003; Griest & Safizadeh 1998) the encouraging lesson learned from OGLE-2003-BLG-208 is that it nevertheless is possible to detect planets in peak anomalies if a continuous/complete coverage of the peak is achieved. The caustics of the planetary and non planetary solutions are not identical and different enough for $1-2\%$ precision photometry. This is best done by either a network based campaign like PLANET, a space based telescope, or from Antarctica (Beaulieu et al. (2004) and Sec. 9.1.1). Single-site-only campaigns are most likely not able to break the ambiguities in the models (Gaudi & Han 2004) apart from the case where the caustic topology is very unique as in the only undisputed microlensing planet known to this date, the planet around lens in OGLE-2003-BLG-235/MOA-2003-BLG-053 (Bond et al. 2004).

# Chapter 7

# OGLE-2004-BLG-254

So with the Baxters on this side and the Rocco brothers on the other, I will be in the middle .

*Clint Eastwood in 'A few dollars more'*

## Abstract

When a single lens is transiting a source star during a microlensing event, we get the rare opportunity to constrain the center to limb variation of the source and the mass of the lens. As an example, we present the analysis of OGLE 2004-BLG-254, a high magnification ($A_{max} = 55$) and relatively short duration ($t_E = 13.2$ days) microlensing event. A high signal-to-noise ratio spectrum taken while the source was still amplified by $\approx 20$ showed that the source star was a K3II giant from the Sagittarius dwarf galaxy. We modeled the lightcurve with uniform brightness, linear and then square root limb darkening laws, including parallax effects. In contrast with some earlier studies, we do not approximate the magnification of the source, but use a general form. With the constraints from finite-source and weak parallax effects we constrain the mass of the lens to the range $0.1 \lesssim M/M_{\odot} \lesssim 4$.

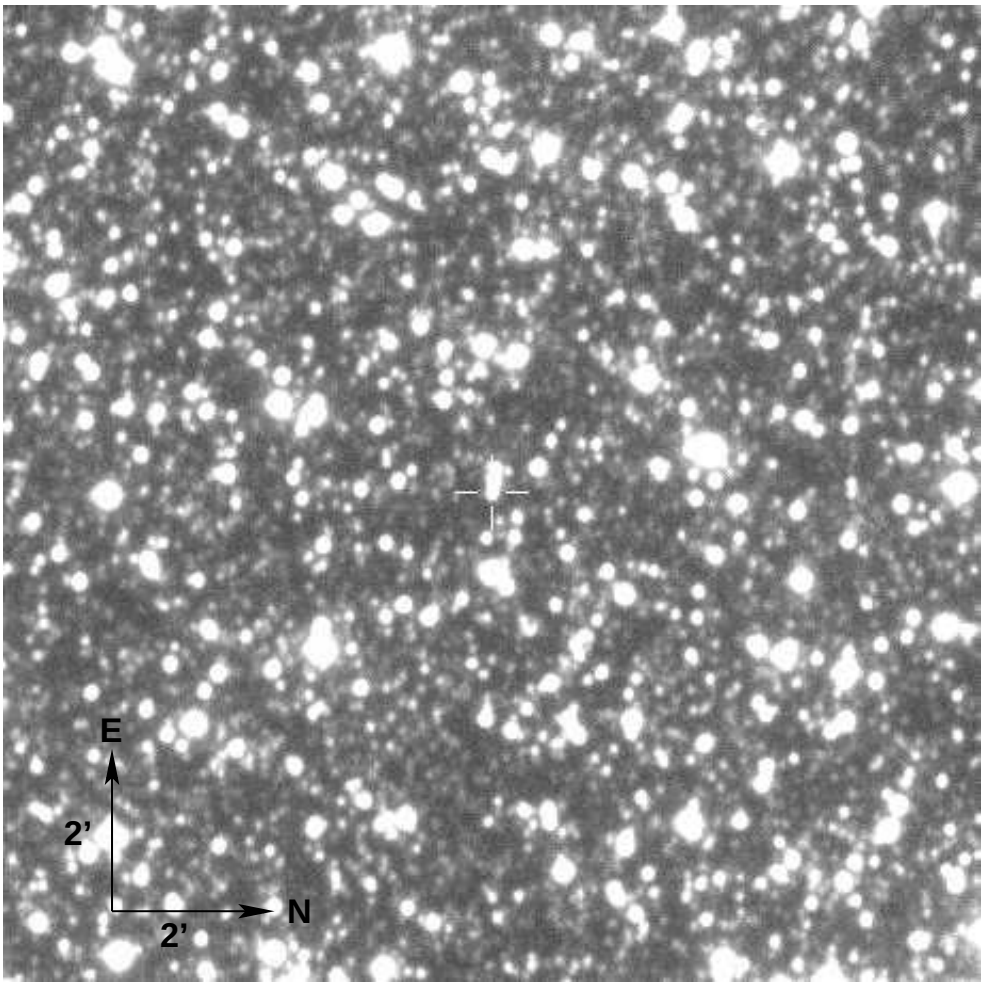


Figure 7.1: Finding chart of OGLE-2004-BLG-254 event. Again North is right and East is up on this $2' \times 2'$ sized frame and the position of the lensed source is at the center of the cross. Although part of a close chain of three stars its brightness ($I_{\rm OGLE} \sim 16.4$ mag) enables quite stable and precise photometry as can be seen in Fig. 7.5. (credit: OGLE's page www.astrouw.edu.pl/∼ogle/ogle3/ews/ews.html)

## 7.1 Introduction

Although binary lenses due to their extended caustics have a larger cross section for finite-source effects, also the point-like[1] caustic from a single lens can be sensitive to extended sources, namely when the impact parameter is of the order of the source size, i.e. in high amplification events with $u_o \lesssim 0.02$ for typical lens scenarios. The point caustic can then transit the source and as in binary lens caustic passages probe the source surface with high resolution. The resulting lightcurve is (neglecting possible asymmetries induced by nonlinear relative motion and other higher order effects) symmetric as in the single lens case, however the peak is broadened and flattened. These rare transits also provide the unique possibility to measure/constrain the mass of a single star (Ghosh et al. 2004; Jiang et al. 2004), having in mind that the majority of star mass measurements (apart from the Sun) stem from binary/multiple star systems. The OGLE-2004-BLG-254 event presented here is the best existing data set up to now of such a phenomena.

## 7.2 Photometric measurements

The OGLE Early Warning System (EWS) (Udalski 2003) alerted the Bulge giant OGLE 2004-BLG-254 as being a potential high magnification event on June 3, 2004. OGLE-III observations were carried out with the 1.3 m Warsaw Telescope at the Las Campanas Observatory, Chile, which is operated by the Carnegie Institution of Washington. Photometry was obtained with the OGLE-III image subtraction technique data pipeline (Udalski et al. 2002) based in part on the (Wozniak 2000b) image subtraction implementation of ISIS (Alard & Lupton 1998; Alard 2000).

The PLANET collaboration started its photometric observations on June 8 which form the basis for our analysis and consist of data from 5 different telescopes being part of the PLANET network: the Danish 1.54m at ESO La Silla (Chile), the Canopus 1m near Hobart (Tasmania), the Perth/Lowell 0.6m at Bickley (Western Australia), the Elizabeth 1m at the South African Astronomical Observatory (SAAO) at Sutherland (South Africa) and the Rockefeller 1.5m of the Boyden observatory at Bloemfontein (South Africa). The event was also monitored by MicroFUN from Chile with the 1.3m (ex-2MASS) telescope at the Cerro Tololo Inter-American Observatory, using ANDICAM, which simultaneously takes images at optical and infrared wavelengths (DePoy et al. 2003). Data collected by PLANET, OGLE, and MicroFUN showed a rise in magnification by 2.85 mag above baseline until 9-Jun, 8:10 UT. These data and adequate real-time modeling indicated a peak to occur on 10-Jun, $6{:}35^{+20\mathrm{min}}_{-30\mathrm{min}}$ UT, at a rather uncertain, but in any case large, magnification of $80^{+70}_{-30}$.

Events of this type harbor an exceptional potential for the discovery or exclusion of extra-solar planets (see Sec. 8) as well as for the study of stellar atmospheres and might provide an opportunity for measuring the mass of the lens star.

[1] True lenses are not point-like and so there are no real point caustics, but finite-lens effects in galactic microlensing events are not observable with current instruments. Their astrometric signatures, in the order of micro arc-sec, however may be within the reach of future space mission like SIM (Takahashi 2003).

On 10-Jun at 12:45 UT, a public alert was issued by PLANET, reporting that data collected on OGLE 2004-BLG-254 at the SAAO 1.0m between Jun-9, 18:50 UT and Jun-10, 4:40 UT, at the Danish 1.54m on Jun-10 between 2:20 UT and 10:05 UT, as well as OGLE data obtained on Jun-10 between 3:50 UT and 9:55 UT, revealed the extended size of the source star, and the passage time of its radius was evaluated to about 16 hours. The peak was passed around 10-Jun, 7:40 UT at 4.35 mag above baseline, i.e. at an amplification of $\sim 55$.

## 7.3 Spectroscopic measurements

We have obtained a high-resolution spectrum of OGLE 2004-254 by use of Target-of-Opportunity-time at the UVES spectrograph mounted at the Nasmyth focus of Kueyen, the second VLT unit (UT2) on June 11, 2004, between 00:24 and 00:52 UT, while the source flux was magnified by the microgravitational lens by a factor 20 (which made the VLT equivalent to a $\sim$ 37m diameter telescope at this moment). The spectrum was taken in one of the standard red setting centered at 5800 Å . The red arm of the UVES instrument is equipped with two CCDs, one EEV for the bluer part of the spectra and a MIT for the red part.With the selected set up (called 580) we are able to cover the spectral domain $4780 - 5758$ Å on the EEV CCD and $5835 - 6808$ Å on the MIT one at a resolution of $\sim 40\,000$.

## 7.4 Nature of source star from UVES spectroscopy

We have analyzed the spectrum by comparison with a small grid of synthetic spectra that we have computed at the same resolution as the observed spectrum. The spectra are based on MARCS model atmospheres (Gustafsson et al. 1975), computed with the version of the code described in Jørgensen et al. (1992) with later updates. The later update of highest importance for the present project, is the inclusion of atomic line opacity samplings, based on the VALD data base (Kupka et al. 1999) of transitions in neutral and one time ionized atoms. The VALD data base is used for the model atmospheres as well as the spectrum computations. The spectrum shows approximately 10 000 well defined lines, and almost all of them are identifiable from comparison with line position and strength of the transitions listed in the VALD data base. Line profiles are computed as Voigt profiles with the necessary broadening parameters taken from the data base. Among the many atomic lines, we have selected three particularly well suited systems of strong Mg, Cr, and Na lines whose intensity and line shapes are fitted to give a first estimate of the fundamental parameters: effective temperature ($T_{\rm eff}$), surface gravity ($\log g$) and metallicity ($Z$).

Using this set of parameters, a synthetic spectrum of the star is computed and we controlled the validity of the model by comparing against a large number of medium to weak lines throughout the observed spectrum. This in addition will allow us to determine variations of the abundances for other elements.

### 7.4.1 Magnesium lines

The triplet of neutral magnesium lines around 5175 Å is well suited to put limits on the temperature and gravity, while it is relatively insensitive to metalicity (magnesium abundance) within reasonable limits. The line system overlaps with the position of a relatively strong MgH band, and the ratio between Mg and MgH is sensitive to temperature as well as gravity. For high values of the gravity, the atomic magnesium triplet lines become very broad and the ratio between Mg and MgH shifts in favor of MgH. Also for low temperatures the balance shifts in favor of MgH, so that the shape and the intensity of the atomic lines can be used together with the ratio (or absence) of the intensity of MgH relative to the intensity of the atomic Mg lines to give information on temperature and gravity.

The absence of MgH in our observed spectrum allows us to conclude that the star is not cooler than 4000 K. The broadness of the atomic Mg lines allows us to confine the value of $\log g < 2.0$. The synthetic spectrum of the triplet Mg lines is not very sensitive to $Z$, and any value from slightly above solar to as low as $1/3\ Z_\odot$ leads to good fits. The medium strong neutral atomic Mg line at 5711 Å is known to respond opposite to the triplet lines to changes in gravity, i.e. to become stronger for decreasing gravity. The synthetic line is obviously too deep for models with $\log g = 0.0$ and solar metallicity, while it becomes too narrow for values much above 0.

Good fits are obtained to all the Mg lines for $T_{\rm eff} = 4100 \pm 100$ K, $\log g = 1.0 \pm 0.5$ and $Z \approx 0.5$. Fig. 7.2 shows the observed spectrum around the three strong Mg lines, from 5165 Å to 5187 Å, superimposed by a synthetic spectrum of a star with $T_{\rm eff} = 4100$ K, $\log g = 1.0$ and $Z = 0.6\ Z_\odot$.

### 7.4.2 Chromium lines

As for the Mg triplet region, the MgH molecular system also has a relatively strong band in the region of a triplet of three strong chromium lines at 5204.51, 5206.04 and 5208.42 Å, which limits $T_{\rm eff}$ to be no less than 4000 K. Also models of $T_{\rm eff} = 4200$ K fit the Cr lines well, while models of $T_{\rm eff} = 4400$ K result in too weak Cr lines (even for $Z = Z_\odot$) while the weaker lines in the same region are too strong at this temperature. We therefore conclude from the region of the chromium lines that $T_{\rm eff}$ is in the range $4000 - 4200$ K.

The chromium system is less sensitive to gravity, and even values as low as $\log g = 0.0$ are in good agreement with the observed spectrum of these lines. On the other hand the lines are sensitive to the value of $Z$ (the Chromium abundance), and $Z = 0.3\ Z_\odot$ tends to be on the lower side of good fits, while $Z = Z_\odot$ is obviously too high.

Fig. 7.3 shows the observed spectrum around the three strong Cr lines, from 5190 Å to 5220 Å, superimposed by a synthetic spectrum of a star with $T_{\rm eff} = 4100$ K, $\log g = 1.0$ and $Z = 0.6\ Z_\odot$.

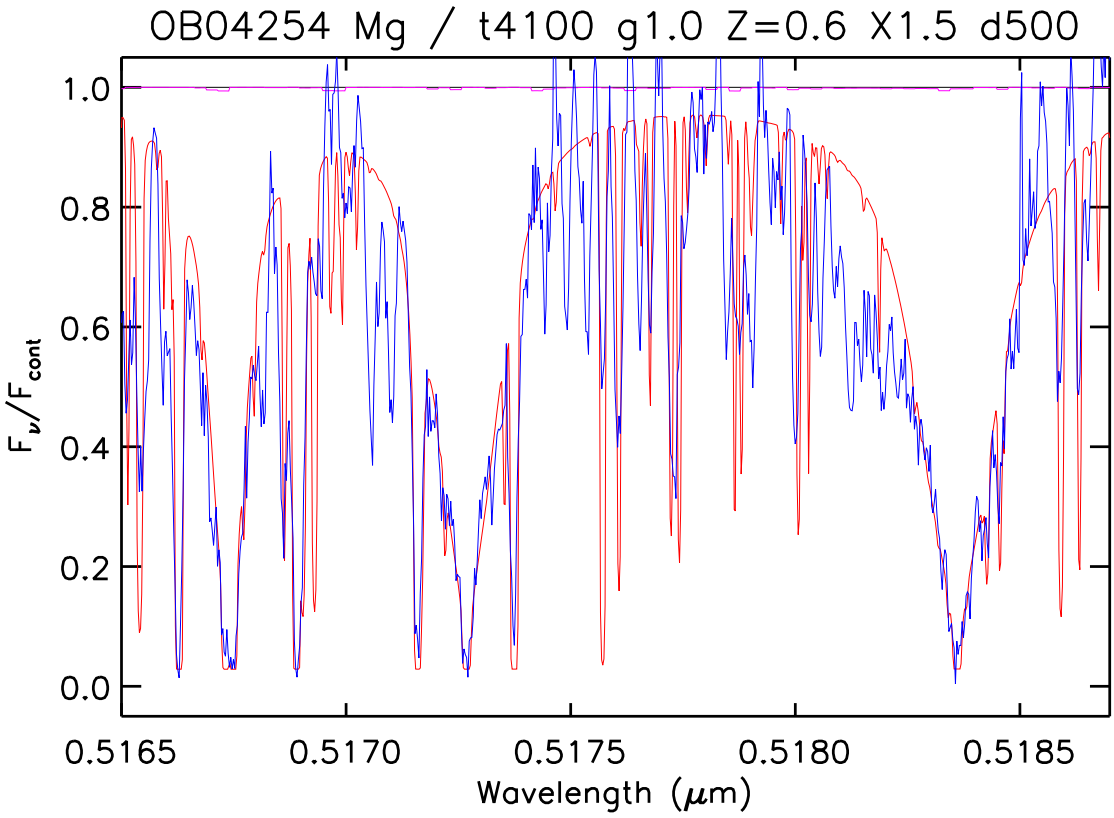


Figure 7.2: The observed (solid blue line) and computed (dotted red line) spectrum in the region around the 5167.3, 5172.7, 5183.6 Å Mg lines. The computed spectrum is based on a stellar model of $T_{\rm eff} = 4100\,{\rm K}$, $\log g = 1.0$ and $Z = 0.6\,Z_{\odot}$. The observed spectrum is shifted by 139.2 Kms$^{-1}$ to the rest frame.

### 7.4.3 NaD lines at 5890/5896 Å and other neutral sodium lines

The intensity and form of the NaD lines are very sensitive to $T_{\rm eff}$ as well as to gravity and (sodium) abundance. Often these lines are not useful for determination of the fundamental parameters and abundances, because interstellar absorption saturates or changes the intensity of the lines. In this case, however, the main component of the interstellar absorption is at a redshift of +122 km/s relative to the star, and the intrinsic stellar NaD lines are very strong and seem to be only moderately affected by interstellar absorption. The fact that the fundamental parameters derived from the NaD lines are in good agreement with the parameters derived from the other stellar lines, also indicates that the interstellar absorption is small, even though it is certainly visible (see Fig. 7.4).

Model spectra from our grid with high metallicity ($Z = 3$), with high gravity ($\log g = 3$) or low $T_{\rm eff}$, all give far too broad NaD lines compared to the observed spectrum, and can therefore be excluded. Models of low gravity ($\log g = 0$), high $T_{\rm eff}$ ($T_{\rm eff} = 4200\,{\rm K}$), or low $Z$ ($Z = 0.3\ Z_{\odot}$), on the other hand give too narrow lines compared to the observed lines.

Fig. 7.4 shows the observed spectrum around the two NaD lines, from 5882 Å to 5902

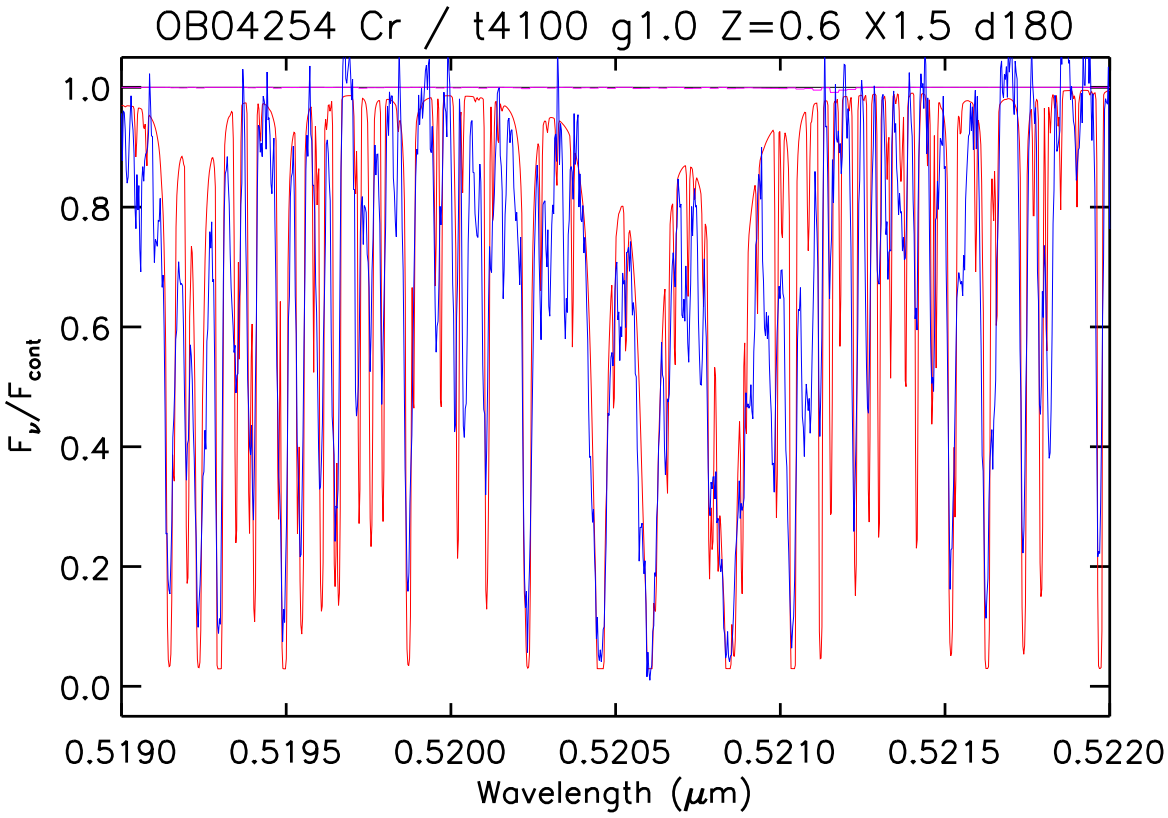


Figure 7.3: The observed (solid blue line) and computed (dotted red line) spectrum in the region around the three strong Cr lines, from 5190 Å to 5220 Å, computed in the same way as in Fig.7.2.

Å, superimposed by a synthetic spectrum of a star with $T_{\rm eff} = 4100\,{\rm K}$ and $\log g = 1.0$, and $Z = 0.6\ Z_\odot$.

We conclude that the Mg, Cr, and Na lines are well fitted by models in the range $T_{\rm eff} = 4100 \pm 100\,{\rm K}$, $\log g = 1.0 \pm 0.5$ and $Z = 0.6 \pm 0.2\ Z_\odot$. This corresponds to a slightly metal deficient bright giant star of spectral class approximately K3II, at a distance (and direction) of the Sagittarius dwarf galaxy and $R/R_\odot = (1.31 \pm 0.07)\ D_{\rm S}/{\rm kpc}$. The line positions fit the lines of the data base with a general offset of +134 km/s, which is also consistent with the star being a member of the Sagittarius dwarf galaxy. This star, although cooler, has the same metallicity and similar radial velocity to the two Sagittarius giants studied by Bonifacio et al. (2000).

Finally we note that since the spectrum is of remarkably high resolution and signal to noise for a star of the Sagittarius dwarf galaxy, it offers the potential of a detailed, high quality abundance analysis, which is however beyond the scope of this Chapter and will be presented elsewhere.

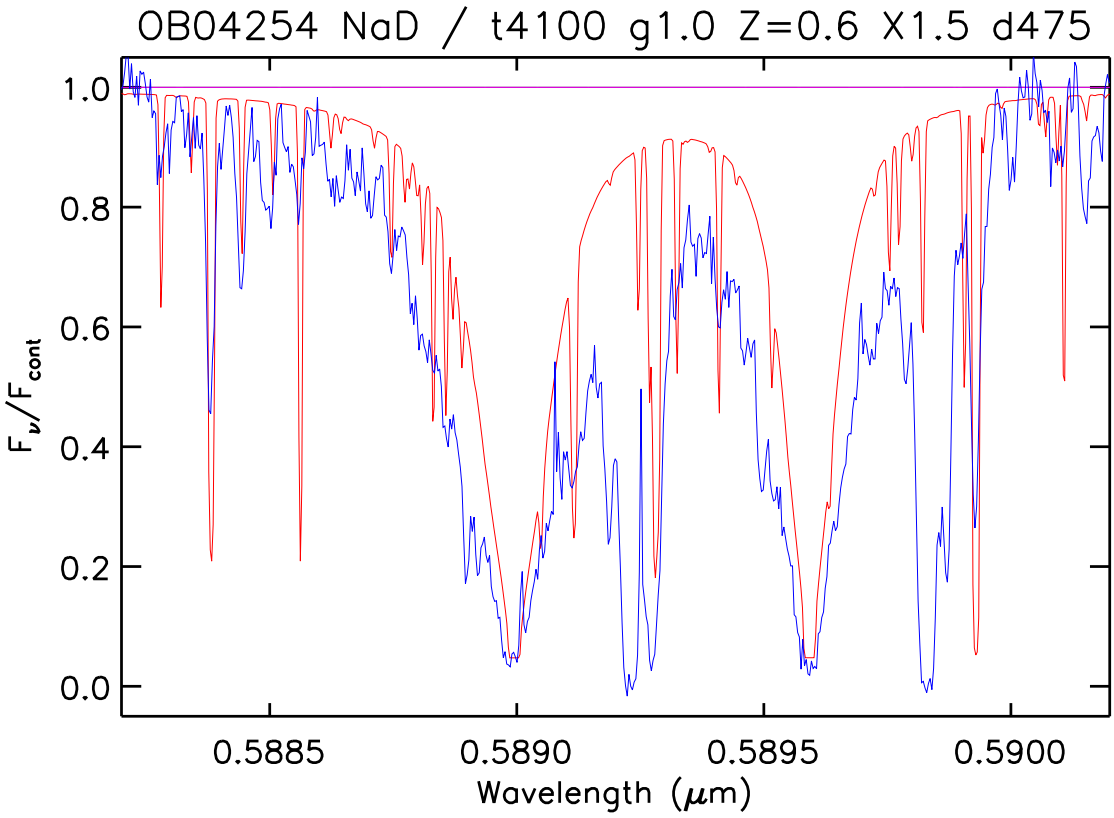


Figure 7.4: The observed (solid blue line) and computed (dotted red line) spectrum in the region around the two NaD lines, from 5882 Å to 5902 Å, computed in the same way as in Fig.7.2.

## 7.5 Lightcurve modelling

### 7.5.1 Extended source formalism

The photometric data collected on OGLE 2004-BLG-254 clearly show that the lightcurve is affected by extended source effects. While the magnification of a point source at the projected distance $u$ from the lens (in unit of the Einstein radius $\Theta_{\rm E}$, see Sec. 1.4) is given by

$$A(u) = \frac{u^2+2}{u\sqrt{u^2+4}}, \tag{7.1}$$

the magnification of an extended source with angular radius $\rho_*$reads

$$A(u|\xi,\rho_*) = \frac{1}{\pi} \times \int_0^{2\pi} \int_0^1 \xi(r) r A\left(\rho_* \sqrt{r^2 - \ 2(u/\rho_*) r\cos(\phi) + (u/\rho_*)^2}\right) \mathrm{d}\varphi\, \mathrm{d}r. \tag{7.2}$$

Here, $\xi(r)$ is the brightness profile of the source and $r$ denotes the fractional stellar radius ($0 \leq \rho \leq 1$).

For a uniformly bright source ($\xi(r) \equiv 1$), Witt & Mao (1994b) have derived a semi-analytic expression for $A(u|\xi,\rho_*)$ involving elliptical integrals, but for other profiles, such as

power-law limb-darkening models, no corresponding expressions are known. Based on the fact that extended source effects are only prominent for small angular separations between lens and source ($u \ll 1$), where $A(u) \simeq u^{-1}$, Gould (1994) found that the extended-source magnification $A(u|\xi, \rho_*)$ can be written more simply as product of the point-source magnification $A(u)$ and a factor $B(z)$, namely

$$A(u|\xi, \rho_*) = A(u)\, B(u/\rho_*; \xi)\,, \tag{7.3}$$

where

$$B(z;\xi) = \frac{1}{\pi} \int_0^{2\pi} \int_0^1 \xi(r)\, \frac{z}{\sqrt{r^2 + 2rz\cos\varphi + z^2}}\, r\, \mathrm{d}r\, \mathrm{d}\varphi. \tag{7.4}$$

The validity of this approximation for typical parameters of finite-source events has been confirmed by Yoo et al. (2004b), who also found that for a uniformly bright source $B_0(z) = B(z; \xi \equiv 1)$ reads

$$B_0(z) = \frac{4}{\pi}\, z \times \begin{cases} E(\pi/2, z) & \text{for} \quad z \leq 1 \\ E(\arcsin z^{-1}, z) & \text{for} \quad z > 1 \end{cases}\,, \tag{7.5}$$

where

$$E(\varphi, k) = \int_0^{\varphi} \sqrt{1 - k^2\, \sin^2\varphi}\, \mathrm{d}\varphi \tag{7.6}$$

is the incomplete elliptical integral of the second kind (e.g. Gradshteyn & Ryzhik 1980; notice the formula given by Yoo et al. (2004b) is not properly defined by referring to this notation and is corrected here). Another efficient technique has also been used by Heyrovský (2003) to deal with arbitrary limb-darkened source profiles: he calculates analytically the angular integral in Eq. (7.2) so that only a radial integral containing the limb-darkening profile remains to be calculated numerically.

### 7.5.2 Limb-darkened source fit

In the photometric analysis of the event, both PLANET and OGLE data are being used. For each PLANET observation site, we have applied a cut on seeing which only removes very unreliable points ; we restricted the complete OGLE data to the ones collected after $\mathrm{HJD}' = 3050.0$ (which is large enough to derive the baseline magnitude). OGLE provides us with 106 data points, SAAO 80 (seeing $< 2.0''$), UTas 37 (seeing $< 3.1''$), Boyden 74 (seeing $< 4.8''$) and Danish 205 (seeing $< 2.0''$), for an amount of 502 measurements from 5 observing sites. As mentioned earlier, our DoPhot based pipeline does provide under estimated photometric errors (e.g. for bright magnitude, error estimates can become of the order of $10^{-3}$ which is unrealistic). Comparison with scatter of the bulk of non variable stars suggests that an order of magnitude of underestimation of errors is 20 %. Therefore, as a new standard in forthcoming analysis based on PLANET data, we modify the errors in the following way: $\sigma^2 = (1.2\ \sigma_{\mathrm{DoPhot}})^2 + (0.01)^2$ for every observing site.

The source star being a K3 giant, we first check weather the fluctuation in the OGLE baseline magnitude is periodic or not. We compute a power spectrum of 115 baseline data

points coming from OGLE, and find that the spectrum is compatible with observational noise, and that we do not have a periodic modulation greater than $\sigma_{\rm noise}$ in the range $1-12$ days.

A point-lens-uniform-(extended)-source model provides us with a first working set of parameters for our $\chi^2$ minimization scheme. At this stage, the residuals of the fit show some symmetric trends around the peak of the light curve, which clearly indicate limb darkening of the source star has to be taken into account. We therefore add a linear limb darkening to the source (see also Sec. 2.2.3), so that $\xi(\mu) = 1 - a_1(1-\mu)$, where $\mu = \cos(\theta)$ is the emergent angle from its surface. This parameterization involves a total of 17 free parameters: three basic microlensing parameters, $t_0$ (time of closest approach), $u_0$ (minimum impact parameter), $t_{\rm E}$ (Einstein ring radius crossing time), the source size $\rho_*$ (in unit of $\Theta_{\rm E}$), two annual parallax parameters $\eta$ (see Sec. 7.6) and $\psi$, one linear limb darkening coefficient $a_1$ and five baseline magnitudes plus five blending parameters.

The best corresponding parameters fitting the data are given in Tab. 7.1. We also tested a square root limb darkening law, which can be written $\xi(\mu) = 1-a_1(1-\mu)-a_{1/2}(1-\sqrt{\mu})$ and involves one more parameter than the linear limb darkening. We note that the $\chi^2$ we obtain is very similar to the one with the linear limb darkening law and leads to no significant improvement.

We further remark that the blending fraction of the different PLANET sites can be very different. The blend at $1.4''$ from the target is not disentangled from OGLE 2004-BLG-254 by Boyden and Canopus observations, whereas it is in SAAO and Danish. Moreover, we obtain a nearly zero blend from OGLE, which is in agreement with data being reduced by image subtraction.

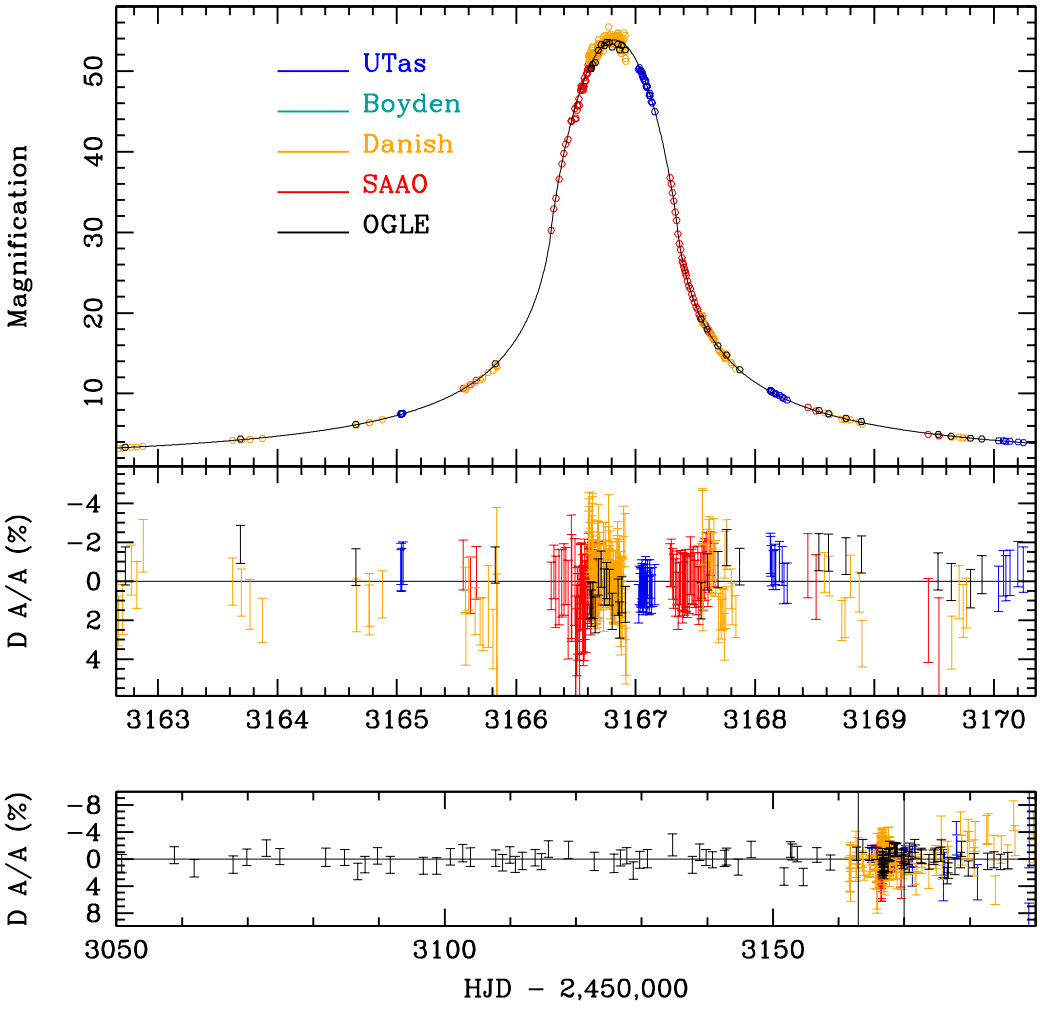


Figure 7.5: The upper panel shows the photometry of the microlensing event OGLE 2004-BLG-254 near its peak, on 2004 June 10, observed by four PLANET sites, Danish 1.54m, UTas 1m, Perth 0.6m, Boyden 1.5m and SAAO 1.0m and OGLE. The solid line is the best point-lens, linear limb darkened extended source model. On the middle panel are plotted the residuals of the peak region fit, whereas the lower panel shows the residuals of the complete set of data (the two vertical lines indicate the peak region displayed above).

Table 7.1: Parameters for the best point-lens-extended source models for linear and square root limb darkening law.

| Parameters | Linear | Square root |
|---|---|---|
| $t_0$ (days) | $3166.8223^{+0.013}_{-0.001}$ | 3166.8221 |
| $u_0$ | $0.01^{+9.1}_{-0.001}$ $.10^{-3}$ | 1.27 $.10^{-3}$ |
| $t_E$ (days) | $13.17^{+0.7}_{-0.2}$ | 13.09 |
| $\rho_*$ | $4.07^{+0.02}_{-0.25}$ $.10^{-2}$ | 4.11 $.10^{-2}$ |
| $a_1$ | $0.64^{+0.13}_{-0.16}$ | 0.59 |
| $a_{1/2}$ - | - | 0.12 |
| $\eta$ | $4.2^{+6.1}_{-8.0}$ $.10^{-2}$ | 4.2 $.10^{-2}$ |
| $(F_b/F_S)_{\rm SAAO}$ | 0.64 | 0.67 |
| $(F_b/F_S)_{\rm Danish}$ | 0.024 | 1.0 $.10^{-2}$ |
| $(F_b/F_S)_{\rm UTas}$ | 0.55 | 0.55 |
| $(F_b/F_S)_{\rm Boyden}$ | - | - |
| $(F_b/F_S)_{\rm OGLE}$ | 1.0 $.10^{-3}$ | 1.0 $.10^{-3}$ |
| $\chi^2/dof$ | 1.03 | 1.02 |

A comparison between the exact formula and the approximation of Yoo et al. (2004b) led to a maximal relative discrepancy of $2.0 \times 10^{-4}$ at the peak and $1.5 \times 10^{-4}$ close to the limb. This suggests that this approximation can be used safely, however we note it does not lead to a much shorter computing time.

## 7.6 Constraints on the lens

As discussed in Sec. 7.4, the source is most likely situated in the Sagittarius dwarf galaxy, at a distance $D_{\rm S} \approx 24$ kpc. We recall that the location of the lens (at distance $D_{\rm L}$) can be constrained by two equations: one coming from the comparison of the fitted value of the source ($\rho_*$, in unit of the Einstein radius) and its physical size determined with the spectroscopic analysis; the other equation involves the parallax parameter $\eta$ determined from the fit (e.g. Kubas et al. 2005a, respectively Chap. 5 ). With $x$ being the fractional distance of the lens, $x = D_{\rm L}/D_{\rm S}$, the Einstein radius reads

$$\theta_{\rm E} = \sqrt{\frac{4GM}{c^2\ D_S}\frac{1-x}{x}}. \tag{7.7}$$

Let $R_*$ and $a_\oplus$ be the physical source radius and the semi-major axis of the Earth motion around the Sun (assumed to be circular), the two equations can then be written:

$$\frac{M(x)}{M_\odot} = \frac{c^2}{4GM_\odot D_{\rm S}}\frac{{R_*}^2}{{\rho_*}^2}\frac{x}{1-x}, \tag{7.8}$$

using the extended source effect, and

$$\frac{M(x)}{M_\odot} = \frac{c^2}{4GM_\odot D_\mathrm{S}} \frac{a_\oplus^2}{\eta^2} \frac{1-x}{x}, \tag{7.9}$$

when taking into account the parallax. The parameter $\eta$ introduced here is related to the annual parallax $\pi_\mathrm{E}$ by

$$\pi_\mathrm{E} = |\eta| \ \Theta_\mathrm{E}. \tag{7.10}$$

From the parameter error bars given in Tab. 7.1, it appears that the fitted source radius $\rho_*$ is well constrained, whereas one can just put an upper limit on the value of the parallax parameter $\eta$. According to Eq. (7.9), this will provide us with a minimum value on the lens mass; we take this upper limit to be $\eta_{max} \approx 0.12$.

In Fig. 7.6, we plot the relations from above between the lens mass $M$ and the fractional distance of the lens $x$ in dependence from finite source size effects (Eq. 7.8) and parallax effects (Eq. 7.9). From this Figure, the lens must therefore be located at a distance $D_\mathrm{L} > 19$ kpc, and its mass must be greater than 0.1 $M_\odot$. If one assumes the thickness of Sagittarius in this particular line of sight to be around 2 kpc, the minimal mass of a lens located within Sagittarius is then 0.4 $M_\odot$.

We also note from the fit that the blend fraction found in the Danish telescope photometry is $F_b/F_S \approx 0.01$, which gives a maximal value of 10 $L_\odot$ for the lens, a value in agreement with a lens mass in the range $0.1 - 4\ M_\odot$.

## 7.7 Discussion

We have performed a dense photometric monitoring of the microlensing event OGLE 2004-BLG-254, a relatively short duration ($t_E = 13.2$ days), small impact parameter ($u = 0.00$) microlensing generated by a point mass lens transiting a giant. It peaked at an amplification of 55.

The analysis of UVES spectra taken while the source was amplified by a factor $\approx 20$ just after the end of the transit of the caustic over the source yielded precise measurement of the characteristics of the star, a K3II with $T_\mathrm{eff} = 4100 \pm 100\,\mathrm{K}$, $\log g = 1.0 \pm 0.5$ and $Z = 0.6 \pm 0.2 Z_\odot$. The projected radius of the source is $6.1 \pm 0.3\ \mu as$, corresponding to $R/R_\odot = (1.31 \pm 0.07)\ D_\mathrm{S}/\mathrm{kpc}$. Its radial velocity of 139.2 km s$^{-1}$ and luminosity suggests that it is a Sagittarius dwarf galaxy giant. We note that at its galactic coordinates (l=358.096, b=-3.87), the microlensing rate due to Sagittarius estimated by Cseresnjes & Alard (2001) is significant.

The short time scale of the event only allows to put an upper limit on parallax effects, suggesting (assuming the hypothesis of source being in Sagittarius is correct) the lens to be located at $D_\mathrm{L} \gtrsim 19$ kpc and with a mass in the range $0.1 \lesssim M_\mathrm{L}/M_\odot \lesssim 4$, where the upper mass bound results from the argument that a more massive and luminous lens would imply a higher than observed blend fraction. These constraints lead to the possibility that either the lens belongs to the far disc of our galaxy or also to Sagittarius. The latter scenario,

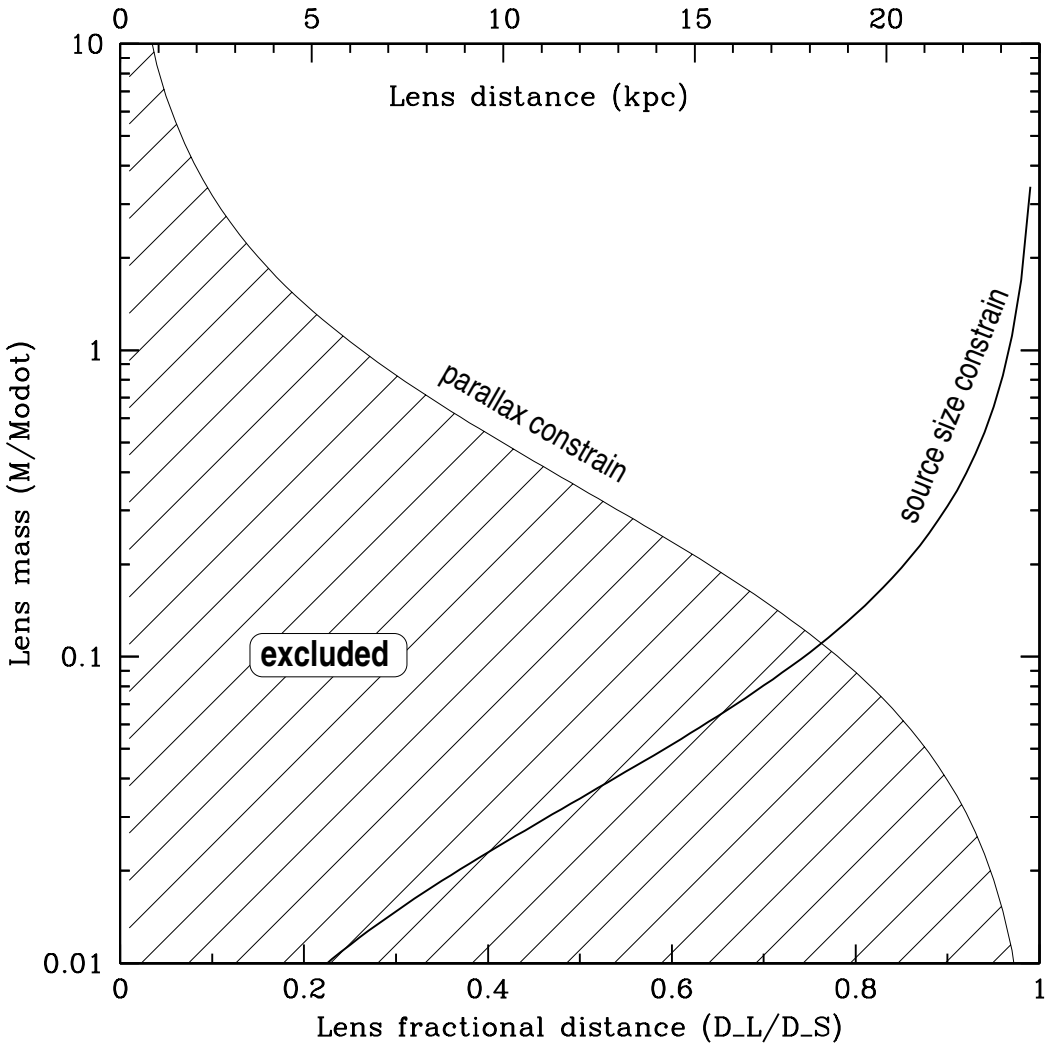


Figure 7.6: Constraints on the lens mass and lens distance from parallax and source size effects, assuming a source at $D_{\rm S} \approx 24$ kpc. Taking the upper limit $\eta = \eta_{max} = 0.12$ gives a lower limit on the mass of the lens, i.e. the lower shaded region is not allowed.

which would be the first reported case of self-lensing in Sagittarius, could however only be satisfyingly reconciled with the rather short event time scale, if the lens belongs to the debris stream, where the velocity dispersion is much larger than the $(11.4 \pm 0.7)$ kms$^{-1}$ in the central regions of Sagittarius.

# Chapter 8

# Constraining the presence of planets around the lens

> But little they know, that it's so hard to find. One rich man in ten with a satisfied mind.
>
> *Johnny Cash, 'A satisfied mind'*

## 8.1 Abstract

From the absence of planetary anomalies in apparent single-lens lightcurves, one can put constraints on the allowed parameter space of planets around the lens. We present a method to quantify planetary detection efficiencies, which extends and refines previous studies (Gaudi et al. 2002) by taking into account the source size. Although current microlensing campaigns are only sensitive to Jovian companions, where finite source effects can be neglected, future microlensing searches will most likely be sensitive to Earth masses and will require extended source modeling for proper data interpretation.
With the framework outlayed below and given a large sample of microlensing events, one can derive upper limits on the Galactic abundance of planets. In a forthcoming analysis we aim to strengthen the constraints on the abundance of Jovian planets in the lensing zone around M-dwarfs (Gaudi et al. 2002), using the PLANET 1995-2004 microlensing data set.

## 8.2 Introduction

While as of spring 2005 about 2000 microlensing events have been observed since the mid 90's, only one planet has left a convincing signal in the measured lightcurves, namely the Jovian like planet around the lens of the OGLE 2003-BLG-235/MOA 2003-BLG-53 event (Bond et al. 2004). Unfortunately it seems that the parameter region where microlensing is most sensitive to planets, i.e. Jovian planets in the lensing zone (Sec. 2.1.1) is scarcely populated by nature[1]. Gaudi et al. (2002) concluded that less than 1/3 of M-dwarfs have Jovian companions within $1-4$ AU. We have extended and refined their approach, aiming to strengthen these constraints and to push the mass limits further down, by allowing for extended source effects and using a larger sample of events.

## 8.3 Detection/Exclusion efficiency

Although a planetary companion around the lens can significantly distort the single lens lightcurve (Sec. 2.1) the parameters $u_o, t_o, t_\mathrm{E}$ will be very close to the lens model without a planet. For a fixed configuration of separation $d$ and mass ratio $q$ a decisive parameter, whether the planetary caustic will be hit by the source track or not, is the impact angle $\phi$ (as illustrated in Fig. 8.1), apart from tracks with very small impact parameter which reveal the presence of planetary/binary central caustics with great certainty for almost any impact angle. Determining the fraction of angles leading to a detection therefore provides a viable way to measure the efficiency $\epsilon$ with which a given $(d,q)$-configuration can be detected. Expressed in a more abstract form the geometric definition of detection efficiency $\epsilon(d,q)$ is then

$$\epsilon(d,q) \equiv \frac{1}{2\pi}\int_0^{2\pi} \mathrm{d}\phi\ \Theta[C(d,q,\phi) - C_\mathrm{thresh}], \tag{8.1}$$

where $\Theta[x]$ is a step function and the *contrast* C

$$C \equiv \frac{\chi^2_\mathrm{binary} - \chi^2_\mathrm{single}}{\chi^2_\mathrm{binary}} = 1 - \frac{\chi^2_\mathrm{single}}{\chi^2_\mathrm{binary}} \quad . \tag{8.2}$$

Note that $\phi$ is uniformly distributed and that the contrast C is different from the quantity used in Gaudi et al. (2002), who used $\Delta\chi^2 = \chi^2_\mathrm{binary} - \chi^2_\mathrm{single}$.

We decided to use the contrast C, because it overcomes a subtle but important shortcoming of the Gaudi et al. approach. It takes into account the data quality without the need to do $\sigma$-clipping (i.e. removing outliers and rescaling error bars until a reduced $\chi^2$ of unity is reached on the base of a single lens model as done by Gaudi et al.) and without a priori assuming the absence of a planet. Since the contribution of outliers (due to bad weather or technical and human malfunctions) to the $\chi^2$ on average will be the same for the tested single and the tested binary lens model, the minus sign in the numerator will remove its contribution to the contrast.

[1]The reason for this however might be naturally explained by current migration theories (Stephane Udry, private communication).

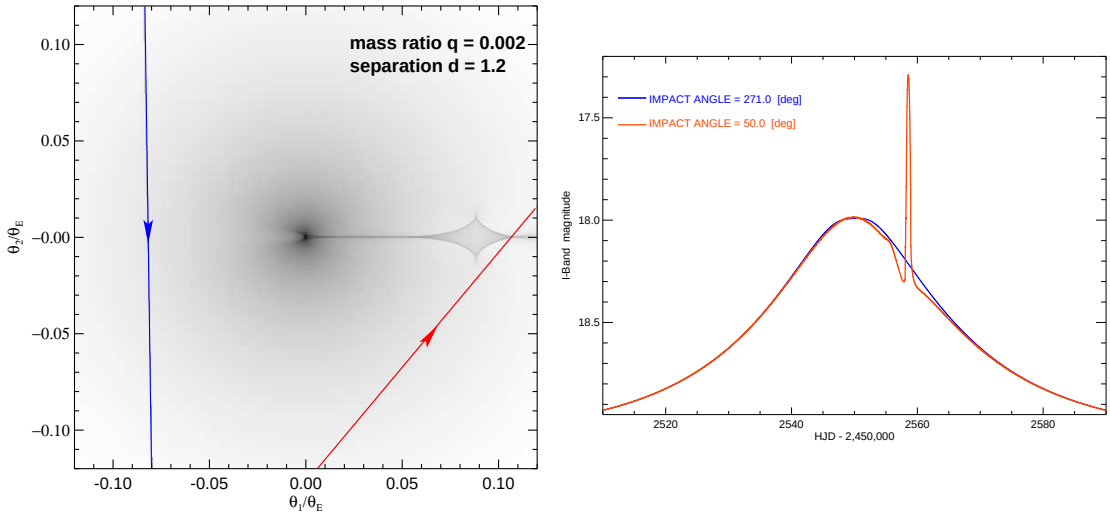


Figure 8.1: **Left**: Caustic geometry of a star+planet lens with mass ratio $q = 0.002$ and separation $d = 1.2$. Dark areas of the magnification map mark regions of high amplification. The blue solid line marks a source track with $u_o = 0.34$ and $\phi = 271.0^\circ$ passing a region where the influence of the (planetary) caustic is negligible. The red line source track has the same impact parameter $u_o = 0.34$ but a different impact angle $\phi = 50.0^\circ$ and this time hits the caustic. Arrows mark the direction of source motion. **Right**: The corresponding lightcurves of the tracks marked in the left plot. The $\phi = 271.0^\circ$ track leads to a lightcurve (blue) practically indistinguishable from a single lens curve, whereas the $\phi = 50.0^\circ$ track shows a short-lived but clearly detectable planetary signal.

### 8.3.1 Choice of detection/rejection threshold

Being aware of the non-gaussian statistics in our measurements, we adopt the conservative threshold of Gaudi et al. (2002) based on Monte-Carlo simulations on PLANET photometry of constant stars, where they find that a threshold of $\Delta\chi^2 = 60$ is high enough to avoid 'detections' arising from statistical fluctuations and/or unrecognized low-level systematics.

## 8.4 Ruling out planets (with TANGOBI)

The detection efficiency $\epsilon$ defined above is the probability that a companion of mass ratio $q$ and separation $d$ produces a signal inconsistent (i.e. $C > C_{\rm thresh}$) with a single-lens model. The absence of such signals implies then, that companions with this specific $(q, d)$ are ruled out with a confidence level of $\epsilon$.

The algorithm TANGOBI[2] (a code created by merging TANGO (Kubas 2005, Chapter 3, Appendix A) with the lens modeling software Gobi developed by Arnaud Cassan) is

[2] **T** ool for **AN** alyzing **G** ravitational lensing **O** f **BI** naries

turning the recipe given in Gaudi et al. (2002) into exclusion diagrams, which constrain the presence of planetary companions in a given microlensing event. Its scheme is as follows:

1. Find best single-lens model for a given event to get $\chi^2_{\rm single}$
2. For fixed $(d, q, \rho_*)$ find for each trajectory $\phi \in [0, 2\pi]$ the best binary model by minimizing over $u_o, t_o, t_{\rm E}, F_{\rm S}, F_{\rm B}$ to get and store best $\chi^2_{\rm binary}$.
3. Repeat step (2) for each point of the $(q, d, \rho_*)$ - grid.
4. Choose a threshold $C_{\rm thresh}$, evaluate $C(q, d, \phi, \rho_*)$ and compute $\epsilon(q, d, \phi, \rho_*)$ for the complete grid.

Note that our detection efficiency is also a function of the source size $\rho_*$, in contrast to the point-source-binary-lens models used in Gaudi et al. (2002) and all other previous studies (Snodgrass et al. 2004). As seen in Sec. 2.1.2 extended-source effects significantly influence the detectability of lightcurve signatures from Sub-Jovian planets. To be able to give constraints for this mass regime the source size therefore has to be taken into account. For that purpose we again make use of the ray-shooting technique to create a grid in the $(d, q, \rho_*)$ - space (see below).

Another difference to previous studies is that we use a combination of optimizing algorithms (Pikaia, Amoeba and Powell) to reduce the risk of overestimating our detection efficiency due to failure of a single technique to locate the best model. This effect is demonstrated in Fig. 8.4. In practice we choose the best (lowest) $\chi^2_{\rm binary}$ from the minimization over $(u_o, t_o, t_{\rm E}, F_{\rm S}, F_{\rm B})$ using Amoeba, Powell, Pikaia+Amoeba, or Pikaia+Powell (see also Chapter 3).

### 8.4.1 Choice of grid + simulations of amplification maps

The maps used as grid in the $(q, d)$-parameter space are generated with the ray-shooting method (Wambsganss 1999). Their size is $(2048)^2$ pixel with a resolution of 0.001 $\rm R_E$ and a ray density per pixel of $\gtrsim 10\,000$. We note that for data outside a map where extended source effects are negligible, we extend the model using a point source approximation.

We scan the mass ratio in the interval $-(\log q)$ =2.00, 2.25, 2.5, 2.75, 3.00, 3.25, 3.5, 3.75, 4.00, 5.00 (which covers roughly the mass spectrum from the most massive non Deuterium fusors down to Earths for the typical lens scenario) and the separation in $d/R_{\rm E} = 0.1, 0.2, ...2.5$ plus the corresponding $1/d$ (see Appendix B.3). Intentionally this choice of the grid limits our exclusion conclusions mainly to the lensing zone, since it is there where we are most sensitive to planets (Sec. 2.1.1), and of course computational resources demand a reasonable cut in the $d$-space.

The map origin at $(0, 0)$ is the center of mass of the system, the planet is located on the positive x-axis and the lens star on the negative x-axis. We then convolve these maps with 3 different source sizes $\rho_*$ ranging from 0.001, 0.005, to 0.010 $R_{\rm E}$, to probe physical source sizes of $\sim 1, \sim 6, \sim 13$ $R_\odot$ (assuming $M_{\rm L} = 0.3$ $M_\odot$, $D_{\rm L} = 4$ kpc, $D_{\rm L} = 8.5$ kpc ).

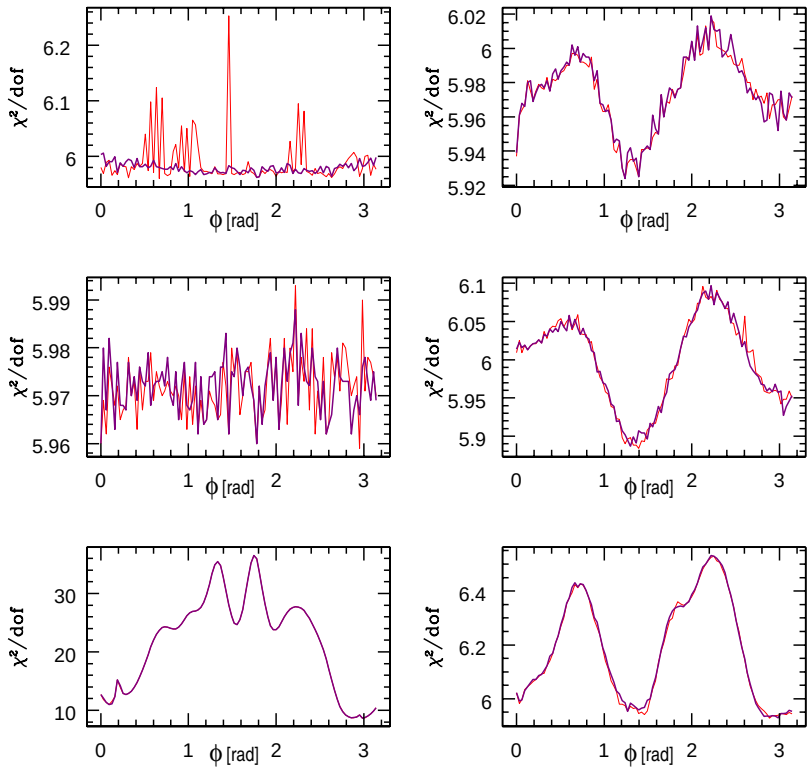


Figure 8.2: Typical convergence behavior of Amoeba (thin line) and Powell (thick line) in the modeling process of locating the best set of $(u_o, t_o, t_\mathrm{E}, F_\mathrm{S}, F_\mathrm{B})$ - parameters of a binary lens for six different given configurations of mass ratio $q$, separation $d$ as function of the uniformly sampled impact angle $\phi$. While often the methods yield comparable results, it can occur that they differ significantly. For example in the top left plot, an optimization with Amoeba alone could overestimate the detection efficiency if the chosen threshold is low enough. To minimize such numerical induced noise in the contrast we do not rely on one technique alone, but pick always the lowest $\chi^2_\mathrm{binary}$ resulting from different minimization methods.

We note for completeness that we assume a linear limb darkening model for the source profile with $\Gamma = 0.50$ (which is inspired by previous measurements such as in Cassan et al. (2004) and Kubas et al. (2005b)) but are aware of the fact that due to the limited resolution of the source in our maps we are barely sensitive to limb darkening parameters. In total our $(d, q, \rho_*)$-library then consist of $11 \times 22 \times 3 = 726$ maps.

## 8.5 Test on artificial data

To test our algorithm we first use simulated events, created similarly to the recipe given in Sec. 3.2 (page 48). Besides a desirable complete coverage of the event and a secure

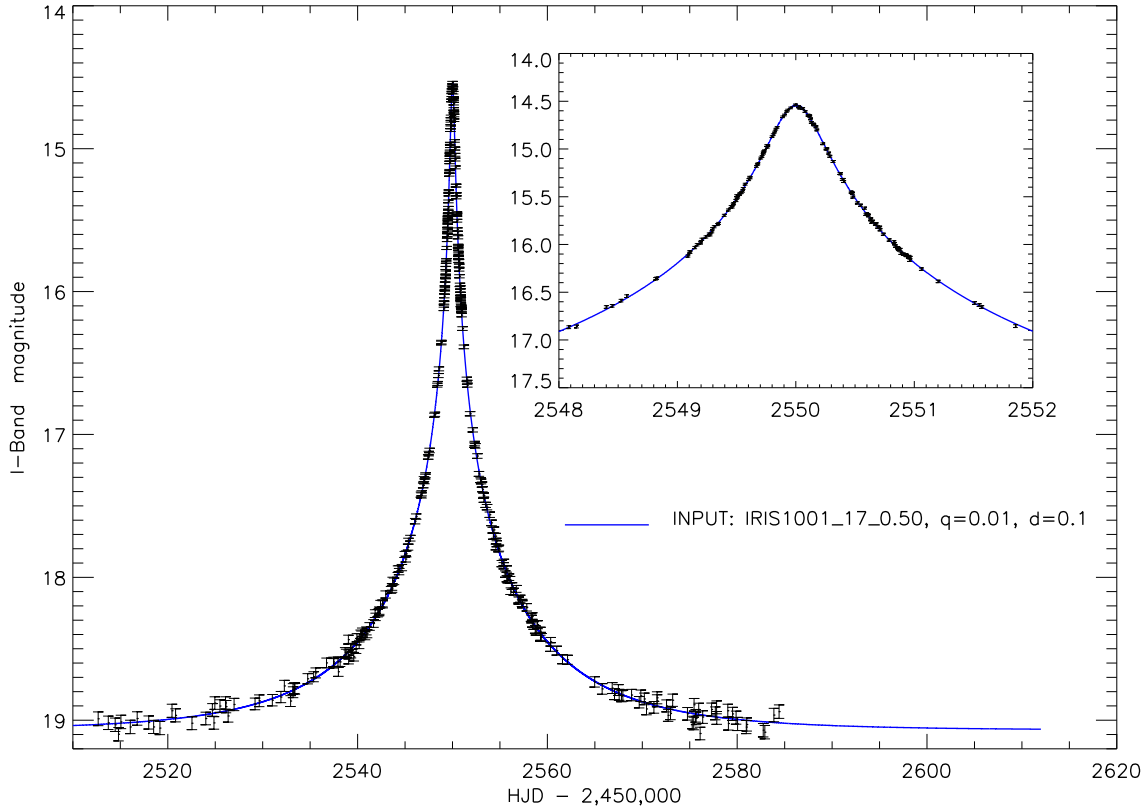


Figure 8.3: Simulated high amplification event (HAE-1) generated with the recipe given in Sec. 3.2. The solid line marks the input model from which the data are drawn with parameters $q = 0.01$, $d = 0.01\ R_{\rm E}$, $u_o = 0.013\ R_{\rm E}$, $\phi = 151.3^o$, $t_o = 2550.00$ HJD$'$, $\rm t_E = 17.0$ days and $\rho_* = 0.0025\ R_{\rm E}$. At baseline the photometric precision is $\sim 5\%$ improving to $\sim 1\%$ at the peak region, which is covered almost continuously with a $\sim 30$ min sampling rate (from 2549.0-2551 HJD$'$). The data set consists of 345 'measurements'.

baseline we especially sample the peak region densely, since as we recall from Chapter 6 it is the most sensitive region of the lightcurve in terms of excluding/detecting a planet. An example of such a test event is displayed in Figure 8.3, with underlying parameters mass ratio $q = 0.01$, separation $d = 0.10\ R_{\rm E}$, impact parameter $u_o = 0.013\ R_{\rm E}$, impact angle $\phi = 151.3^o$, impact time $t_o = 2550.00$ HJD$'$, time scale $t_{\rm E} = 17.0$ days and source size $\rho_* = 0.0025\ R_{\rm E}$. The photometric precision in the baseline region is $\sim 5\%$ improving to $\sim 1\%$ at the peak region, which is covered almost continuously with a $\sim 30$ min sampling rate (from $2549.0 - 2551.0$ HJD$'$). The data set contains 345 points and represents a high quality template.

Note that this event actually does contain a planet ($q = 0.01$, $d = 0.10\ R_{\rm E}$), which however is outside the lensing zone (Sec. 2.1.1) and leaves no significant (i.e. with the given accuracy not detectable) signature in the 'measured' lightcurve. This event therefore

demonstrates the limits of our approach in two ways: What can we exclude with high confidence and what not, with a nearly optimal data set of an high amplification event ($A_{\max} \approx 77$) following an apparent single lens lightcurve.

Adopting a rejection threshold of $\Delta\chi^2 = 60$ from Gaudi et al. (2002) the derived constraints on planets around the lens in this test event are shown in Fig. 8.4 for different source sizes. First we note that we are, as suspected, not sensitive to the existing planetary companion. Within the lensing zone however, rather strong constraints on the presence of Jovian planets can be given. For example a $\sim 1\ M_J$ planet ($\sim q = 10^{-3}$) is ruled out with high confidence (95%) for projected separations of $0.4 \lesssim d/R_{\rm E} \lesssim 1.7$, which correspond to about 1.2−5.1 AU (assuming a bulge-bulge lens scenario, with $D_{\rm S} = 8.5$ kpc, $D_{\rm L} = 6.5$ kpc) for all source sizes, spanning from $\sim 1-13\ R_\odot$. Also companions of several Neptune masses are not allowed with $(75-95)$ % confidence in orbits with separations $0.7 \lesssim d/R_{\rm E} \lesssim 1.3$. Some conclusion on Earth mass ($\sim q = 10^{-5}$) planets can only be given in the case when the source star size is of order $\sim 1\ R_\odot$ or less, i.e. the source is not a giant. In this case one could say, that with a certainty of $(50-75)$% there are no planets around HAE-1 with masses comparable to Earth in the orbital range $0.9 \lesssim d/R_{\rm E} \lesssim 1.2$.

## 8.6 Test on OGLE-1998-BLG-014

One of the first planet exclusion studies on a microlensing event was done on OGLE-1998-BLG-014 (Albrow et al. 2000a). In order to check if our method yields results consistent with theirs and to ensure compatibility with the conclusions drawn by Gaudi et al. (2002) we also apply Tangobi on this benchmark event. The measured lightcurve shown in Fig. 8.5 reveals a well sampled $A_{\max} \approx 16$ event with apparent deviations from a single lens model.

Although the amplification maps used by us intrinsically always imply extended sources, our smallest source with $\rho_*/R_{\rm E} = 0.001$, corresponding to $\sim 1\ R_\odot$, should be an adequate approximation, since the impact parameter $u_o/R_{\rm E} = 0.062$ of OGLE-1998-BLG-014 is not small enough for measurable interactions between central caustic and a source of this size. The result of our method comparison is shown in Fig. 8.6. Although they are not identical (which partly might be explained by the fact that we did not have access to exactly the same data set they used) they are consistent. Both approaches rule out $\sim 10 M_J$ companions between $\sim 1.2 - 7.4$ AU around the lens for a bulge-bulge lens scenario (with the source at $D_{\rm S} = 8.5$ kpc and the lens at $D_{\rm L} = 6.5$ kpc) but give little constraints on Sub-Jovian companions.

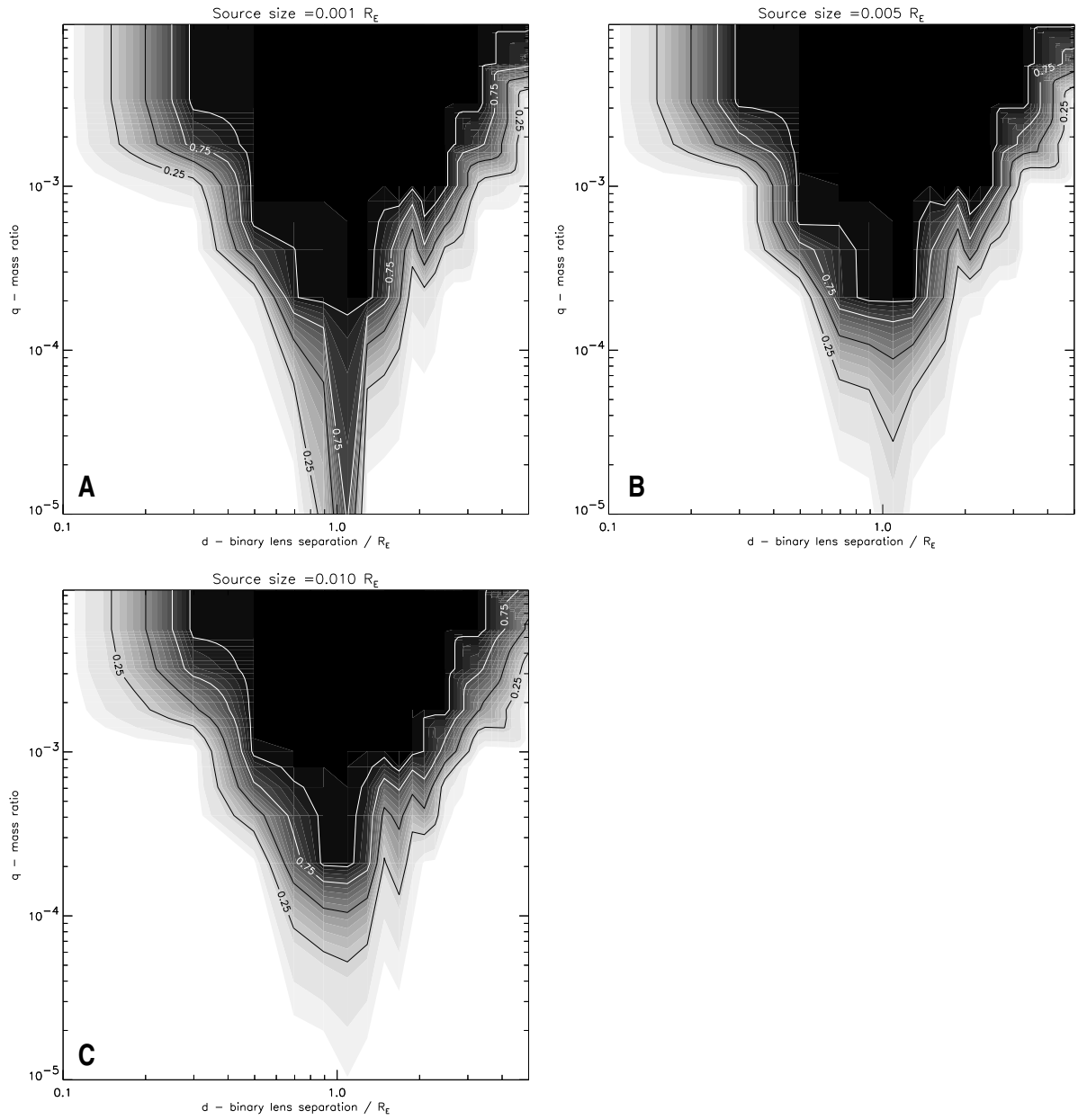


Figure 8.4: Exclusion diagrams for our test event HAE-1 (Fig. 8.3) for the three source sizes in our grid $\rho_*/R_{\rm E} = 0.001, 0.005, 0.010$ (**A,B,C**), corresponding roughly to physical sizes of 1, 6 and 13 $R_\odot$ for typical lens scenarios. Shown contours correspond to $25\%, 50\%, 75, 95\%$ (outer to inner) confidence levels of exclusion. The used rejection threshold $\Delta C$ is equivalent to the $\Delta\chi^2 = 60$ criterion derived in Gaudi et al. (2002). For all source sizes mass ratios $(\log q) = -3$, i.e. $\sim 1\ M_J$ companions with separations in the lensing zone $0.4 \lesssim d/R_{\rm E} \lesssim 1.7$ can be ruled out at a certainty level of 95%. Significant constraints (with $75 - 95$ % confidence) can also be given on Sub-Jovian down to several Neptune masses, albeit in a more narrow separation zone between $0.7 \lesssim d/R_{\rm E} \lesssim 1.3$. In the as 'good-as-it-can-get' situation of plot **A**, when the source is for instance a small turn-off star in the bulge, even constraints on planets (with $50 - 75$ % confidence) down to Earth masses for projected orbits of about $0.9 \lesssim d/R_{\rm E} \lesssim 1.2$ can be made (corresponding to $\sim 2.7 - 3.6$ AU for a bulge-bulge lensing event with the source at 8.5 kpc and the lens at 6.5 kpc).

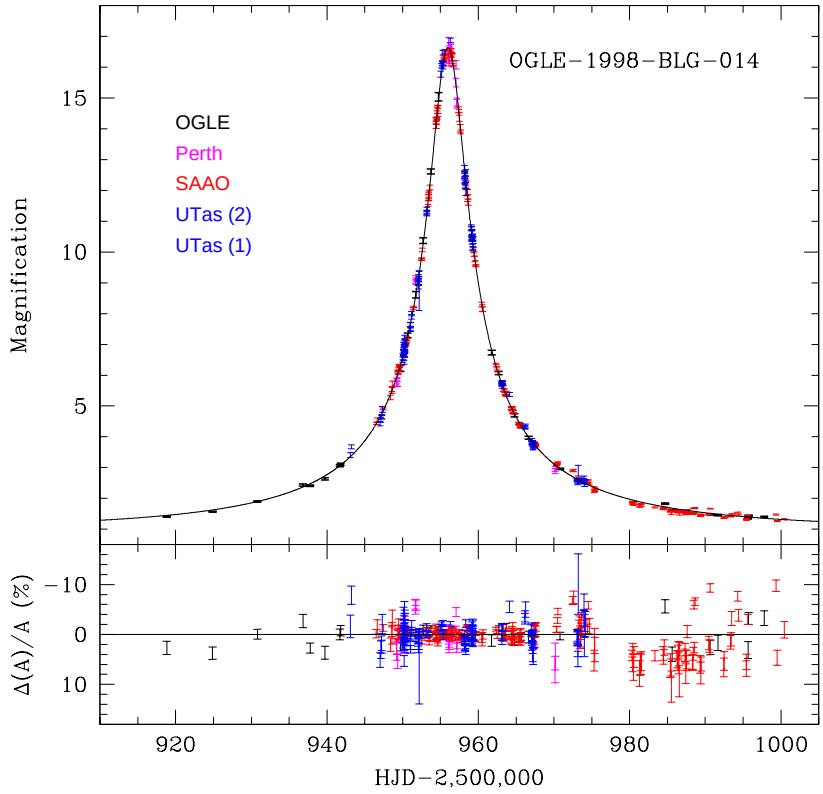


Figure 8.5: PLANET network data set and model of the reference event OGLE-1998-BLG-014 of Gaudi et al. (2002) & Albrow et al. (2000a) for planet exclusion studies, a well sampled apparently single lens event with maximum magnification $A_{\max} \approx 16$ and time scale $t_{\rm E} = 39.6$ days.

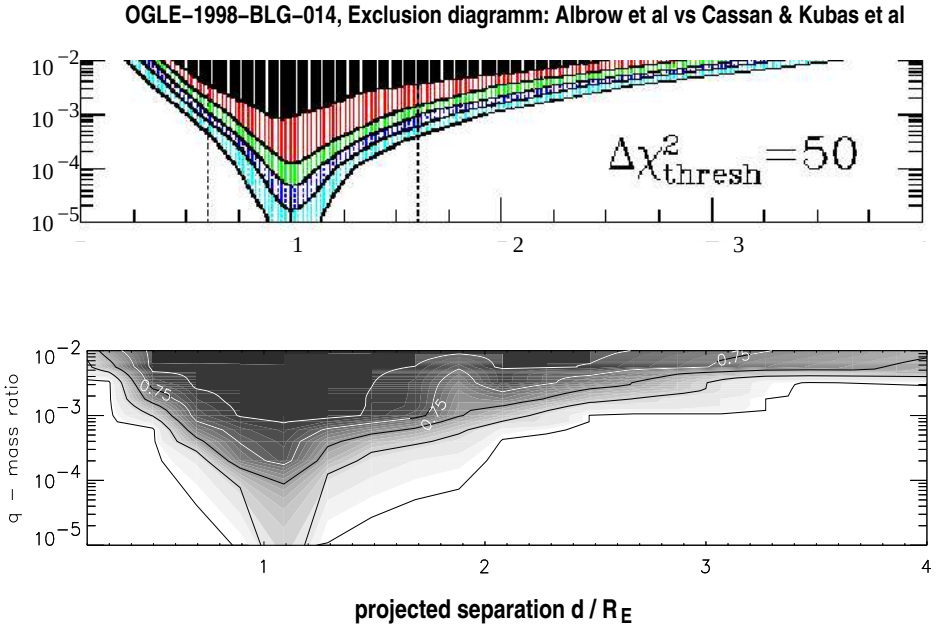


Figure 8.6: **Top**: Planetary companion exclusion diagram of OGLE-1998-BLG-014 from Albrow et al. (2000a) assuming a point source for $(\log q) \in [-5, -2]$ and $d/R_{\rm E} \in [0, 5]$. Contours mark exclusion confidence levels of $\epsilon = 5\%$ (outer contour), $25\%, 50\%, 75\%$ and $90\%$ (inner contour). **Bottom**: To mimic the approach plotted above, we perform the analysis with Tangobi using our smallest source size, which roughly corresponds to $\sim 1\ R_\odot$ and use an equivalent contrast threshold. Our result is not identical but consistent with their findings. Assuming a small source, both methods rule out companions to the lens of this event with mass ratio $q = 10^{-2}$ between $0.3 \lesssim d/R_{\rm E} \lesssim 2.4$ at 95% confidence. A mass ratio of $q = 10^{-2}$ corresponds to the mass ratio between a $10 M_J$ planet and a G-dwarf and the projected separation to $\sim$ 1.2-7.4 AU, for a bulge-bulge lens scenario with the lens at 6.5 kpc and the source at 8.5 kpc.

## 8.7 Discussion

We presented an algorithm (Tangobi) which uses the absence of anomalies in apparent single lens lightcurves to constrain the possible presence of planetary companions to the lens star. This method extends and refines the approach of Gaudi et al. (2002) by taking into account finite source size effects. Comparison tests done on OGLE-1998-BLG-014 yield constraints consistent with their method, i.e. ruling out $\sim 10 M_J$ planets in (projected) orbits of $\sim 1.2 - 7.4$ AU around the lens. While finite-source effects have a negligible influence on the results of exclusion studies for Jovian mass planets, they can not be neglect in the Sub-Neptune mass regimes. By applying Tangobi to a large sample of events (i.e. the complete PLANET 1995-2004 datasets) we will be able to strengthen the upper limits on the Galactic abundance of Jovian companions in the lensing zone given by Gaudi et al. (2002) and might also give the first limits for planets of several Neptune masses. To infer at least some upper limits on the presence of Earth mass planets the source star targets should have sizes $\sim 1\ R_\odot$ or less, which are out of reach for the capabilities of current 1m-telescope class microlensing campaigns. Next generation microlensing searches conducted from space or Antarctica (see Sec. 9.1.1) however, will most likely be sensitive to Earth mass planets.

Finally we note in the framework of Tangobi, also events which clearly exhibit extended-source effects (as OGLE-2004-BLG-254 from Chapter 7), can also be studied to constrain the presence, respectively absence of planets.

# Chapter 9

# Summary and outlook

> If you are going through hell, keep going.
>
> *Sir Winston Churchill*

Base of the work presented in the previous chapters are the software packages Tango & Tangobi, developed for the analysis of gravitational binary lenses. It could be shown that genetic algorithms are well suited for exploring the intricate parameter space of binary lenses. With the help of these tools several data sets from the microlensing campaign PLANET have been analyzed, leading to the following main results:

- The analysis of event OGLE-2002-BLG-069 (Chapter 5) lead to a second time ever determination of the mass of a binary lens. This event involves a G5III cool giant in the Bulge at a distance of $D_{\rm S} = (9.4 \pm 1.4)$ kpc lensed by an M-dwarf binary system of total mass $M = (0.51 \pm 0.15)\ M_{\odot}$ located at $D_{\rm L} = (2.9 \pm 0.4)$ kpc.

  Additionally and thanks to the successful first time spectroscopic monitoring of the caustic exit at high resolution with UVES, we were able to compare stellar atmosphere models with observations. Our data suggest that a PHOENIX atmosphere model assuming LTE is not an adequate description of the source star.

- While the dataset on OGLE-2003-BLG-208 (Chapter 6) is consistent with the lens having a Jovian companion, a star+star lens scenario is statistically preferred in the highly ambiguous parameter space of this high amplification event ($A_{\rm max} \sim 30$). A still to be done re-reduction of the data is unlikely to change this preliminary conclusion, since the essential regions of the lightcurve are not covered well enough by the observations. Although this event demonstrates that the characterization of possible planets from central caustic anomalies is more difficult than previously thought, it also shows that current network microlensing campaigns are in principle able to detect planets in peak anomalies of high amplification events, if they achieve a continuous coverage over the whole course of the anomaly, respectively the event.

- Observations of OGLE-2004-BLG-254 (Chapter 7) represent the best known data set of a single-lens caustic transiting a source star. Thanks to another successful spectroscopic monitoring with UVES, the source star could be identified as a K3II giant in the Sagittarius dwarf galaxy at a distance of about $\approx 24$ kpc. Upper limits on annual parallax effects and blend fractions in the lightcurve enable us to constrain the lens mass to be $0.1 \lesssim M_{\rm L}/M_{\odot} \lesssim 4$ at a distance $\gtrsim 19$ kpc, i.e. this event is a candidate for being the first reported case of self-lensing in the Sagittarius galaxy.

- The absence of planetary signatures in apparent single-lens lightcurves can be used to constrain the possible presence of planets around the lens star (Chapter 8). A new algorithm with this task (to constrain the allowed parameter space of planets around lenses) has been developed and successfully tested on the benchmark event OGLE-1998-BLG-014, ruling out $\sim 10 M_J$ companions in projected orbits between $\sim 1.2 - 7.4$ AU around the lens with 95% confidence.

  The possibility of taking into account extended source sizes in this new method provides a basis to give more realistic constrains on the Galactic abundance of extrasolar planets from microlensing searches.

## 9.1 Future work

A priority-ranked list of things to do after submitting and defending this thesis would look like this:

- The algorithm Tangobi (Chapter 8) for the exclusion of planetary companions around the lenses has to be applied to all suitable events in the PLANET database to give statistically upper limits on the galactic abundance of extrasolar planets in the lensing zone. As of now only $\sim 8\%$ of the total sample of apparent single-lens events from the 1995-2004 PLANET seasons have been computed.

- The data set of OGLE-2003-BLG-208 (Chapter 6) needs careful re-reduction to finalize the competing planetary and non-planetary models.

- The element abundance analysis of the presumed Sagittarius giant source star in OGLE-2004-BLG-254 (Chapter 7) has to be completed.

- There are still several well covered binary lens events with straight-fold-caustic passages in the PLANET data box. Although none of them possesses additional multiband/spectroscopic data comparable to OGLE-2002-BLG-69 (Chapter 5), their photometric data alone may be good enough to put interesting limits on the physical lens and source properties using the analysis techniques presented here. In fact almost any physical constraints that could be derived are of interest, since still very little is known on the source and lens population.

The points above sketch a short to mid-term working/submission plan. In the following last Section however I would like to invite the reader to have a short glimpse onto a more distant time, the prospects of next-generation microlensing searches to find Earth-like planets.

### 9.1.1 PLANET III: Hunt for second Earth's from DOME C

While the microlensing technique in principle is even sensitive to Earth masses, a short coming of current observing campaigns is their lack of spatial resolution (due to seeing effects) and light gathering power to be able to follow microlensing events from small and faint sources, which do not blur and damp lightcurve signatures from Earth-mass planets below measurability (contrary to the current typical microlensing targets, large Bulge giants, see also Sec. 2.1.2).
As shown in Chap. 6 a continuous coverage of the whole event is essential to disentangle ambiguous models. One way to fulfill all these requirements would be to put a telescope into orbit (such as SIM, or GEST (Bennett et al. 2003)), however there exists another promising approach. Site testing studies in Antarctica, at places with very special atmospheric conditions such as DOME C, revealed almost space-like observing conditions with reported median seeing values around $\sim 0.27$ arc-sec (and even below 0.1 arc-sec for 25% of the time).

Using the long $\sim$ 6 months nights at the South pole, a 2.5 m robotic telescope with a wide field imager and sampling rates of $\sim$ 20 min, could conduct a continuous $\sim$ 1% photometry (on I=20 mag turn-off Bulge stars) microlensing survey sensitive enough to Earth masses, as simulations such as the one displayed in Fig. 9.1, demonstrate (Beaulieu et al. 2004).

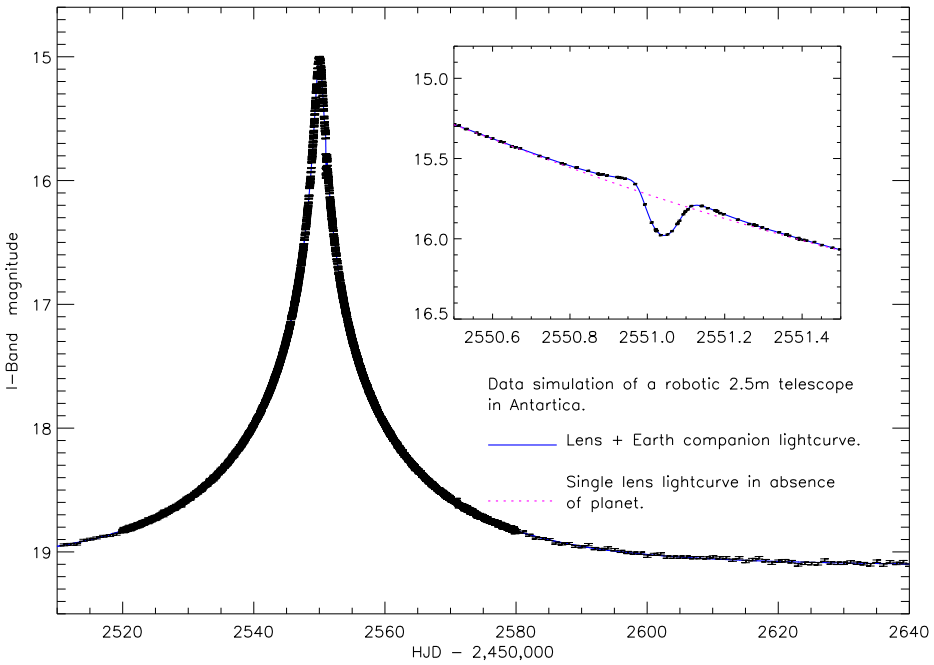


Figure 9.1: A simulated detection of an Earth mass planet with 3 AU orbit from a 2.5m robotic telescope in Antarctica with $\sim$ 20 min sampling rate (as long as the event is within the Einstein ring, outside the sampling is relaxed to 1 point a day), assuming a source size of 1 $R_{\odot}$. The anomaly, lasting about 4 hours, would be easily detected and sufficiently well covered.

# Appendix A

# Tango Basics Manual

> C: What is a good Tango dancer? T: Someone who walks well. C: And what is an excellent Tango dancer? T: ?? C: Someone who knows how to stop.
>
> *Carlos Cavito and Thierry LeCocq*

*While a complete documentation of the software package would violate the guidelines for the scope of the thesis and will be given elsewhere, this section wants to give a 'quick and dirty' guide to Tango to enable new users to do basic modeling tasks.*

## License

Tango is not freely distributable. To obtain a copy and register send a request to kubas@astro.physik.uni-potsdam.de.

## Soft-and hardware requirements

TANGO has been tested to run on PCs/Laptops under SUSE and Redhat/Mandrake Linux distributions with kernels 2.4xxx and higher, as well as on Compaq Alpha workstations with Tru Unix 5Va/b. It requires a Fortran90 compiler such as f90/f95 (Unix) or ifort (Linux, free), a C compiler (cc, gcc) and the free available GSL (Gnu Science Library). For making use of all features the presence of IDL (Version 5 and higher) and a the cfitsio library are also required.

Before starting to play around with TANGO it is required to have the following directories in the place where TANGO is executed:**./tracks** (coordinates of source trajectories are written here), **./tracks/ga** (model/fit results are saved here), **./ana** (for optional analysis of convergence behavior). A text file **jobnum** needs to be created, containing an integer number (format='i4.4',i.e. 0000,0010...) marking the current modeling session with a number.

## Overview of control files

The central control file for TANGO in your executing directory is **settings**, which looks like:

```
#  TANGO (Tool for AN alyzing G ravitational lens O bjects) RV 1.01
#  D.Kubas
#
#
# FITTING OPTIONS
#
# outflag = 1  (PSPL  (with AMOEBA/PIKAIA))
#   "     = 2  (BINARY LENS FIT (BNF) with PIKAIA)
#   "     = 3  (BNF HYBRID approach, first PIKAIA then AMOEBA)
#   "     = 4  (BNF with  AMOEBA only, specify start simplex!)
#   "     = 5  (binary source (with PIKAIA))
#   "     = 6  (MAP FIT)
#   "     = 7  (WRITE SPECIFIC MODEL)
#   "     = 8  (SFC fit with PIKAIA)
#   "     = 9  (SFC fit with AMOEBA)
#   "     = 10 (SFC fit with PIKAIA + AMOEBA)
# simflag = 2  (read dataset from file)
#
    2    simflag
    6    outflag
    1    paraflag (0/1 off/on parallax)
#
    281.662     ecliptic heliocentric longitude [deg]
    10.0934     ecliptic heliocentric lattitude [deg]
    2643.08333      time of perihelion  [MHJD]
    2720.29861      time of vernal equinox [MHJD]
#
#
#
~/ARCHIVES/microlens_event007.dat     data filename
#
#
    1    verbosity flag   (1 = standard,
#                           2 = silent, only fit parameters and chi2 written to screen
#                         for making of contour plots)
    1    plot flag         (1 = plot model points with resolution of map, or with default
#                               resolution of 0.001 R_E, 2=plot only model at data points)
    2700. , 3000.          start, end of plot range [MHJD]
#
# PIKAIA SETUP
#
# pikaia ctrl setup , ctrl is vector of control flags and parameters to control the
# behavior of the genetic algorithm, if value of element is < 0. then
# default settings indicated in bracets are used.
#
   1000    ctrl(1) = populations size (default is 100)
   400     ctrl(2) = number of generations (500)
```

```
   6       ctrl(3) = number of significant digits in encoding (6)
  -1.      ctrl(4) = crossover propability (0.85)
  -1.      ctrl(5) = mutation mode; 1/2/3/4/5 (2) , see documentation
  -1.      ctrl(6) = initial mutation rate (0.005)
  -1.      ctrl(7) = minimum mutation rate (0.0005)
  -1.      ctrl(8) = maximum mutations rate (0.25)
  -1.      ctrl(9) = relativ fitness differential ([0,1]; 1)
   2       ctrl(10) = reproduction plan; 1/2/3 (3)
   1       ctrl(11) = elitism flag 0/1 off/on , only for plan 1 & 2 (0)
  -1.      ctrl(12) = printed output 0/1/2 none/minial/verbose (0)
#
#
#=======================================================================
# BINARY LENS - POINT SOURCE MODEL
#=======================================================================
#.......................................................................
# PARAMETER SPACE BOUNDARIES (for PIKAIA)
#.......................................................................
 0.184, 0.190        mass ratio q
 0.1, 0.5            lens separation d
 0.001  , 0.1        minimum impact parameter u
 0. ,  360.          impact angle phi [deg]
 10.   , 140.        Einstein time t_E [days]
 2813., 2815.        time at origin t_o  [in MHJD]
 0.0, 0.5            parallax amplitude pi_E [==eta]
 0. ,  360.          parallax angle psi
#
#.......................................................................
# AMOEBA SETUP
#.......................................................................
#
#
    1.e-6 tol = tolerance for termination criteria
#-----------------------------------------------------------------------
# SEED VALUES FOR STARTING SIMPLEX / and
#  IF outflag=7 --> seed values are used for plotting WITHOUT fitting
#-----------------------------------------------------------------------
#               1=free,0=fixed parameter
#
#
0.187     q     0     mass ratio
0.312     d     0     lens separation
0.0662    u     1     impact parameter
228.781   alpha  1     impact angle
32.237    t_E    1     Einstein time
2814.288  t_o    1     time origin
0.3       pi_E   1     parallax semimajor axis
214.608   psi    1     parallax orientation
#-----------------------------------------------------------------------
# Initial size of starting simplex
#-----------------------------------------------------------------------
```

```
0.0005    dq           mass ratio
0.0005    dd           lens separation
0.005     du           impact parameter
0.5       dalpha       impact angle
0.5       dt           Einstein time
0.1       dpi          parallax semimajor axis
10.       dpsi         parallax orientation
0.05      dto          time origin
#
#=========================================================================
# (ANALYTIC) STRAIGHT FOLD CAUSTIC MODEL
#=========================================================================
#
#-------------------------------------------------------------------------
# Boundaries PIKAIA
#-------------------------------------------------------------------------
#
-0.507 ,-0.5085        t_cc caustic crossing time
43.68,  43.69          a_crit
0.073180, 0.073185     delta_t
3.321264  ,3.321268    w
0.499, 0.502           gamma limb darkening
16.88, 0.0002          a_other [linear amplifification]
#
#-------------------------------------------------------------------------
# AMOEABA setup
#-------------------------------------------------------------------------
# Characteristic length scales of starting simplex
#
10.0    dcrit [a_crit]
0.0001  dw slope outside caustic
0.01    dao [a_other]
0.1     ddt [delta_t]
0.1     dgamma ld parameter
0.05    dtc [t_cc]
```

As one can see it is quite self-explanatory, due to its comments. In the first part the desired model and optimization approach is chosen by setting the integer flag *outflag*. The celestial coordinates of the event are also set here and are activated when the parallax flag *paraflag* is set. The complete path of the file containing the data (here in ∼/ARCHIVES/microlens_event007.dat) needs to be given. The desired plot range can be also specified here. It follows the setup of the implemented genetic algorithm PIKAIA, with the first two lines specifying population size (needs to be even) and number of generations. For a detailed explanation of the other genetic parameters see (Charbonneau 1995), but it is recommended to leave them in the default settings (indicated in brackets after the corresponding comment). After that the description of the to be explored model and parameter space starts, beginning with the binary lens-point source model. Lower and upper parameter bounds can be inserted here, which will be used in the genetic optimization process. The initial seed parameters for the simplex algorithm AMEOBA follow, where

one can choose which parameters are allowed to vary and which are kept fixed with the integer *free/fix* flags. The tolerance criteria serves to terminate the AMOEBA optimization when the gradient of the simplex vertices is below that threshold. When a hybrid approach is chosen, i.e. first a genetic and then a gradient optimization the manually given seed values are overridden but the free/fix flags stay active. The last part controlling the straight-fold-caustic modeling obeys the same operation scheme.

### Data selection

The selection criteria for the data sets are defined in the file **inputdata**:

```
event       SX00007
site, band, PJD_start, PJD_end, Type, Type, seeing limit, error[mag]
d, I, 2000, 3000, 11, 11, 2.6, 1.
```

It is based on the PLANET nomenclature where a data archive has the form 'XXX00000X', with the first character specifying the telescope (Z=Danish, d,A=SAAO, W=Perth,U=Tasmania,...,see www.planet.iap.fr for a complete list of telescope acronyms), characters 2 and 3 mark the name of the alert team (i.e OB for OGLE BULGE, KB= 'Kiwi Bulge' for the MOA team), the first 2 digits the year and the last 3 the number of the event. The last character stands for the Filter. For example 'ZOB03208R' translates into Danish R-band data set of OGLE-2003-BLG-208 event. With this in mind, the first column of 'inputdata' selects the telescope and the second the band. Then a time interval in PJD=HJD′=HJD - 2,450,000 can be given and two valid types marking the quality of the data reduction (Schechter et al. 1993). The last two columns provide the opportunity to set thresholds on seeing and errors of the data used for modeling.

### Data format

```
# OB04273
#
#
# AOB04273I
# SAAO STE4 I
#   N Mag    Err   Date       Seeing BackG Typ ExpTm FWHM  AirMass
    1 17.573 0.014 3158.36933 1.469   2417  11  500  4.738 0.000
    2 17.544 0.015 3158.41664 1.148   2615  11  500  3.703 0.000
    3 17.522 0.014 3158.47080 1.233   2021  11  500  3.976 0.000
#
# ZOB04273R
# La Silla 1.54m R
#   N Mag    Err   Date       Seeing BackG Typ ExpTm FWHM  AirMass
    2 15.723 0.008 3157.85957 1.215   8536  11  540  3.115 0.000
    3 15.725 0.008 3157.88189 1.251   7380  11  540  3.207 0.000
#
# OOB04273I
# OGLE I
```

```
# Mag  Err   Date
 19.799 0.174 3126.6042
 19.856 0.191 3127.6102
```

The data is read from ascii files, where the PLANET data are stored in a 10 column format, the public data from OGLE, respectively MOA are treated in 3 column format. The data points do not have to be ordered in time, a '#' can be used to comment lines. The first non data line has to be the event name in the form OB04273, i.e. without band or site character. The start of the actual archive is then marked by the full name, i.e. by AOB04273I for instance.

## Binary-lens-point-source modeling HOWTO

Assuming TANGO is installed successfully, the needed directories and the 'jobnum' file created and the data are prepared in the format described above, then a standard first run, using the genetic algorithm + gradient search and neglecting parallax effects, would look like:

1. Specify the data you want to use for modeling in 'inputdata'

# In 'settings'

2. Set '3 outflag ', switch off parallax with '0 paraflag'

3. Fill in complete path to data set file

4. Set '1 verbosity flag' and '1 plot flag' and give plot range

5. Choose population size and number of generations

6. Choose appropiate parameter bounds

7. Choose which parameters of the genetic model outcome should be refined with the simplex technique by setting the 0/1 (fix/free) integer flags

8. Choose size of starting simplex and termination/tolerance threshold.

# On shell command line

9. Type '`tango`'

After the last command, TANGO will display the chosen settings to the screen and save them in the file settingsXXXX, where XXXX is the jobnumber from the 'jobnum' file. This first screen message will end like

```
 ***********END OF SETUP*********************

Reading data file
~/ARCHIVES/simdata4442.ncc
 Number of selected data points=    666
 Number of archives= 1 dSX00007I
                     666 points from archive dSX00007I
 data time span [days]=   101.422
       all dof =10
  dof [no flux]= 8

 starting BINARY LENS PIKAIA FITTING...
```

Depending on your settings of population size and generation number, it will take while for the next output to appear. After the genetic optimization the parameters are handed over to the simplex and after some more informative screen messages TANGO will end with

```
...fitting terminated!!

 fit was written to file: tracks/ga/fit_xb7003
```

and as the message says will write the model fit_xb7003 (with jobnum=7003 in this case) to the 'tracks/ga' directory. Additionally the files called 'finaldata7003' (containing the from the archive selected data points) and 'contributions7003' (containing the unreduced $\chi^2$ contribution term for each data point) are written into './tracks/ga'. A typical model output file looks like:

```
# q=0.828, b=  0.382, np= 436 , CHI^2/DOF=   462.33/  428=   1.080
# u=0.0286, phi=  193.336, t_E= 155.447, R_s=0.0000 t_o=2549.963
#                 base1=  19.185  , blend1=  21.394  blend fraction (at base)=  0.116
#                 base2=   0.000  , blend2=   0.000  blend fraction (at base)=  0.500
#                 base3=   0.000  , blend3=   0.000  blend fraction (at base)=  0.500
#                 base4=   0.000  , blend4=   0.000  blend fraction (at base)=  0.500
#                 base5=   0.000  , blend5=   0.000  blend fraction (at base)=  0.500
#                 base6=   0.000  , blend6=   0.000  blend fraction (at base)=  0.500
# res=    1000.000
#                  eta  = 0.0000 psi=   0.000  , diurnal amplitude=  0.0000
#                  constant acc: ampl.=   0.0000   angle=   0.000
# Number of archives= 1 dSX00007I
# bounds: q=[0.6000000 ,1.0000000] , b=[ 0.3000, 0.6000]
#         u=[-.1000 ,0.0000], phi=[ 180.0, 200.0] , t_E=[ 140.00, 200.00]
#         base6=[  0.000,  0.000] , blend6=[  0.000,  0.000]
#FIT amplification | FIT time | DATA (amp[flux])| time| site | Error [mag]| Residuals [mag]
        1.07772    2820.491720     1.09881    2820.491720  d     0.04600  0.02104
        1.07763    2820.607046     0.00000    2820.607046  ni    0.00000  0.00000
```

with the header marked with '#' containing the fit parameters and other useful info, as the chosen parameter bounds for example. The model can then be plotted with a suitable

plotting program. In case IDL is installed one can use the routine plot_model.pro from the package of IDL routines written for TANGO. Lines with the site set to 'ni' are from points between the data points needed for plotting.

## Binary-lens-extended-source modeling HOWTO

### Straight-fold-caustic-modeling

Follows the same cooking recipe as above, but using outflags=8,9 and/or 10 and the setup section for straight-fold-caustic crossings in 'settings.

### Using amplification maps

For a complete binary-lens-extended-source model amplification maps created with a modified version of Joachim Wambsganss 'microlens' ray shooting code (Wambsganss 1999)[1] are used. Once a map is shoot and convolved with the desired source profile (using the TANGO-IDL routine conv_map.pro for example) one can 'feed' the map(s) to Tango via the file 'map_cat':

```
# Library of (binary lens) magnification IRISXXXX maps
#
# IRIS no|mass ratio|separation|resolution|map size|source size|pixminx|pixminy|gamma
    2001    0.666       0.312     10240       2048      10        -0.1   -0.1  0.51
```

where the required characteristics of the amplification map are written down (here *resolution* is in pixel per Einstein radius, *pixminx/pixminy* the lower left coordinates of the map, *gamma* the limb darkening and *source size* and *map size* given in pixel). The directory of the map library then has to be written into 'settings' and then the modeling can proceed analog to the steps listed above using outflag option 6 and with the caveat, that since a map represents a specific mass-ratio-$q$-separation-$d$ configuration these parameters have to be kept fixed during the optimization process.

## Overview of routines

The code consists of about 42 routines, which are listed in groups according to their tasks and described very briefly below.

### amoeba.f, amotry.f, funk.f

Simplex based optimizing routines from the Numerical Recipes (Press et al. 1992), with funk.f as the supplied model function, which evaluates the $\chi^2$ of a given set of parameters.

### idx.f, sargc.f, sargp.f, sargv.f

String manipulation routines needed for input/output control.

[1] Send requests on license- and obtaining modalities to jkw@ari.uni-heidelberg.de

**coords.f, entre_coords.f**

Compute source trajectory at data points, respectively in between for plotting purposes.

**read_setup.f, write_setup.f**

Reading the TANGO setup file 'settings' and archiving to 'settingsXXXX', with XXXX being a job number such as 0007.

**read_data.f,filter_data_num.f, assign_data.f**

Reading/selecting/filtering the data sets used for modelling.

**pac.f, pac_fit.f, pac2.f, pac2_fit.f**

Calculating single-lens-point-source and single-lens-double-point-source amplifications and evaluating the $\chi^2$.

**pikaia.f**

Genetic algorithm package from Charbonneau (1995)

**fitness.f, xb2mod.f**

Evaluation of the fitness of the model and conversion between genetic model parameters (phenotypes) and standard lensing parameters.

**mag.f, laguer.f, zroots.f, gen_fit.f, simplex_fit.f**

Computation of binary-lens-point-source amplification and evaluation of $\chi^2$.

**cc_flux.f, cc_flux_exp.f, cc_gen_fit.f, geta.c, gammq.f, gammln.f, gcf.f**

Computation of straight-fold-caustic-passage amplification and evaluation of $\chi^2$.

**write_fit.f, write_ray.f, write_schneider.f**

Model output routines.

**IDL routines: conv_map.pro, plot_light.pro, plot_map.pro**

Convolving magnification maps with extended sources, plotting the model+data lightcurves, the magnification maps with source track and the $\chi^2$ parameter landscapes.

## A.1 The Roulette Wheel algorithm

The way Pikaia (Charbonneau 1995) selects individuals for breeding is based on the following algorithm:

1. Define $F = \sum_{i=1}^{n_\mathrm{p}} S_i$,
   where $n_\mathrm{p}$ is the population size and $S_i$ the fitness of individual $i$. This quantity is then a constant for a given generation.

2. Let $T_j = \sum_{i=1}^{j} S_i$, with $j = 1, ..., n_\mathrm{p}$
   be a running sum. Clearly it holds $T_{j+1} \geq T_j$ for all $j$ and $T_{n_\mathrm{p}} = F$.

3. Generate random number $R \in [0, F]$ and locate element $T_j$ for which $T_{j-1} \leq R < T_j$ is true. This $j$ is unique and determines the individual to select.

This recipe is analog to spinning a roulette wheel, where each individual is assigned a sector of angular size $\frac{1}{2\pi} \times S_i/F$.

# Appendix B

## B.1 Optical depth

To express the probability of a lens being microlensed one introduces the following cross section

$$\nu = \pi\theta_E^2 \ , \tag{B.1}$$

which defines the area on the sky covered by an Einstein radius sized disc. Integration along the line of sight over the product of $\nu \times$ number density of lenses $n_{\rm L}$ then defines the socalled *optical depth* $\tau$ (Narayan & Bartelmann 1996)

$$\tau = \frac{1}{\delta\omega}\int_0^{D_{\rm S}} n_{\rm L}(D_{\rm L})\nu \ dV \ = \frac{4\pi G}{c^2} D_{\rm S}^2 \int_0^1 n_{\rm L}(x) \ x(1-x) \ dx \ , \tag{B.2}$$

with $x \equiv D_{\rm L}/D_{\rm S}$ and $dV = \delta\omega D_{\rm L}^2 dD_{\rm L}$ being the volume of the spherical shell with thickness $dD_{\rm L}$ and radius $D_{\rm L}$ covering the solid angle $\delta\omega$ (see Fig. B.1).
This quantity $\tau$ describes the probability, that at any given moment a (source) star is within the Einstein ring of a lens, i.e. the probability of microlens event to occur in the observed solid angle $\delta\omega$. Obviously this only yields reasonable results if the cross sections of the lenses do not significantly overlap, in other words when $\tau \ll 1$. A rough estimate of the to be expected event rates can be derived assuming that all stars in our Galaxy have equal mass and a constant number density along the line of sight. Setting the mass density $\rho = n_{\rm L} \ M \cong 0.12 M_\odot/{\rm pc}^3$ (Lang 1980) we get

$$\tau = \frac{2\pi}{3}\frac{G\rho}{c^2} D_{\rm S}^2 = 1.0 \times 10^{-6} \left(\frac{D_{\rm s}}{8 \ {\rm kpc}}\right)^2 \ , \tag{B.3}$$

i.e. , microlensing events are pretty rare. This is why fields with high star densites such as the Galactic Bulge or the Magellanic Clouds are the prime targets for microlensing surveys.

## B.2 Parameterization of binary lens caustics

According to equation (1.11) we have to find the roots of the determinant of the Jacobian of the lens mapping (2.3). It turns out that this is done best in polar coordinates. With

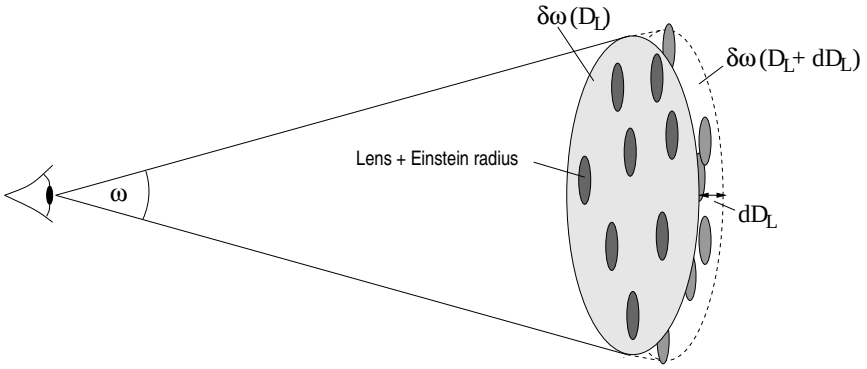


Figure B.1: The area covered by the Einstein radii of the lenses along the line of sight with respect to the solid angle $\delta\omega$ defines the measure of optical depth (Eq. B.2).

$\vec{x} = (x_1, x_2) = (r\cos\phi, r\sin\phi)$ the condition $\det J = 0$ can be written as

$$\begin{aligned} &16d^2r^2(r^4 - m_2)\cos^2\phi + \\ &+ 8rd[m_1m_2r^2 - (r^2 + 4d^2)(r^4 - {m_2}^2)]\cos\phi + \\ &+ (r^2 + 4d^2)^2(r^4 - {m_2}^2) - {m_1}^2r^4 - 2m_1m_2r^2(r^2 - 4d^2) = 0 \quad . \end{aligned} \tag{B.4}$$

This equation is quadratic in $\cos\phi$ and can easily be solved in the standard way.

The bifurcation values for the separation $d$ marking the transition between the three different topologies (Sec. 2) in dependence from $q$ can be given as (Dominik 1999b)

$$\begin{aligned} d_{\rm c} &= \left\{ \frac{[(1+q)^2 - d_e^4]^3}{27q} \right\}^{1/8} , \\ d_{\rm w} &= (1 + q^{1/3})^{3/2} \quad . \end{aligned} \tag{B.5}$$

Here $d_{\rm c}$ stands for the translation of middle to close and $d_{\rm w}$ for the translation of middle to wide separations.

## B.3 Lensing zone derivation

The (planetary) caustic positions can, as seen above, either be calculated directly by applying the lens mapping (2.3) to solutions of equation (B.4) or via the following simple argument (**?**). The influence of the planet on the light of the source is rather small when measured in units of the Einstein radius, to be more exact it holds that $R_{\rm p} \equiv R_{\rm E}({\rm planet}) = \sqrt{q}R_{\rm E}({\rm star})$[1]. From a lens plane point of view this means that the planet only has a significant effect if it is close to one of the images created by the main lens (see Fig. B.2). This is analog to the fact that in the source plane the source must be close to a planetary caustic in order to produce a measurable planetary signature in the

[1]This is a direct consequence from the definition of the Einstein radius in Eq. (1.8).

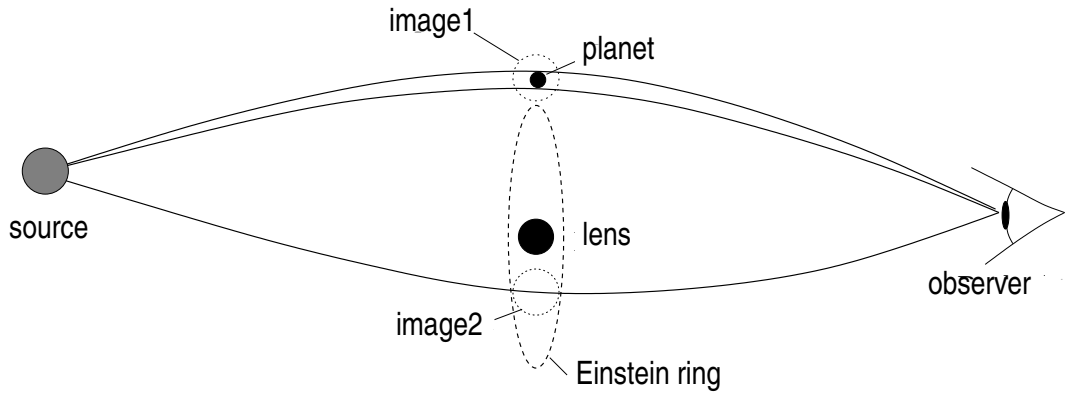


Figure B.2: A planet close to one of the images created by the lens star, splits this image into two new ones and so causes a perturbation in the single lens star lightcurve.

lightcurve. The image positions $x_i$ of the main lens as function of the source position $y_s$ are given via Eq. (1.10) and read (normalized with the Einstein radius)

$$x_i = \frac{1}{2}\left(y_s \pm \sqrt{{y_s}^2 + 4}\right) \ . \tag{B.6}$$

According to the argument above the relation between planet position $x_p$ and caustic position $y_c$ should be the same as between image positions and source position. Setting $x_i = x_p$, $y_s = y_c$ we get with Eq. (B.6)

$$y_c \simeq x_p - \frac{1}{x_p} \tag{B.7}$$

Here it is assumed that (without loss of generality) the planet is located on the x-axis, i.e. $y_c$ measures the position of the caustic with respect to the x-axis. This relation holds for $q \ll 1$ and $x_p \neq 1$, i.e. not in the direct vicinity of the topology change between middle to close, respectively middle to wide planet-star separations, since there our perturbative-picture description breaks down (Dominik 1999b). Excluding this (for small q vanishing) region and demanding with $x_c \leq 1$ that the caustics should be within the Einstein radius of the lens star, this equation yields the following lensing zone interval

$$0.6 R_{\rm E} \lesssim d \lesssim 1.6 R_{\rm E} \ . \tag{B.8}$$

Note that the relation (B.7) is invariant under the transformation $x_p \rightarrow -1/x_p$, i.e. 2 different planet-star separations can create caustics, which are different in their form but have the same distance to the origin. This gives rise to the so-called close-wide ambiguity of binary lenses (Dominik 1999b) and which can fool sometimes the analysis of lightcurves.

# Bibliography


Abe F., Bennett D. P., Bond I. A., Calitz J. J., Claret A., Cook K. H., Furuta Y., Gal-Yam A., Glicenstein J.-F., Hearnshaw J. B., Hauschildt P. H., Kent D., Kilmartin P. M., Kurata Y., Masuda K., Maoz D., Matsubara Y., Meintjes P. J., Moniez M., Muraki Y., Noda S., Ofek E. O., Okajima K., Philpott L., Rattenbury N. J., Rhie S. H., Sako T., Sullivan D. J., Sumi T., Terndrup D. M., Tristram P. J., Yanagisawa T., Yock P. C. M. 2003, *A&A* **411**, L493

Afonso C., Albert J. N., Andersen J., Ansari R., Aubourg É., Bareyre P., Bauer F., Blanc G., Bouquet A., Char S., Charlot X., Couchot F., Coutures C., Derue F., Ferlet R., Fouqué P., Glicenstein J. F., Goldman B., Gould A., Graff D., Gros M., Haissinski J., Hamilton J. C., Hardin D., de Kat J., Kim A., Lasserre T., LeGuillou L., Lesquoy É., Loup C., Magneville C., Mansoux B., Marquette J. B., Maurice É., Milsztajn A., Moniez M., Palanque-Delabrouille N., Perdereau O., Prévot L., Regnault N., Rich J., Spiro M., Vidal-Madjar A., Vigroux L., Zylberajch S., The EROS collaboration 2001, *A&A* **378**, 1014

Alard C. 2000, *A&AS* **144**, 363

Alard C., Lupton R. H. 1998, *ApJ* **503**, 325

Albrow M., An J., Beaulieu J.-P., Caldwell J. A. R., Dominik M., Greenhill J., Hill K., Kane S., Martin R., Menzies J., Pollard K., Sackett P. D., Sahu K. C., Vermaak P., Watson R., Williams A., Hauschildt P. H. 2001a, *ApJ* **550**, L173

Albrow M., Beaulieu J.-P., Birch P., Caldwell J. A. R., Kane S., Martin R., Menzies J., Naber R. M., Pel J.-W., Pollard K., Sackett P. D., Sahu K. C., Vreeswijk P., Williams A., Zwaan M. A., The PLANET Collaboration 1998, *ApJ* **509**, 687

Albrow M. D., An J., Beaulieu J. ., Caldwell J. A. R., DePoy D. L., Dominik M., Gaudi B. S., Gould A., Greenhill J., Hill K., Kane S., Martin R., Menzies J., Pogge R. W., Pollard K. R., Sackett P. D., Sahu K. C., Vermaak P., Watson R., Williams, A. (The PLANET Collaboration) 2001b, *ApJ* **549**, 759

Albrow M. D., Beaulieu J.-P., Caldwell J. A. R., Depoy D. L., Dominik M., Gaudi B. S., Gould A., Greenhill J., Hill K., Kane S., Martin R., Menzies J., Naber R. M.,

Pogge R. W., Pollard K. R., Sackett P. D., Sahu K. C., Vermaak P., Watson R., Williams A., The PLANET Collaboration 1999a, *ApJ* **522**, 1022

Albrow M. D., Beaulieu J.-P., Caldwell J. A. R., DePoy D. L., Dominik M., Gaudi B. S., Gould A., Greenhill J., Hill K., Kane S., Martin R., Menzies J., Naber R. M., Pogge R. W., Pollard K. R., Sackett P. D., Sahu K. C., Vermaak P., Watson R., Williams A., The PLANET Collaboration 2000a, *ApJ* **535**, 176

Albrow M. D., Beaulieu J.-P., Caldwell J. A. R., Depoy D. L., Dominik M., Gaudi B. S., Gould A., Greenhill J., Hill K., Kane S., Martin R., Menzies J., Naber R. M., Pollard K. R., Sackett P. D., Sahu K. C., Vermaak P., Watson R., Williams A., Pogge R. W. 1999b, *ApJ* **512**, 672

Albrow M. D., Beaulieu J.-P., Caldwell J. A. R., Dominik M., Gaudi B. S., Gould A., Greenhill J., Hill K., Kane S., Martin R., Menzies J., Naber R. M., Pollard K. R., Sackett P. D., Sahu K. C., Vermaak P., Watson R., Williams A., Bond H. E., van Bemmel, I. M. (The PLANET Collaboration) 2000b, *ApJ* **534**, 894

Alcock C., Akerloff C. W., Allsman R. A., Axelrod T. S., Bennett D. P., Chan S., Cook C. H., Freeman K. C., Griest K., Marshall S. L., Park H. S., Perlmutter S., Peterson B. A., Pratt M. R., Quinn P. J., Rodgers A. W., Stubbs C. W., Sutherland W. 1993, *Nature* **365**, 621+

Allen C. W. 1972, *Allen's Astrophysical Quantities*, 4th Edition, Springer, AIP

An J. H., Albrow M. D., Beaulieu J.-P., Caldwell J. A. R., DePoy D. L., Dominik M., Gaudi B. S., Gould A., Greenhill J., Hill K., Kane S., Martin R., Menzies J., Pogge R. W., Pollard K. R., Sackett P. D., Sahu K. C., Vermaak P., Watson R., Williams A. 2002, *ApJ* **572**, 521

Arnold V. J 1984, *Catastrophy Theory*, Springer, Berlin Heidelberg NewYork

Aubourg E., Bareyre P., Brehin S., Gros M., Lachieze-Rey M., Laurent B., Lesquoy E., Magneville C., Milsztajn A., Moscoso L., Queinnec F., Rich J., Spiro M., Vigroux L., Zylberajch S., Ansari R., Cavalier F., Moniez M., Beaulieu J. P., Ferlet R., Grison P., Madjar A. V., Guibert J., Moreau O., Tajahmady F., Maurice E., Prevot L., Gry, C. (The EROS Collaboration) 1993, *Nature* **365**, 623+

Beaulieu J. P., Brillant S., Cassan A. et al. 2005, *Mapping the Atmosphere of a Bulge Giant by means of Time-Resolved High-Resolution Microlensed Spectra*, in preparation

Beaulieu J. P., Cassan A., Kubas D., Jørgensen U. G., Albrow M. D., Bennett D., Brillant S., Caldwell, J. A. R. Coutures C, Dominik M., Donatowicz J., Fouqué P., Greenhill J., Hill K., Horne K., Jørgensen U. G., Kane S., Martin R., Menzies J., Pollard K. R., Sahu K. C., Vinter C., Wambsganss J., Watson R., Williams A., Marquette 2004, in *Dome C Astronomy/Astrophysics Meeting' - CESR - Toulouse, june 28th to july 1st 2004, Eds Giard, M. Paletou F.*

Bennett D. P., Bally J., Bond I., Cheng E., Cook K., Deming D., Garnavich P., Griest K., Jewitt D., Lauer T., Lunine J., Luppino G., Mather J., Minniti D., Peale S., Rhie S., Sahu K., Schneider J., Sonneborn G., Stevenson R., Tenerelli D., Woolf N., Yock P., Rich M. 2003, *American Astronomical Society Meeting Abstracts* **203**,

Bond I. A., Abe F., Dodd R. J., Hearnshaw J. B., Honda M., Jugaku J., Kilmartin P. M., Marles A., Masuda K., Matsubara Y., Muraki Y., Nakamura T., Nankivell G., Noda S., Noguchi C., Ohnishi K., Rattenbury N. J., Reid M., Saito T., Sato H., Sekiguchi M., Skuljan J., Sullivan D. J., Sumi T., Takeuti M., Watase Y., Wilkinson S., Yamada R., Yanagisawa T., Yock P. C. M. 2001, *MNRAS* **327**, 868

Bond I. A., Udalski A., Jaroszyński M., Rattenbury N. J., Paczyński B., Soszyński I., Wyrzykowski L., Szymański M. K., Kubiak M., Szewczyk O., Żebruń K., Pietrzyński G., Abe F., Bennett D. P., Eguchi S., Furuta Y., Hearnshaw J. B., Kamiya K., Kilmartin P. M., Kurata Y., Masuda K., Matsubara Y., Muraki Y., Noda S., Okajima K., Sako T., Sekiguchi T., Sullivan D. J., Sumi T., Tristram P. J., Yanagisawa T., Yock P. C. M. 2004, *ApJ* **606**, L155

Bonifacio P., Hill V., Molaro P., Pasquini L., Di Marcantonio P., Santin P. 2000, *A&A* **359**, 663

Cassan A., Beaulieu J. P., Brillant S., Coutures C., Dominik M., Donatowicz J., Jørgensen U. G., Kubas D., Albrow M. D., Caldwell J. A. R., Fouqué P., Greenhill J., Hill K., Horne K., Kane S., Martin R., Menzies J., Pollard K. R., Sahu K. C., Vinter C., Wambsganss J., Watson R., Williams A., Fendt C., Hauschildt P., Heinmueller J., Marquette J. B., Thurl C. 2004, *A&A* **419**, L1

Castro S., Pogge R. W., Rich R. M., DePoy D. L., Gould A. 2001, *ApJ* **548**, L197

Charbonneau P. 1995, *ApJS* **101**, 309

Chwolson O. 1924, *Astr. Nachrichten* **221**, 329

Claret A. 2000, *A&A* **363**, 1081

Cseresnjes P., Alard C. 2001, *A&A* **369**, 778

Darwin C. 1859, *On the origin of species*, John Murray ,London

DePoy D. L., Atwood B., Belville S. R., Brewer D. F., Byard P. L., Gould A., Mason J. A., O'Brien T. P., Pappalardo D. P., Pogge R. W., Steinbrecher D. P., Teiga E. J. 2003, in *Instrument Design and Performance for Optical/Infrared Ground-based Telescopes. Edited by Iye, Masanori; Moorwood, Alan F. M. Proceedings of the SPIE, Volume 4841, pp. 827-838 (2003).*, pp 827–838

Dominik M. 1995, *A&AS* **109**, 597

Dominik M. 1998a, *A&A* **333**, L79

Dominik M. 1998b, *A&A* **329**, 361

Dominik M. 1999a, *A&A* **341**, 943

Dominik M. 1999b, *A&A* **349**, 108

Dominik M. 2001, in *ASP Conf. Ser. 237: Gravitational Lensing: Recent Progress and Future Goals*, p. 259

Dominik M. 2004a, *MNRAS* **352**, 1315

Dominik M. 2004b, *MNRAS* **353**, 118

Einstein A. 1936, *Science* **86**, 506

Fields D. L., Albrow M. D., An J., Beaulieu J.-P., Caldwell J. A. R., DePoy D. L., Dominik M., Gaudi B. S., Gould A., Greenhill J., Hill K., Jørgensen U. G., Kane S., Martin R., Menzies J., Pogge R. W., Pollard K. R., Sackett P. D., Sahu K. C., Vermaak P., Watson R., Williams A., Glicenstein J.-F., Hauschildt P. H. 2003, *ApJ* **596**, 1305

Gaudi B. S., Albrow M. D., An J., Beaulieu J.-P., Caldwell J. A. R., DePoy D. L., Dominik M., Gould A., Greenhill J., Hill K., Kane S., Martin R., Menzies J., Naber R. M., Pel J.-W., Pogge R. W., Pollard K. R., Sackett P. D., Sahu K. C., Vermaak P., Vreeswijk P. M., Watson R., Williams A. 2002, *ApJ* **566**, 463

Gaudi B. S., Han C. 2004, *ApJ* **611**, 528

Gaudi B. S., Petters A. O. 2002, *ApJ* **580**, 468

Geyer C. J. 1992, *Statistical Science* **7**, 473

Ghosh H., DePoy D. L., Gal-Yam A., Gaudi B. S., Gould A., Han C., Lipkin Y., Maoz D., Ofek E. O., Park B.-G., Pogge R. W., Salim S., Abe F., Bennett D. P., Bond I. A., Eguchi S., Furuta Y., Hearnshaw J. B., Kamiya K., Kilmartin P. M., Kurata Y., Masuda K., Matsubara Y., Muraki Y., Noda S., Okajima K., Rattenbury N. J., Sako T., Sekiguchi T., Sullivan D. J., Sumi T., Tristram P. J., Yanagisawa T., Yock P. C. M., Udalski A., Soszyński I., Wyrzykowski Ł., Kubiak M., Szymański M. K., Pietrzyński G., Szewczyk O., Żebruń K., Albrow M. D., Beaulieu J.-P., Caldwell J. A. R., Cassan A., Coutures C., Dominik M., Donatowicz J., Fouqué P., Greenhill J., Hill K., Horne K., Jørgensen U. G., Kane S., Kubas D., Martin R., Menzies J., Pollard K. R., Sahu K. C., Wambsganss J., Watson R., Williams A. 2004, *ApJ* **615**, 450

Gould A. 1992, *ApJ* **392**, 442

Gould A. 1994, *ApJ* **421**, L71

Gould A., Gaucherel C. 1997, *ApJ* **477**, 580

Gould A., Han C. 2000, *ApJ* **538**, 653

Griest K., Safizadeh N. 1998, *ApJ* **500**, 37+

Gustafsson B., Bell R. A., Eriksson K., Nordlund A. 1975, *A&A* **42**, 407

Hart M. H. 1979, *Icarus* **37**, 351

Heyrovský D. 2003, *ApJ* **594**, 464

Jaroszyński M., Udalski A., Kubiak M., Szymanski M., Pietrzynski G., Soszynski I., Zebrun K., Szewczyk O., Wyrzykowski L. 2004, *Acta Astronomica* **54**, 103

Jiang G., DePoy D. L., Gal-Yam A., Gaudi B. S., Gould A., Han C., Lipkin Y., Maoz D., Ofek E. O., Park B.-G., Pogge R. W., Udalski A., Kubiak M., Szymański M. K., Szewczyk O., Żebruń K., Wyrzykowski Ł., Soszyński I., Pietrzyński G., Albrow M. D., Beaulieu J.-P., Caldwell J. A. R., Cassan A., Coutures C., Dominik M., Donatowicz J., Fouqué P., Greenhill J., Hill K., Horne K., Jørgensen S. F., Jørgensen U. G., Kane S., Kubas D., Martin R., Menzies J., Pollard K. R., Sahu K. C., Wambsganss J., Watson R., Williams A. 2004, *ApJ* **617**, 1307

Jørgensen U. G., Carlsson M., Johnson H. R. 1992, *A&A* **254**, 258

Kayser R., Refsdal S., Stabell R. 1986, *A&A* **166**, 36

Kayser R., Schramm T. 1988, *A&A* **191**, 39

Kubas D., Cassan A., Beaulieu J.P. et al. 2005a, in preparation

Kubas D., Cassan A., Beaulieu J. P., Coutures C., Dominik M., Albrow M. D., Brillant S., Caldwell J. A. R., Dominis D., Donatowicz J., Fendt C., Fouqué P., Jørgensen U. G., Greenhill J., Hill K., Heinmüller J., Horne K., Kane S., Marquette J. B., Martin R., Menzies J., Pollard K. R., Sahu K. C., Vinter C., Wambsganss J., Watson R., Williams A., Thurl C 2005b, *A&A in press, astro-ph/0502018*

Kupka F., Piskunov N., Ryabchikova T. A., Stempels H. C., Weiss W. W. 1999, *A&AS* **138**, 119

Lang K. R. 1980, *Astrophysical Formulae*, Springer, Berlin Heidelberg NewYork

Mao S., Di Stefano R. 1995, *ApJ* **440**, 22

Mao S., Paczyński B. 1991, *ApJ* **374**, L37

Metropolis N., Rosenbluth M., Teller A., Teller E 1953, *Journal of Chemical Physics* **21**, 1087

Misner C.W., Thorne K.S., Wheeler J.A. 1973, *Gravitation*, Freeman New York

Narayan R., Bartelmann M. 1996, *Lectures on Gravitational Lensing*, astro-ph/9606001

Nelder J. A., Mead R. 1965, *Computer Journal* **7**, pp.308

Paczyński B. 1986, *ApJ* **304**, 1

Press W. H., Teukolsky S. A., Vetterling W. T., Flannery B. P. 1992, *Numerical recipes.*, Cambridge: University Press

Rattenbury N. J. 2003, *Ph.D. thesis*, University of Auckland

Refsdal S. 1964, *Mon. Not. R. Astron. Soc.* **128**, 295+

Refsdal S. 1966, *MNRAS* **134**, 315

Schechter P. L., Mateo M., Saha A. 1993, *PASP* **105**, 1342

Schneider P., Wagoner R. V. 1987, *ApJ* **314**, 154

Schneider P., Weiss A. 1986, *A&A* **164**, 237

Schneider P., Weiss A. 1987, *A&A* **171**, 49

Snodgrass C., Horne K., Tsapras Y. 2004, *MNRAS* **351**, 967

Takahashi R. 2003, *ApJ* **595**, 418

Udalski A. 2003, *Acta Astronomica* **53**, 291

Udalski A., Paczynski B., Zebrun K., Szymaski M., Kubiak M., Soszynski I., Szewczyk O., Wyrzykowski L., Pietrzynski G. 2002, *Acta Astronomica* **52**, 1

Udalski A., Szymanski M., Kaluzny J., Kubiak M., Krzeminski W., Mateo M., Preston G. W., Paczynski B. 1993, *Acta Astronomica* **43**, 289

van Belle G.T. 1999, *PASP* **111**, 1515

Vermaak P. 2003, *MNRAS* **344**, 651

Wambsganss J. 1997, *MNRAS* **284**, 172

Wambsganss J. 1999, **109**, 353

Witt H. J. 1990, *A&A* **236**, 311

Witt H. J., Mao S. 1994a, *ApJ* **430**, 505

Witt H. J., Mao S. 1994b, *ApJ* **430**, 505

Wozniak P. R. 2000a, *Acta Astronomica* **50**, 421

Wozniak P. R. 2000b, *Acta Astronomica* **50**, 421

Yoo J., DePoy D. L., Gal-Yam A., Gaudi B. S., Gould A., Han C., Lipkin Y., Maoz D., Ofek E. O., Park B.-G., Pogge R. W., Udalski A., Soszyński I., Wyrzykowski Ł., Kubiak M., Szymański M., Pietrzyński G., Szewczyk O., Żebruń K. 2004a, *ApJ* **603**, 139

Yoo J., DePoy D. L., Gal-Yam A., Gaudi B. S., Gould A., Han C., Lipkin Y., Maoz D., Ofek E. O., Park B.-G., Pogge R. W., Udalski A., Soszyński I., Wyrzykowski Ł., Kubiak M., Szymański M., Pietrzyński G., Szewczyk O., Żebruń K. 2004b, *ApJ* **603**, 139

Zinnecker H., Köhler R., Jahreiß H. 2004, in *Revista Mexicana de Astronomia y Astrofisica Conference Series*, pp 33–36

## Recommended reviews, monographs and links

**Introduction**
"Lectures on Gravitational Lensing", Narayan R. & Bartelmann M., astro-ph/9606001
**Standards**
"Gravitational Lenses", Schneider P.,Ehlers J., Falco E.E., 1992, Springer-Verlag
"Singularity Theory and Gravitational lensing", Petters A.O., Levine H., Wambsganss J., 2001, Birkhäuser-Verlag
**Galactic microlensing**
"Gravitational Microlensing in the Local Group", Paczyński B., 1996, Annual Reviews of Astronomy & Astrophysics, Vol.34, p.419-459
**Extra-solar planets**
http://www.obspm.fr/encycl/encycl.html (general)
http://planet.iap.fr (PLANET collaboration)
**Global Optimization**
http://solon.cma.univie.ac.at/~neum/glopt.html
**Ephemerides**
http://aa.usno.navy.mil/

## Used constants

- $G = 6,672 \times 10^{-11}\ \frac{m^3}{kg\ s^2}$
- $c = 2,997925 \times 10^{8}\ \frac{m}{s}$
- $M_{\odot} = 1,9891 \times 10^{30}\ kg$
- $R_{\odot} = 6,960 \times 10^{8}\ m$

- $M_{\mathrm{J}} = 1,90 \times 10^{27}\ kg$
- $R_J = 70,85 \times 10^{6}\ m$
- $M_{\oplus} = 5,97 \times 10^{24}\ kg$
- $R_{\oplus} = 6,378 \times 10^{6}\ m$
- $1\ \mathrm{pc} = 3,26\ ly = 3,08 \times 10^{16}\ m$
- $1\ \mathrm{AU} = 1,4960 \times 10^{11}\ m$

# Appendix C

# Publication list

## Refereed Journals

### First Author

- D. Kubas et al. 'Full characterization of binary lens event OGLE-2002-BLG-069 from PLANET observations', A&A 435, 2005

### Coauthor

- A. Cassan et al. 'Probing the atmosphere of the bulge G5III star OGLE-2002-BUL-069' by analysis of microlensed Halpha line", Astron. Astrophys. 419, L1-L4, 2004.
- G. Jiang et al. 'OGLE-2003-BLG-238: Microlensing mass estimate of an isolated star' Astrophys. J., (astro-ph/0404394), ApJ 617, 2004.
- H. Gosh et al., 'Potential Direct Single-Star Mass Measurement', astro-ph/0405500, ApJ 615, 2004.

## Proceedings

- J.P. Beaulieu et al. 'Planet III: Searching for Earth-mass planets via microlensing from DOME C', 'Dome C Astronomy/Astrophysics Meeting' - CESR - Toulouse, june 28th to july 1st 2004, Eds Giard, M. Paletou F.
- M. Dominik et al., 'The PLANET microlensing campaign: Implications for planets around galactic disk and bulge stars', XIXth IAP colloquium 'Extrasolar Planets: Today and Tomorrow', Paris, France, 2003, ASP Conf. Ser.
- P.D. Sackett et al., 'PLANET II: A Microlensing and Transit Search for Extrasolar Planets', Bioastronomy 2002: Life Among the Stars, IAU Symposium 213, ASP, 2003.

# Acknowledgments

I bow to no one.

*Vin Diesel in 'The chronicles of Riddick'*

At first I would like to salute to and thank my French colleagues Arnaud 'Swim' Cassan (especially for his support in my final days), Jean-Philippe 'Belial' Beaulieu and Stephane 'Goret' Colombi for bringing back the fun and motivation into my work. Thanks to the whole PLANET crew for the adventurous experience to hunt and kill planets and Mauricio and Pancho at LaSilla for their support on the mountain in many ways.
Thanks to all my office mates during the years especially Andreas Helms and his radio, Lida Blond and Lida Black and little Lisa for their artwork and creating a comfy office. Thanks to Janine 'Schatzilein' Heinmueller for her charming company and optimism thru good and bad times. Muchas gracias to Rodrigo Gil-Merino for riding with me a long part of the Phd-road, our siestas and fruitful discussions on science, life and cheese plants. Much thanks also to the Wild Pack from the 4th floor, Suso, Ayhan, Jürgen, Ernest, Antonio, Murilo and Tiago for their nonlinear company. Cheers and 12 points to Isabelle, Turi and John. Thanks to James for his linguistic-physics lessons in the train. Thanks to Bernd and Alexander for taking care of my Qi. Thanks to Diana for introducing me to genetics and Robert Schmidt for precious tips and tricks on astro-ph and awk and for precious last-minute CPU-time. Thanks to the star man Wolf-Rainer Hamann for his hospitality, especially with respect to rooms and computer power. Thanks to Lars Koesterke, still appreciating your lessons on Fortran and life. Thanks to Tessie for his support. Thanks to Dr. Goetz Graefener, the fastest coffee drinker in town, for waiting for me to finish my coffee and for our mensa-cafeteria sessions. Thanks to Olaf 'The Paper Machine' Wucknitz for his inspiring comments. Thanks to the young and hip Adam Amara for all the fun we had during his visit and for sending me the 3rd day of '24'. Thanks to Helge Todt for staying in quarantine and keeping the flu away from me during my final days.
Thanks to Stanislav Lem, Johnny Cash and Jack Bauer for their inspiration, strength and understanding.
Thanks, sorry and greetings to all my friends from the other sides (the worlds of where no one has gone before, the milongas and life) to Barny, Heiko, Paul, Daniel, Gpunkt, Jpunkt, 'El Alemanecito' Constantin, Julia, Ines, Christine, Ricarda and Megan.

Special thanks and apologies to all not mentioned.

My very special thanks go to Andrea Brockhaus, Miss Secretary of the years 1990-2005, the inoffical Director of our Institute. I cannot imagine to have accomplished the thesis without her support and advice.

At last I thank my supervisor Joachim Wambsganß for providing me the opportunity, the freedom and the financial support to do this work.